UNIVERSITÁ DEGLI STUDI DI CATANIA
DIPARTIMENTO DI FISICA E ASTRONOMIA
DOTTORATO DI RICERCA IN FISICA (XXIX CICLO)

Stefano Burrello

Effective interactions and pairing correlations: from nuclei to compact stars

---

TESI DI DOTTORATO

Relatore:
Chiar.mo Prof. V. Greco
Dott.ssa M. Colonna

ANNO ACCADEMICO 2015/2016

Contents

List of Figures

List of Tables

Abstract

The purpose of this dissertation is to study some general properties of nuclear many-body systems, ranging from infinite nuclear matter to finite nuclei. Our investigations is focused in particular on nuclear systems with neutron excess, to get a deeper insight in the open issue which concerns the isospin dependence of the nuclear interaction. The analysis is concentrated on the behavior of nuclear matter at densities which lie below the saturation one, with the aim to address several nuclear phenomena, which involve surface effects in nuclei and clustering processes emerging in nuclear reactions and compact stellar objects. Our study is devoted also to shed light on the impact of some relevant interparticle correlations, mainly active in the low density region of the phase diagram, which occur in fermionic system and are responsible for the superfluid phenomena: the pairing correlations. Our goal is therefore to examine the interplay of these correlations with the other terms of the effective interaction, usually introduced to approach the nuclear many-body problem.

Wide attention is dedicated to the role of the pairing interaction in the astrophysical setting of stellar matter, especially when the cooling process of proto-neutron stars is concerned. Our analysis evidences in fact important pairing effects on neutrino emissivity and specific heat, which are two key ingredients in the thermal evolution of a compact star. On the one hand, superfluidity turns out to be responsible for a significant modification of the neutrino emission, for suitable density, asymmetry and temperature conditions, which can be of interest for the evolution of neutron stars and supernovae explosion in the pre-bounce phase. Focusing on neutral current neutrino scattering, we observe an increase of the neutrino differential cross

section in a paired and low-density nuclear medium, at least close to the spinodal border, where the matter is characterized by quite large density fluctuations. This behavior leads to an enhancement of neutrino trapping and a reduction in the energy flux carried by neutrinos.

On the other hand, we present a calculation of the specific heat in the inner crust of proto-neutron stars, within an approach based on cluster degrees of freedom, that considers the complete distribution of different nuclear species in thermal and beta-equilibrium. The resulting specific heat brings to light a strong influence of resonance population at moderate temperatures and in density regions close to the crust-core transition and the importance of an accurate treatment of beta-equilibrium for a quantitative determination of the specific heat and of the neutron star cooling curve.

Since nuclear systems with neutron excess have an essential role also in the context of nuclear structure, we investigate, within a semi-classical as well as in a quantal transport model, the structure and small amplitude dynamics of neutron-rich nuclei, focusing on the mixed isoscalar-isovector character of their collective excitations. In particular, we address some of the open questions concerning the nature of the low-lying isovector dipole strength experimentally observed in neutron-rich nuclei and known in literature as pygmy dipole resonance (PDR). We show that the relative isoscalar-isovector weight of the different modes is determined by their intrinsic structure, as well as by the type of initial perturbation considered so the PDR excitations turns to be essentially isoscalar-like, i.e., neutrons and protons oscillate in phase but with different amplitude. Moreover, we explore the relation between the mixed isoscalar-isovector structure of the dipole collective modes and the density dependence of the symmetry energy, focusing on its importance in shaping the neutron skin thickness. Further developments are moreover enviseged to get a deeper insight on the role of pairing and quantal effects in characterizing the collective excitations of neutron-rich nuclei.

Acknowledgments

La mia prima esperienza nell'affascinante mondo della ricerca scientifica è stata resa possibile solo grazie agli sforzi sinergicamente profusi dalle tante persone che mi sono state vicine in questi tre lunghi anni.

Adesso che l'ambizioso traguardo è vicino, sento che sia quindi giunto il momento di dedicare loro qualche riga per dimostrare la mia gratitudine.

Pur consapevole che la mia riconoscenza nei suoi confronti non sarà mai sufficiente a compensare quanto ricevuto, desidero innanzitutto ringraziare la mia tutor, la Dott.ssa Colonna, per...tutto! L'appellativo di tutor è infatti quanto mai riduttivo per descrivere il ruolo da lei rivestito nella stesura di questo elaborato e, in generale, nel percorso formativo da me seguito.

Non ho alcuna riserva ad ammettere che non sarei riuscito a portare a compimento questo importante obiettivo senza il suo costante supporto, soprattutto quando le vicissitudini che sono occorse nella mia vita lo avevano reso quasi un sogno irrealizzabile. Ciò nonostante lei ha sempre creduto nelle mie potenzialità, cercando di spronarmi per portare a termine i vari progetti in cui ero coinvolto. Spero pertanto di aver ripagato la sua fiducia.

Spero di non aver deluso neppure le aspettative del Prof. Greco, a cui sono profondamente grato per avermi concesso la possibilità di intraprendere questo percorso, per i suoi continui e preziosi consigli, nonché per la sana ironia con cui mi ha insegnato ad affrontare gli (strani!) eventi che accadono nelle nostre esistenze.

Ritengo inoltre di dover esternare la mia gratitudine nei confronti del Direttore, il Prof. Cuttone, e in generale dell'intero personale dei Laboratori Nazionali del Sud, per avermi fornito gli strumenti necessari, per effettuare concretamente l'attività relativa al mio dottorato di ricerca.

Un sentitissimo ringraziamento va poi alla Prof.ssa Gulminelli e al Prof. Matera, non solo per aver dedicato il loro tempo alla lettura di questo manoscritto, apportando delle correzioni che lo hanno indubbiamente reso migliore, ma per essersi in generale dimostrati in varie circostanze degli ottimi "maestri", oltre che dei sinceri amici.

Among my closest friends, special thanks are for Hua, who carefully read this thesis and helped me to solve several troubles which occur in these years. I would like to affirm that, in only two years, he actually becomed like a member of my family!

Di quella famiglia che non mi hai mai fatto mancare il necessario sostegno economico e, ancor più, psicologico e morale e per il quale non riuscirò mai ad essere riconoscente a sufficienza. E anche di quella (nuova!) famiglia che stiamo costruendo insieme ad Anna, che si è rivelata la risposta a tutte quelle "domande fondamentali sulla vita, l'Universo e tutto quanto" (cit.) che mi hanno convinto a studiare fisica.

Introduction

Atomic nuclei are many-body systems constituted by a strongly interacting and self-bound ensemble of nucleons with two possible isospin states, protons and neutrons. Since the last century, the study of such systems has held a primary importance in modern science, according to the key role that these objects take in the microscopic world, as well as in the astrophysical context. Unfortunately, the nuclear many-body problem has revealed one of the most complex issues existing in nature, owing to the peculiar characteristics of the strong interaction between the constituent particles, as well as by the large number of degrees of freedom involved and the related variety of phenomena produced. A huge amount of investigations have been devoted therefore to tackle the challenging problem of understanding the behavior of nuclear matter.

A big interest on the isospin physics, i.e. on charge asymmetric nuclear systems, has been moreover recently stimulated, triggered by the possibilities offered by new radioactive beam facilities, which have made feasible to perform measurements of nuclear properties for nuclei which lie far from the stability valley. At intermediate beam energies, reactions with exotic nuclei also allow one to explore several regions of the nuclear matter phase diagram and Equation of State (EoS). Furthermore, observational data from astrophysical objects, such as compact stars, can be crucial in constraining the nuclear EoS in density ranges and isospin asymmetries unreachable in terrestrial laboratories.

The knowledge of the isospin dependence of the nuclear interaction is presently considered one of the most outstanding questions in nuclear physics and it has demonstrated an active topic of research. A large number of works

are actually dedicated to the density dependence of the symmetry energy of the nuclear EoS, owing to its essential contribution to the total energy of asymmetric matter.

Our efforts are mainly devoted to investigate the behavior, in a broad sense, of asymmetric nuclear matter, at densities below the saturation one. Different studies involving this density region will be presented, ranging from the characterization of surface effects on structure and small amplitude dynamics in finite nuclei, to the description of the clustering phenomena occurring even in the crust of compact stars. These phenomena are generally related to the emergence of a liquid-gas phase transition, for the nuclear matter at sub-saturation density and relatively low-temperature. The latter process is also closely linked to the emergence of mechanical instabilities, underlying multifragmentation mechanism experimentally observed in nuclear reactions at Fermi energies.

The original (and unsolvable) quantal many-body problem is often approached adopting the mean-field approximation. This choice is based on the assumption, experimentally confirmed, that the main properties of atomic nuclei can be described by employing, in place of the bare nucleon-nucleon interaction, a suitable effective one-body potential which can averagely reproduce the mutual interaction between particles and accounts for the neglected correlations in an effective manner.

Several extensions of mean-field models have been however introduced to take explicitly into account the effects of relevant interparticle correlations. This is the case, for instance, of pairing correlations which occur, under suitable conditions, in fermionic systems and are responsible for the superfluidity phenomena observed in finite nuclei and in compact stars.

The theory of superfluidity is based on the Bardeen-Cooper-Schrieffer (BCS) theorem which states that, in a system of degenerate fermions, the Fermi surface is unstable due to the formation of pairs if there is an attractive inter-particle interaction in some spin angular momentum channel. This leads to a collective reorganization of particles at energies around the Fermi energy, which manifests itself in the formation of Cooper pairs. Correspondingly, an energy gap emerges in the quasi-particle spectrum, which disappears

at high-enough temperature, when the system reverts to its normal state.

Since pairing correlations are mostly active at low-density, they come out to play an important role in shaping the properties of the sub-saturated nuclear matter. The aim of this dissertation is to approach several aspects of the many-body problem in nuclear physics, ranging from nuclei to compact stars, in order to address the importance of the different terms characterizing the effective interaction and their interplay with the pairing correlations.

Wide attention, as stressed before, is dedicated to neutron-rich systems. Nuclei with a strong neutron excess exhibit several fascinating properties which make them qualitatively different from ordinary nuclei. For instance, neutron-rich nuclei are characterized by interesting new features for collective excitations, such as the so-called pygmy dipole resonance (PDR). Whereas the isovector giant-dipole resonance (GDR) is commonly referred to as neutrons and protons moving against each other, the nature of the pygmy resonance is still matter of debate, even if, roughly speaking, this excitation could be associated with an oscillation of the outermost neutrons (neutron-skin) against the isospin-symmetric core.

Regardless of their nature, the importance of these collective modes lies on the fact that the study of the electromagnetic dipole response of the neutron-rich nuclei potentially allows to shed light on fundamental properties of the interaction among the constituent particles. Indeed, these collective excitations are quite sensitivite to the isovector term of the nuclear effective interaction (or modern Energy Density Functional theory).

In our work, we investigate the dipole response of neutron-rich nuclei, employing some recently introduced effective interactions, which have been especially devised to improve the description of spin-isospin properties of nuclei. This produces a set of interactions of similar quality on the isoscalar channel and that, approximately, isolate the effects of modifying the isovector channel in the study of a given observable.

Neutron-rich nuclei are a key ingredient also in the nuclear astrophysics context, as far as nucleosynthesis processes are concerned, or in the structure modelization of compact stellar objects. The structure of compact stars (core collapse supernovae, proto-neutron stars and neutron stars) is still not fully

understood and is currently under lively research.

Neutron star physics constitutes indisputably a unique laboratory for testing nuclear matter under several conditions. The properties of the neutron stars are largely influenced by the nuclear EoS in a wide density range. There are many stellar EoS available in the literature, comprising a large variety of approaches and deduced by employing a large number of models. Considering only nucleonic degrees of freedom, at the high densities of the neutron star core, that is around and above the nuclear saturation density, nuclear matter is expected to be uniform and mean-field models with neutrons and protons are usually sufficient. At the lower densities of the crust and at temperatures below a critical value of approximately 15 MeV, nuclear matter develops instead inhomogeneities with a coexistence of gas and liquid phases on a macroscopic scale. In stellar matter, however, the transition is driven by the balance of the short-range nuclear and long-range Coulomb interaction. At very low temperatures, moreover, a solid phase with a lattice structure of nuclear clusters emerges. A consistent interpolation between the various regions is hence needed to cover all aspects in a single model and usually a combination of different approaches is required to depict a complete scenario.

In the physics of compact stars, also the presence of superfluidity is well established and has a significant effect on several phenomena related to the thermal evolution of these compact stellar objects. The cooling process of (proto-)neutron stars, in particular, seems to be strongly dependent, among the other features, on the specific heat and the neutrino emission of the star, which are both influenced by the formation of a fermionic pair condensate.

In particular, the specific heat of the neutron star is known to be strongly affected by superfluidity effects, which significantly reduce the crust thermalization time. The mean-field theoretical calculations employed so far to study the superfluidity of the crust however assume that the cluster component can be represented only by a single representative nucleus, neglecting that at finite temperature stellar matter is characterized by a whole distribution of different nuclear species. In our work, we explore the importance of this distribution on the calculation of the specific heat in the crust.

Moreover, we aim at investigating whether the interaction of neutrinos

with a low-density nuclear medium can be affected by the formation of Cooper pairs, thus modifying the cooling mechanism, by neutrino emission, of proto-neutron stars. We extend our analysis to nuclear matter conditions where large density fluctuations may develop, associated with the onset of the liquid-vapor phase transition, and clustering phenomena occur.

In the astrophysical applications presented above, we are going to introduce the pairing correlations in the spirit of the EDF theories, through a phenomenological effective interaction. Thus our studies on finite nuclei and compact stars are linked by the low-density behavior of the nuclear effective interaction and EoS.

The thesis is organized as follows. The first two chapters are entirely dedicated to review the main mean-field theories developed in the last century to approach the N-body problem in nuclear physics. The Hartree-Fock theory and its extension introduced to include the pairing correlations are presented, both in their static and dynamical forms. At the same time, we also discuss other quantal methods, such as the Random Phase approximation, and introduce semi-classical approaches, underlying advantages and drawbacks of each theory.

In Chapter 2, we also extensively discuss our pairing model and we present our first application, which concerns the analysis of the pairing effects on the characterization, along a clusterization process, of the instability exhibited by nuclear matter. We study in particular the effect on the isospin distillation mechanism, which is responsible, in a phase separation process, of the different isotopic content experimentally observed in the liquid and in the gas phase.

The neutrino emission of a neutron star is discussed in Chapter 3, where focusing on the neutrino interaction with a homogenous nuclear medium with electrons, we investigate, within a thermodynamical treatment, the impact of pairing correlations on the transport of neutrinos in stellar matter at low density, at the borderline with the occurrence of mechanical instabilities.

The heat capacity of the proto-neutron star crust is instead studied in Chapter 4. For this purpose, we present a Nuclear Statistical Equilibrium model which accounts for the simultaneous presence of nuclei, or clusters,

and homogenous matter, which typifies the (inner) crust of a neutron star. Within this framework, a given thermodynamical condition corresponds to a statistical superposition of finite configurations, the so-called Wigner-Seitz cells, each containing a different cluster embedded in a homogeneous electron gas, as well as a homogeneous gas of neutrons and protons. The importance of the cluster distribution and the key role of the β-equilibrium condition are highlighted, and the relevance of an accurate description of the system free energy, taking into account also cluster-gas interactions, is discussed.

The fifth chapter is finally focused on the small amplitude dynamics of nuclear systems, which often manifests the development of collective patterns. We investigate the collective modes in both asymmetric nuclear matter and finite nuclei with a strong neutron excess. We carry out our analysis within a semi-classical transport model, employing several effective forces, in order to test the influence of the different terms of the interaction in shaping the characterization of the nuclear response function. We also present a comparison with the time dependent Hartree-Fock calculations (TDHF), for small amplitude dynamics, to stress as well the importance of the quantal corrections. Finally, we make some calculations in the framework of the BCS extension of the TDHF theory, introduced to include the formation of the Cooper pairs. Focusing on the tin isotopic chain, we aim at highlighting the possible role of the pairing correlations in characterizing the structure and the response function of these systems, and again the interplay with the other terms of the effective interaction, also in view of a comparison with experimental results. Further measurements of pygmy and giant dipole resonances along isotopic chains are expected in fact to constrain tightly the density dependence of the symmetry energy of the nuclear EoS.

Chapter 1

Mean field theories and effective interactions

The investigation of interacting many-particle systems represents one of the most fascinating fields of modern science. Indeed understanding the properties of complex systems in terms of their constituent particles and the interaction among them is an exciting challenge [71, 150].

In particular, since it involves quantum particles as neutrons and protons, the study of atomic nuclei arises as a quantal many-body problem. Actually, as it is known, nucleons themselves reveal an internal structure, being constituted by quarks, but fortunately the energy scales associated to quark or to nucleonic degrees of freedom are well separated. So in low-energy nuclear physics, neutrons and protons can be regarded as elementary fermionic particles interacting through the strong nuclear force.

Anyway, the nuclear many-body problem is particularly complex due mainly to the following reasons: on the one hand, the nuclear interaction, due to its peculiar behavior, is rather difficult to handle; on the other hand, nuclei are generally mesoscopic systems, which means that they are neither few- nor infinite-body systems [107]. This means that only in a very restricted area of the nuclear chart, one can get the solution of the quantal problem through ab-initio techniques, but at the same time the number of nucleons is not enough to take advantage of possible simplifications used in infinite

systems. To make the situation worse, finite size effects imply interesting and not-trivial aftermath.

Although for the original quantal many-body problem it does not exist any general exact solution, in the last decades several theoretical methods have been developed in order to get a deeper insight of nuclear phenomena. In particular, while the relativistic quantum field theory is the reference model for high energy nuclear physics, most of the theoretical studies at lower energies are addressed within a non-relativistic context.

Surprisingly enough in view of the complexity of the interaction, many observations in nuclei have been understood by adopting the mean-field theory, which assumes that the nucleons behave as independent particles in an effective one-body potential, generated by a phenomenologically based effective interaction.

In this Chapter, we are going to discuss extensively the details of these effective interactions and to review the main mean-field theories developed to describe static and dynamic properties of nuclei.

1.1 The nuclear quantal many-body problem

In the theoretical treatment of the nuclear many-body problem, nuclear systems are in general considered to be composed of nucleons (protons and neutrons) which are fermions interacting through some specified forces, without internal degrees of freedom.

The solution of the general quantal many-body problem consists in finding the wave function

$$\Psi(\mathbf{r}_1, \mathbf{r}_2, \ldots, \mathbf{r}_N) \equiv \Psi(\{\mathbf{r}_i\}, t), \tag{1.1}$$

which is the solution of the Schrödinger equation:

$$\hat{H}\Psi(\{\mathbf{r}_i\}, t) = i\hbar\frac{\partial}{\partial t}\Psi(\{\mathbf{r}_i\}, t), \tag{1.2}$$

where $\hat{H}$ represents the N-body Hamiltonian operator.

The knowledge of the interaction between nucleons should be the start-

ing point to apply the techniques of modern many-body theory to the nuclear context. Even considering only two-body forces, the definition of the nucleon-nucleon interaction in the nuclear medium is really challenging. On the one hand, in fact, there exists no derivation of the bare nucleon-nucleon force from first principles. On the other hand, as stressed above, it is rather difficult in practice to handle with the bare nucleon-nucleon interaction, because of its strong repulsion at short distances, which makes inapplicable the usual many-body techniques [150]. In addition, it has also been pointed out a strong dependence of the nuclear interaction on the spin and isospin channels [197] and a significant influence of three-body forces [127]. Lastly, to further complicate the scenario, being charged particles, protons feel also the Coulomb interaction. Definitely, the solution of the nuclear many-body problem is extremely tricky and not only from the analytical point of view but also from the numerical one.

1.1.1 Mean field potential and correlations

In order to solve the complex nuclear many-body problem, one should take into account that the nucleons within a nucleus do not feel the bare nucleon-nucleon interaction, because the interaction is strongly renormalized by the medium effects, if one goes to a restricted description, so reducing the N-body to a one-body problem.

Despite of the complexity of the problem previously underlined, indeed, many experimental observations such as electron scattering on nuclei clearly revealed that nucleons, although they interact in principle with each other, behave in a good approximation like independent particles [81], occupying orbits of a single-particle potential. When two nucleons are surrounded by other nucleons, in fact, the associated wave function looks like an independent particle case. This can be interpreted as the result of the combined effect of the Pauli principle which blocks accessible configurations for the two nucleons and the properties of the force itself.

Due to this reason, one of the approximations commonly adopted to approach the nuclear many-body problem is the so-called mean-field approxi-

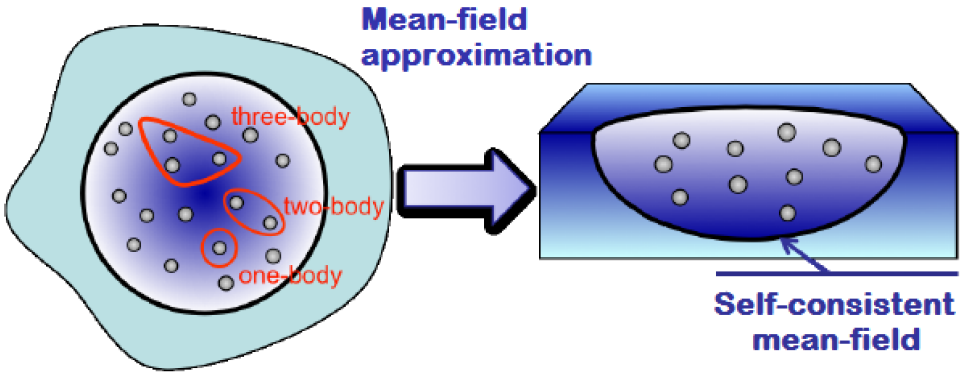

Figure 1.1: Illustration of the mean-field approximation. Replacement of the initial problem concerning all possible N-body interactions with a simpler problem of single-particles interacting only through a self-consistent mean-field (readapted from [107]).

mation. Under this hypothesis, as it is schematically shown in Fig. 1.1, the interaction of any given individual component with each other is approximated by a single averaged effect. In this way, each nucleon feels the self-consistent mean-field generated by the other nucleons composing the system. The effect of correlations, in this first order approximation, is not covered. So, the mean-field theory is reliable as long as the residual many-body correlations can be neglected.

Despite the simplification, gross qualitative features of nuclear structure are well reproduced by the mean-field and this is enough for several applications which will be examined in this thesis, such as: time dependent problems, finite temperature asymmetric nuclear matter studies, unified methods for extensive calculations over the whole nuclear chart in astrophysical applications.

1.2 Time-independent mean-field theory

A simple approximation often adopted to reduce the complexity of the many-body problem and the degrees of freedom involved in the Schrödinger equation is therefore based on the independent-particle picture. This leads for fermionic systems as nuclei to the well-known Hartree-Fock method. The

solution of the time-independent case is important because it allows one to describe the main static properties of nuclei and to lay the groundwork for its time-dependent extension.

1.2.1 The Rayleigh-Ritz variational principle

The Hartree-Fock method is based on the Rayleigh-Ritz principle which restricts the size of the Hilbert space where one seeks the solution of a variational problem. It is straightforward to demonstrate that solving the Schrödinger equation Eq. (1.2) in the stationary case, that is:

$$\hat{H}\left|\Psi\right\rangle = E\left|\Psi\right\rangle, \tag{1.3}$$

is equivalent to solve the following variational equation

$$\delta E\left[\Psi\right] = 0, \tag{1.4}$$

where

$$E = \frac{\left\langle\Psi\right|\hat{H}\left|\Psi\right\rangle}{\left\langle\Psi|\Psi\right\rangle} \tag{1.5}$$

labels the total energy E of the system. In such a way, as it is known, it is possible to connect the solution of Eq. (1.3) to an ordinary variational problem. Since the variation is usually restricted to a set of trial states $|\Psi\rangle$ and not to the whole Hilbert space, if the true state describing the system is not included in this set, the solution will be just an approximation of the exact eigenfunction. Anyway, the variational method is well-suited to determine the ground state of a system, because for any trial state $|\Psi\rangle$ it is easy to show that

$$E[\Psi] \geq E_0, \tag{1.6}$$

so that E_0 results as the lower limit of the variational calculation.

Once evaluated the approximated state $|\Phi\rangle$ of the exact ground state $|\Psi_0\rangle$, it is possible to get the approximated excited state $|\Phi_i\rangle$ just solving again the variational equation Eq. (1.4) with the supplementary constraint of orthogonality to the states previously determined. For higher excited state

the variational principle turns to be rather complicated or even inapplicable and so it has been applied, for example within the Hartree-Fock theory and its extensions, mainly to achieve a reliable estimation of the ground state.

1.2.2 Hartree-Fock (HF) theory

The Hartree-Fock (HF) theory assumes that the ground state $|\mathrm{HF}\rangle$ of a A-body fermionic system can be represented as a Slater determinant $|\Phi\rangle$:

$$|\mathrm{HF}\rangle = |\Phi(1,\ldots,\mathrm{A})\rangle \equiv \prod_{\alpha=1}^{A} \hat{c}_\alpha^\dagger \, |0\rangle \,, \tag{1.7}$$

viz it can be considered as the product of A independent single-particle states. It is possible to demonstrate that the ground state corresponds to the so-called Fermi sea, where only the A lowest levels are occupied (hole states) while all the others are left empty (particle states).

Actually, it is more convenient to represent the Slater determinant by defining the correspondent single-particle density

$$\rho_{ij} = \langle \Phi | \hat{a}_j^\dagger \hat{a}_i | \Phi \rangle \,, \tag{1.8}$$

where $\hat{a}_i^\dagger$ and $\hat{a}_i$ are the second-quantized single particle creation and annihilation fermionic operators.[1] The one-body density is characterized by the property to be idempotent, viz:

$$\hat{\rho}^2 = \hat{\rho}, \tag{1.10}$$

so that its eigenvalues can be either 1, in case of hole states (h), or 0 for the particle ones (p). In other words, in the basis where $\hat{\rho}$ is diagonal, it does not mix particle-hole states.

In order to determine the energy of the system, let us write the two-body

[1] These operators must obey the following anti-commutation relations:

$$[\hat{a}_i^\dagger, \hat{a}_j^\dagger]_+ = [\hat{a}_i, \hat{a}_j]_+ = 0, \qquad [\hat{a}_i^\dagger, \hat{a}_j]_+ = \delta_{ij} \qquad \forall i,j \tag{1.9}$$

Hamiltonian operator in second quantization as [22]:

$$\hat{H} = \sum_{i,j} T_{ij} \hat{a}_i^\dagger \hat{a}_j + \frac{1}{4} \sum_{i,j,k,l} \langle ij|\hat{\bar{V}}|kl\rangle \, \hat{a}_i^\dagger \hat{a}_j^\dagger \hat{a}_l \hat{a}_k. \tag{1.11}$$

The Hamiltonian is therefore the sum of a first contribution given by the kinetic energy term and of a second one with

$$\langle ij|\hat{\bar{V}}|kl\rangle \equiv \langle ij|\hat{V}|kl\rangle - \langle ij|\hat{V}|lk\rangle \,, \tag{1.12}$$

which is the antisymmetrized two-body interaction.

The energy of Eq. (1.5), that is the expectation value of the Hamiltonian Eq. (1.11), making use of the previous definition, becomes:

$$E^{\mathrm{HF}} = \sum_{ij} T_{ij} \, \langle \Phi|\hat{a}_i^\dagger \hat{a}_j|\Phi\rangle + \frac{1}{4} \sum_{i,j,k,l} \bar{V}_{ijkl} \, \langle \Phi|\hat{a}_i^\dagger \hat{a}_j^\dagger \hat{a}_l \hat{a}_k|\Phi\rangle \,. \tag{1.13}$$

By using Wick's theorem [194] and after some algebraic calculations (see section A.1), finally one gets:

$$E^{\mathrm{HF}}[\rho] = \sum_{ij} \left(T_{ij} + \frac{1}{2} U_{ij} \right) \rho_{ji} \tag{1.14}$$

where $\hat{U}$ is the self-consistent mean field, defined as:

$$U_{ij} = \sum_{kl} \bar{V}_{ikjl} \rho_{lk}. \tag{1.15}$$

The operator $\hat{U}$ is a one-body field and averages over all two-body interactions.

Since the variational principle can be formulated either in terms of variation of single-particle states or of the one-body density [22, 150], in order to determine the HF-basis, we can choose to minimize the energy for all the $\hat{\rho}$ values associated with the Slater determinant, imposing its variation

vanishes. This variation can be written

$$\delta E = E[\rho + \delta\rho] - E[\rho] = \sum_{ij} h_{ij}\delta\rho_{ji} = \sum_{m>A,n\leq A} h_{mn}\delta\rho_{nm} + c.c. \qquad (1.16)$$

where the single particle Hamiltonian $\hat{h}$ has been defined as

$$h_{ij} = \frac{\partial E[\rho]}{\partial \rho_{ij}} \qquad (1.17)$$

and taking into account that, because of Pauli blocking of hole states, the only $\delta\rho_{ij}$ not vanishing concern ph or hp transitions. Since these ph variations are arbitrary and using the result of Eq. (1.14), the variational equation Eq. (1.4) applied to this case, in the basis where $\hat{\rho}$ is diagonal, leads to:

$$h_{mn} = T_{mn} + \sum_{j=1}^{A} \bar{V}_{mjnj} = 0 \qquad (\text{for } m > A,\, n \leq A). \qquad (1.18)$$

This means that, analogously to the single-particle density $\hat{\rho}$ in the basis where it is diagonal, the single particle Hamiltonian

$$\hat{h} = \hat{T} + \hat{U}, \qquad (1.19)$$

does not mix particle and hole states and so, admitting a set of common eigenstates, they can be diagonalized simultaneously.

This consideration allows finally to write the following Hartree Fock equation:

$$\left[\hat{h}, \hat{\rho}\right] = \left[\hat{T} + \hat{U}[\rho], \hat{\rho}\right] = 0. \qquad (1.20)$$

Since $\hat{U}$ (and so also $\hat{h}$) depends on the density which is the solution of the problem, the equation above is self-consistent. Such as any self-consistent problem, it should be approached by an iterative procedure.

The results obtained after the numerical implementation of this model will be shown on Chapter 5. The HF theory, as we will see, is in fact a static model capable to describe, within the same formalism, some basic properties, such as masses, charge radii and deformations (when extended

to the so-called multi-reference framework) [185, 186] of the ground state of several nuclei, over a wide range of mass.

1.3 Dynamical evolution of the system

The time evolution of the quantal many-body system extends the stationary problem presented in the previous section. Several excited states show however new dynamical phenomena which can be explained only by supposing that many nucleons are coherently involved in the motion, giving rise to a collective vibration. In order to correctly address these collective states, several mean-field based small amplitude dynamical approaches have been developed in the last century. On the one hand, quantal approaches such as Random Phase Approximation (RPA) [49, 126] or Time Dependent Hartree-Fock (TDHF) theory in the small amplitude limit [27, 168], on the other hand, some semi-classical methods exploiting the corresponding Vlasov equation, such as for instance the Boltzmann-Nordheim-Vlasov (BNV) model [16, 25]. All these methods will be applied in Chapter 5, in order to describe the collective modes emerging in the dynamical evolution of nuclei.

1.3.1 Time Dependent Hartree-Fock (TDHF) theory

The stationary Hartree-Fock method described in Section 1.2.2 can be also formulated in a time-dependent way.

The starting point is an arbitrary vector $|\Psi(0)\rangle$ of the Hilbert space representing the state which describes the many-body system at the time $t = 0$. Since it is not an exact solution of the Schrödinger equation Eq. (1.3), as it is known, it evolves with the time as a wave packet by the time evolution operator:[2]

$$|\Psi(t)\rangle = e^{-\frac{i\hat{H}t}{\hbar}} |\Psi(0)\rangle \,. \tag{1.21}$$

[2]Actually, the same description holds even if $|\Psi\rangle$ is the exact solution of the static problem Eq. (1.3) and an external perturbation is introduced.

As a consequence, the corresponding one-body density

$$\rho_{ij}(t) = \langle \Psi(t) | \hat{a}_j^\dagger \hat{a}_i | \Psi(t) \rangle \,, \tag{1.22}$$

is time dependent as well. So, by making the derivative of Eq. (1.22) with respect to the time and exploiting the definition in Eq. (1.21), in the same Schrödinger picture, one achieves the equation of motion:

$$i\hbar \dot{\rho}_{ij}(t) = \langle \Psi(t) | \left[\hat{a}_j^\dagger \hat{a}_i, \hat{H} \right] | \Psi(t) \rangle \,. \tag{1.23}$$

It is possible to demonstrate (see section A.2) that, by neglecting the two-body correlations which cannot be taken into account by the mean field, the equation of motion above leads to the well-known TDHF equation:

$$i\hbar \dot{\hat{\rho}}(t) = \left[\hat{h}[\rho], \hat{\rho} \right] , \tag{1.24}$$

that is a first-order differential equation in time, where $\hat{h}$ is defined as in the static case, with the only one difference that now, since it includes the density $\hat{\rho}(t)$, it becomes time-dependent.

It is straightforward to observe that in the stationary situation, Eq. (1.24) is equivalent to the non-linear relation given by Eq. (1.20). For the static case, moreover, as it has already been pointed out in section 1.2.2, the two-body correlations are strongly suppressed by Pauli blocking. However, it is lawful to assume that these 2p-2h processes can be neglected even in the dynamical case, at least as long as the excitation energies are smaller than the energy of the last occupied single particle levels, named as Fermi energy. Under this assumption it is shown that, by supposing the initial state $|\Psi(0)\rangle$ coincides with a Slater determinant, this property will be maintained for the whole time evolution.

The TDHF theory will be applied on Chapter 5 to investigate the main features of giant resonances in nuclei. The study of these fundamental modes is really important and it has contributed to our understanding of the bulk behavior of the nucleus and of the dynamics of its excitations [90].

1.3.2 Random Phase Approximation (RPA) method

The investigation of collective excitations of nuclear systems can be addressed not only by employing the small amplitude limit of the TDHF theory described above, but also with the equivalent Random Phase Approximation (RPA) method, which is a technique based on the linearized TDHF equation and developed also to describe the response of the system to an external perturbation.

The RPA was introduced in 1953 by Bohm and Pines [24] in their study on plasma oscillations and it has been later extended to nuclear physics. The basic idea is to look at the influence on the system of an external time-dependent field as

$$\hat{F}(t) = \hat{F}e^{-i\omega t} + \hat{F}^{\dagger}e^{i\omega t} \tag{1.25}$$

where $\hat{F}$ is a one-body operator, which can be written as

$$\hat{F}(t) = \sum_{i,j} f_{ij}(t)\hat{a}_i^{\dagger}\hat{a}_j. \tag{1.26}$$

Under the hypothesis that the perturbation is weak, this operator introduces only a tiny variation on the nuclear density, which can be treated in linear order as:

$$\hat{\rho}(t) = \hat{\rho}^{(0)} + \delta\hat{\rho}(t) \tag{1.27}$$

with

$$\delta\hat{\rho} = \hat{\rho}^{(1)}e^{-i\omega t} + \hat{\rho}^{(1)\dagger}e^{i\omega t}, \tag{1.28}$$

so it constitutes only a small amplitude oscillation $\delta\hat{\rho}$, of frequency ω, around the stationary solution $\hat{\rho}^{(0)}$ of the Hartree-Fock equation for the Hamiltonian $\hat{h}^{(0)} = \hat{h}[\rho^{(0)}]$.

By including Eq. (1.27) in Eq. (1.24) and expanding up to the first order in the field, one easily gets:

$$i\hbar\delta\dot{\hat{\rho}} = \left[\hat{h}^{(0)}, \delta\hat{\rho}\right] + \left[\frac{\delta\hat{h}}{\delta\rho}\cdot\delta\hat{\rho}, \rho^{(0)}\right] + \left[f, \rho^{(0)}\right]. \tag{1.29}$$

It is smoothly demonstrated that particle-hole matrix elements are the only

ones not-identically vanishing and they obey to the so-called linear response equations (RPA):

$$\left\{ \begin{pmatrix} A & B \\ B^* & A^* \end{pmatrix} - \hbar\omega \begin{pmatrix} 1 & 0 \\ 0 & -1 \end{pmatrix} \right\} \begin{pmatrix} \rho^{(1)}_{ph} \\ \rho^{(1)}_{hp} \end{pmatrix} = - \begin{pmatrix} f_{ph} \\ f_{hp} \end{pmatrix} \tag{1.30}$$

where the matrices A and B are

$$A_{minj} = (\epsilon_m - \epsilon_i)\delta_{mn}\delta_{ij} + \frac{\partial h_{mi}}{\partial \rho_{nj}}, \qquad B_{minj} = \frac{\partial h_{mi}}{\partial \rho_{jn}} \tag{1.31}$$

and the single particle energy ϵ_k is defined as:

$$h^{(0)}_{kl} = \delta_{kl}\epsilon_k. \tag{1.32}$$

The RPA equation is solvable by inverting the matrix on the left-side hand, leading to a linear relation between the external perturbation and the corresponding density fluctuation

$$\rho_{kl} = \sum_{mn} R_{klmn}(\omega) f_{mn} \tag{1.33}$$

where the operator $\hat{R}$ is known in the literature as the response function and, in the general case, it can operate on all kind of excitations and not just on particle-hole type. In the RPA theory, it is shown that the response function has poles when the ω values match the eigenfrequencies of the system, when an arbitrary small perturbation is able to excite the related mode. Therefore, these resonances can be finally found simply solving Eq. (1.30) imposing that the external field vanishes. As a final remark, it is important to stress that, since this derivation is rather general, it applies also in the case of density dependent forces that are an essential feature of the mean-field approach.

1.4 Nuclear effective interactions

In the previous sections, it has been discussed how to solve the quantal many-body problem, in order to catch not only the stationary properties of

the system but also its dynamical evolution. This analysis highlighted at the same time the importance of knowing the underlying interaction.

Although in fact many aspects of nuclei can be explained under the hypothesis that the nuclear system is constituted by particles interacting through a self-consistent mean-field, unfortunately the natural HF approach, consisting of starting from the nuclear Hamiltonian to map a many-body into a one-body problem, does not work in nuclear physics.

Stimulated by this task, nuclear physicists have introduced the idea to use an effective nucleon-nucleon interaction, which can be considered as the infinite sum of two-nucleon scattering processes in the nuclear medium.

The effective interactions have been, over the last decades, a powerful tool to describe the properties and the dynamics of a large number of nuclei. Indeed, by using this approach, one gets two main advantages: on one side, it has been displayed that the effective interaction is rather well-behaved at short distances and so it allows the application of the usual many-body methods; on the other side, moreover, it consistently includes more many-body effects than if taking just the bare interaction in one-body approach.

There are many different ways to construct an effective interaction.

These effective forces can be in principle defined microscopically [31], but in practice it is very challenging to calculate them. Consequently, from the early days of nuclear physics, rather than make use of these ab-initio calculations, it has been preferred to adopt phenomenological forces [79, 122, 170], which contain a certain number of parameters adjusted to reproduce the experimental data. In many cases, this procedure has turned out to be extremely successful and, by using only a few parameters, many experimental data covering a quite large range of nuclear masses, have been explained.

The phenomenological method usually employed is to postulate a given functional form for the effective interaction, determining only a posteriori the parameters of the model, fixing them to reproduce some selected sets of nuclear data. The lack of uniqueness for the fit, however, has led to a large number of different parameterizations, which provide very different predictions when applied beyond their domain of validity.

Therefore, the most reasonable approach is to fit these phenomenological

interactions with the largest number of available data, deduced not only by the experiments but also by microscopic calculations in nuclear matter, as we will do in Chapter 2.

It is also preferable to choose the analytical form as simple as possible. For example, since we know that the range of the nuclear force is rather short, the simplest ansatz consists in using a zero-range force, whose radial dependence is described by a δ-function. Such forces are in fact simple to handle and can describe quite well some nuclear properties. However, more realistic forces need a finite range, which corresponds to the dependence of the effective interaction on the momentum. Looking in fact at the following momentum representation of the potential

$$V(\mathbf{p}, \mathbf{p}') = \frac{1}{(2\pi\hbar)^3} \int e^{-\frac{i}{\hbar}(\mathbf{p}-\mathbf{p}')\cdot\mathbf{r}_{12}} V(\mathbf{r}_{12}) d^3 r_{12}, \tag{1.34}$$

we can see that, if the function V of the relative distance $\mathbf{r}_{12} = \mathbf{r}_1 - \mathbf{r}_2$ between the two particles is a δ-function, the corresponding representation is a constant, otherwise any range represents a momentum dependence.

Finally, it is important to bear in mind that phenomenological effective forces can also depend on the density.

1.4.1 Skyrme-type interactions

The most commonly used phenomenological effective interactions are the zero-range Skyrme-type interactions. To trace their success, it is important to mention not only their flexible implementation, but also to the fact that Vautherin and Brink [186], employing Skyrme interactions, succeeded to reproduce the binding energies and the nuclear radii of the whole periodic table. Furthermore, the mathematical structure is not complex, because the contact range of the force implies the presence of the δ-function, which greatly facilitates the calculation.

Following the idea formulated by Skyrme in 1950s [170], the simplest

version of this kind of interactions assumes the following functional form:

$$\begin{aligned} V_{\text{Sky}}(\mathbf{r}_1, \mathbf{r}_2) = {} & t_0(1 + x_0\hat{P}_\sigma)\delta(\mathbf{r}_{12}) + \frac{1}{2}t_1(1 + x_1\hat{P}_\sigma)\left[\mathbf{p}_{12}^2\delta(\mathbf{r}_{12}) + \delta(\mathbf{r}_{12})\mathbf{p}_{12}^2\right] \\ & + t_2(1 + x_2\hat{P}_\sigma)\mathbf{p}_{12} \cdot \delta(\mathbf{r}_{12})\mathbf{p}_{12} + \frac{1}{6}t_3(1 + x_3\hat{P}_\sigma)\rho^\alpha\left(\frac{\mathbf{r}_1 + \mathbf{r}_2}{2}\right)\delta(\mathbf{r}_{12}) \\ & + iW_0(\boldsymbol{\sigma}_1 + \boldsymbol{\sigma}_2) \cdot \left[\mathbf{p}_{12} \times \delta(\mathbf{r}_{12})\mathbf{p}_{12}\right], \end{aligned} \tag{1.35}$$

where $\mathbf{p}_{12} = -\frac{i}{2}(\nabla_1 - \nabla_2)$ is the relative momentum, $\hat{P}_\sigma = \frac{1}{2}(1 + \sigma_1\sigma_2)$ is the spin-exchange operator and t_0, t_1, t_2, t_3, x_0, x_1, x_2, x_3, W_0, α are model parameters.

Each contribution in the previous formula describes a different feature of the phenomenological effective interaction: the first contribution is the central term, which depends only on the distance between the particles; the terms including t_1 and t_2 simulate the influence of non-local contribution introducing the dependence on the relative momentum $\mathbf{p}_{12}$; the fourth addend depends instead on the density of matter and aims to recreate a similar effect as one would have considering three-body contributions; the last term describes the spin-orbit two-body interaction.

The parameterization shown in Eq. (1.35) is therefore rather general and it depends on a considerable number of parameters, which have been added to get a better description of data. However, despite its simple mathematical form, for practical implementations some simplifications must be done. For this reason, it is often adopted a simplified version of Eq. (1.35) where only some of the parameters listed above are assumed to differ from zero, according to the functional form required for the interaction. Once the functional dependence is identified, the value of the parameters will depend on the properties of nuclear matter one wants to consider. The values of the parameters for some of the Skyrme interactions employed in our work fill out the Table 1.1.

Table 1.1: The values of the parameters for some Skyrme interactions employed in our works.

	SAMi-J27	SAMi-J31	SAMi-J35	SLy4
t_0[MeV fm^3]	−1876	−1844	−1799	−2489
t_1[MeV fm^5]	481.09	460.73	436.23	486.82
t_2[MeV fm^5]	−75.71	−110.2	−145.0	−546.4
t_3[MeV fm$^{3+3\alpha}$]	10185	10112	9955.4	13777
x_0	0.4822	−0.024	−0.4439	0.8340
x_1	−0.558	−0.459	−0.344	−0.344
x_2	0.2131	−0.431	−0.784	−1.000
x_3	1.0022	0.0076	−0.882	1.3540
W_0	81.937	216.87	273.61	123.00
W_0'	180.37	−133.6	−275.6	123.00
α	0.25463	0.2684	0.2843	0.1667

1.4.2 Energy Density Functional (EDF) theory

In the last decades, many studies have been devoted to extend the well known Density Functional Theory (DFT) widely discussed in the context of condensed matter [61, 136] to the nuclear field [44], whereas the distinctive assumption of effective interaction has been done.

The aim of the newly born Energy Density Functional (EDF) theory is to provide an exact reformulation of the initial problem to reproduce the ground state energy and the one-body local density as close as possible to the observed ones.

These functional theories keep the simplicity of the independent particle picture, but they incorporate in an effective way several effects much beyond the pure HF theory.

Indeed, by fitting directly coefficients of the functional on observables that contain all the correlations, the functional theory itself goes much beyond the HF framework. As a result, the functional theory gives more reliable results with respect to pure HF calculations in nuclear matter, which employ the bare nucleon-nucleon interaction [62, 107].

In order to obtain the EDF, one can assume an auxiliary Slater determinant $|\Psi\rangle$ for the many-body wave function so that the energy can be evaluated

by performing the expectation value of the effective Hamiltonian, denoted as $\hat{\mathcal{H}}(\rho)$, with the independent particle state $|\Psi\rangle$ [107]:

$$E = \langle\Psi|\,\hat{\mathcal{H}}(\rho)\,|\Psi\rangle = \int \mathcal{E}(\mathbf{r})d\mathbf{r}, \tag{1.36}$$

where the energy functional $\mathcal{E}$ depends on the parameterization adopted of the effective interaction.

In particular, by employing a Skyrme-like effective interaction Eq. (1.35), as it has been done in our works, this energy functional is written as:

$$\mathcal{E} = \mathcal{K} + \mathcal{E}_0 + \mathcal{E}_3 + \mathcal{E}_{eff} + \mathcal{E}_{fin} + \mathcal{E}_{so} + \mathcal{E}_{sg}. \tag{1.37}$$

Each contribution in the equation above can be of course expressed in terms of the isoscalar $\rho = \rho_n + \rho_p$ and isovector $\rho_3 = \rho_n - \rho_p$ particle density as:

$$\begin{aligned}
\mathcal{K} &= \frac{\hbar^2}{2m}\tau \\
\mathcal{E}_0 &= C_0\rho^2 + D_0\rho_3^2 \\
\mathcal{E}_3 &= \left(C_3\rho^2 + D_3\rho_3^2\right)\rho^\alpha \\
\mathcal{E}_{eff} &= C_{eff}\rho\tau + D_{eff}\rho_3\tau_3 \\
\mathcal{E}_{fin} &= C_{fin}\left(\nabla\rho\right)^2 + D_{fin}\left(\nabla\rho_3\right)^2 \\
\mathcal{E}_{so} &= C_{so}\mathbf{J}\cdot\nabla\rho + D_{so}\mathbf{J}_3\cdot\nabla\rho_3 \\
\mathcal{E}_{sg} &= C_{sg}\mathbf{J}^2 + D_{sg}\mathbf{J}_3^2.
\end{aligned} \tag{1.38}$$

The coefficients C and D with different indices given above are combinations of traditional Skyrme parameters, that is:

$$\begin{aligned}
C_0 &= \frac{3}{8}t_0 & D_0 &= -\frac{1}{8}t_0\left(2x_0+1\right) \\
C_3 &= \frac{1}{16}t_3 & D_3 &= -\frac{1}{48}t_3\left(2x_3+1\right) \\
C_{eff} &= \frac{1}{16}\left[3t_1 + t_2\left(4x_2+5\right)\right] & D_{eff} &= -\frac{1}{16}\left[t_1\left(2x_1+1\right) - t_2\left(2x_2+1\right)\right] \\
C_{fin} &= \frac{1}{64}\left[9t_1 - t_2\left(4x_2+5\right)\right] & D_{fin} &= -\frac{1}{64}\left[3t_1\left(2x_1+1\right) - t_2\left(2x_2+1\right)\right]
\end{aligned}$$

$$C_{so} = \frac{3}{4}W_0 \qquad D_{so} = \frac{1}{4}W_0$$
$$C_{sg} = \frac{1}{32}\left[t_1\left(1-2x_1\right) - t_2\left(1+2x_2\right)\right] \qquad D_{sg} = \frac{1}{32}\left(t_1 - t_2\right). \tag{1.39}$$

One can notice that, by denoting with $\varphi_{i,s,q}$ the single-particle wave function of the i^{th} nucleon of the q type, having spin s, in the coordinate space, the functional constructed by the Skyrme interaction turns to be not a functional of the density $\rho_q = \sum_{i,s} |\varphi_{i,s,q}(\mathbf{r})|^2$ (q = p, n) only, but it also depends on the kinetic energy and spin densities, denoted respectively by τ_q and $\mathbf{J}_q$ and defined as:

$$\tau_q = \sum_{i,s} |\nabla\varphi_{i,s,q}(\mathbf{r})|^2$$
$$\mathbf{J}_q = \sum_{i,s,s'} |\varphi^*_{i,s',q}(\mathbf{r})\nabla\varphi_{i,s,q}(\mathbf{r})|^2 \left\langle s'\right| \sigma \left|s\right\rangle. \tag{1.40}$$

Analogously to the particle density, one has then also defined the isoscalar $(\tau, \mathbf{J})$ and isovector $(\tau_3, \mathbf{J}_3)$ kinetic energy and spin densities in the following way:

$$\tau = \tau_n + \tau_p \qquad \tau_3 = \tau_n - \tau_p$$
$$\mathbf{J} = \mathbf{J}_n + \mathbf{J}_p \qquad \mathbf{J}_3 = \mathbf{J}_n - \mathbf{J}_p. \tag{1.41}$$

1.5 The semi-classical model in nuclear physics

The quantal formalism so far adopted doubtless constitutes a powerful tool to explain a huge number of experimental facts. Actually, performing reliable calculations by implementing codes based on Hartree-Fock, RPA or TDHF is very challenging from the computational point of view. Moreover these methods could not be appropriate to approach some physical situations.

In the last decades, therefore, many theories have been developed to ensure a trustworthly reproduction of several gross nuclear properties, such as the ground state energies, the nuclear radii or the frequencies of the giant resonances, employing methods which could be less computationally demand-

ing.

In atomic physics, the Thomas-Fermi theory [70, 176] has demonstrated to be able to provide truthful results, but it has not been widely applied to the nuclear context in its original version, because of the shortness of the range of nuclear forces [150]. However, the Extended Thomas-Fermi (ETF) version afterwards developed for the stationary case has shown itself that the corresponding semi-classical expressions, representing the different observables on the average, can be a viable alternative to the solution of the full quantum mechanical calculations [29].

The semi-classical procedure can be moreover generalized for the dynamical case, where it can be pointed out that, in the limit for $\hbar \to 0$, the TDHF equation leads to the Vlasov equation, which allows to depict a fluid dynamic description of the giant resonances.

1.5.1 Thomas-Fermi approximation

The Thomas-Fermi (TF) theory, roughly speaking, assumes that the particles at each point in space feel the potential as if it was locally equal to a constant [150]. This corresponds to a break-off at the lowest order in the Taylor series expansion of the self-consistent (Skyrme) Hartree-Fock potential $U(\mathbf{r})$.

Under this assumption, it is demonstrated [29] that the local limit of the TF density and kinetic energy density are given by

$$\rho^{TF}(\mathbf{r}) = \frac{1}{3\pi^2} k_F^3 \Theta\left(\mu - U(\mathbf{r})\right) \qquad \tau^{TF}[\rho] = \frac{3}{5}\left(3\pi^2 \rho^{TF}\right)^{2/3} \tag{1.42}$$

where the local Fermi momentum k_F has been defined as:

$$k_F(\mathbf{r}) = \left[\frac{2m}{\hbar^2}(\mu - U(\mathbf{r}))\right]^{1/2}. \tag{1.43}$$

The Lagrangian multiplier μ coincides with the Fermi energy and is fixed by the conservation of the number of particles $\mathcal{N}$:

$$\mathcal{N} = \int d^3\mathbf{r} \rho^{TF}(\mathbf{r}). \tag{1.44}$$

Because the TF approximation, the density matrix loses some feature of the exact one, such as the property to be idempotent. Moreover, as a difference with respect to the HF method, when one makes a variational calculation with semiclassical densities, it is required the additional condition Eq. (1.44) to fix the number of particles.

Actually, the TF approximation can also be obtained by expanding in terms of $\hbar$ the Bloch function (see [29]) and taking only the lowest order ($\hbar \to 0$); retaining all terms up to the second order in $\hbar$ one can deduce the Extended Thomas Fermi mentioned above.

1.5.2 Semi-classical limit of TDHF: the Vlasov equation

In order to develop the semi-classical limit of the TDHF equation Eq. (1.24), we should recall the fundamental concept of Weyl transform [42, 193], which converts an arbitrary operator in a function of $\mathbf{r}$ and $\mathbf{p}$.

The starting point of this approach is in fact the definition of the so-called Wigner function $f(\mathbf{r}, \mathbf{p})$

$$f(\mathbf{r}, \mathbf{p}) = \frac{1}{h^3} \int e^{-i\frac{\mathbf{p}\cdot\mathbf{R}}{\hbar}} \langle \mathbf{r} + \frac{\mathbf{R}}{2} | \, \hat{\rho} \, | \mathbf{r} - \frac{\mathbf{R}}{2} \rangle \, d\mathbf{R}, \tag{1.45}$$

which is nothing but the Weyl transform of the one-body density operator $\hat{\rho}$ already defined for example in Eq. (1.8).

By taking the time derivative of Eq. (1.45) and making use of the THDF equation, one easily gets (see section A.3):

$$\begin{aligned} \frac{\partial f}{\partial t} &= \frac{1}{i\hbar} \frac{1}{h^3} \int e^{-i\frac{\mathbf{p}\cdot\mathbf{R}}{\hbar}} \langle \mathbf{r} + \frac{\mathbf{R}}{2} | \left[\hat{T} + \hat{U}, \hat{\rho} \right] | \mathbf{r} - \frac{\mathbf{R}}{2} \rangle \, d\mathbf{R} \\ &= \left(\frac{\partial f}{\partial t} \right)_1 + \left(\frac{\partial f}{\partial t} \right)_2 \end{aligned} \tag{1.46}$$

where the terms connected respectively with one or two-body contributions have been distinguished.

In Appendix A.3, it is found that the one-body term is given by

$$\left(\frac{\partial f}{\partial t}\right)_1 = -\frac{\mathbf{p}}{m} \cdot \nabla_{\mathbf{r}} f, \tag{1.47}$$

while the second addend is evaluated as

$$\left(\frac{\partial f}{\partial t}\right)_2 = \frac{2}{\hbar} \sin\left(\frac{\hbar}{2} \nabla_{\mathbf{r}} U \cdot \nabla_{\mathbf{p}} f\right). \tag{1.48}$$

The semi-classical approximation consists in taking only the first order term, in the expansion of the right-hand side of the previous Eq. (1.48) as power of $\hbar$, leading to:

$$\left(\frac{\partial f}{\partial t}\right)_2 = \frac{2}{\hbar}\left(\frac{\hbar}{2} \nabla_{\mathbf{r}} U \cdot \nabla_{\mathbf{p}} f + o\left(\hbar^3\right)\right) \xrightarrow{\hbar \to 0} \nabla_{\mathbf{r}} U \cdot \nabla_{\mathbf{p}} f \tag{1.49}$$

and so definitely, from the Eq. (1.46), one obtains the well-known collisionless BNV equation [98], i.e. the Vlasov equation [187]

$$\frac{\partial f}{\partial t} + \frac{\mathbf{p}}{m} \cdot \nabla_{\mathbf{r}} f - \nabla_{\mathbf{r}} U \cdot \nabla_{\mathbf{p}} f = 0. \tag{1.50}$$

In thisl limit, f is real and has the physical meaning of a distribution function allowing for further semiclassical developements in the direction of adding correlations in the time dependent picture.

We remark here that, while the one-body part is entirely classical in that it contains no terms in $\hbar$, the two-body contribution has generally a non-negligible quantum correction. The semi-classical approximation becomes however exact if all the derivatives of U higher than the second order are zero, as it happens for example for a free particle, a constant force or an harmonic oscillator.

One sees that the collisionless BNV equation is equivalent to the Liouville equation for the classical distribution function in the phase-space

$$\frac{df(\mathbf{r}, \mathbf{p}, t)}{dt} = 0 \tag{1.51}$$

which expresses the balance in time between the incoming and the outgoing amount of particles in a given classical volume of this space.

This is doubtless true for a gas of independent particles interacting with a mean-field but without any genuine two-body collisions, coherently with the hypothesis of the starting TDHF theory.

Otherwise, a collision term should be introduced on the right-hand side of the Eq. (1.50), which returns the following BNV equation

$$\frac{\partial f}{\partial t} + \frac{\mathbf{p}}{m} \cdot \nabla_{\mathbf{r}} f - \nabla_{\mathbf{r}} U \cdot \nabla_{\mathbf{p}} f = I_c(f) \tag{1.52}$$

where $I_c(f)$ is a nonlinear integral operator in f. This collision term can be obtained again in the semi-classical limit from the corresponding quantal term neglected in deriving the TDHF equations [101].

1.6 Thermodynamics and phase transitions of nuclear matter

Within the framework given by the mean-field treatment, the investigation of nuclear systems can be even addressed from a thermodynamical point of view, by exploiting EDF based on Skyrme-like forces [63]. Many efforts have been dedicated in the last decades to the study of thermodynamics and phase transitions both in finite nuclei [48, 166] and in (infinite) nuclear matter [167]. In this section, in particular, we investigate the thermodynamical behavior of this latter nuclear medium by omitting the Coulomb interaction and so dealing with that as a mixture of neutrons and uncharged protons. Such idealized systems are indeed useful for understanding the bulk properties of large nuclei. Although nuclear matter calculations are never realistic for any nuclear system, they can be extended (in the semiclassical limit) to include the Coulomb force between protons and treat finite nuclei and thus to be used in realistic calculations of the neutron star crust (see Chapter 3).

1.6.1 Equilibrium properties: Equation of State (EoS)

The most important ingredient to describe the equilibrium properties of nuclear matter, as for any thermodynamical system, is the knowledge of the so-called Equation of State (EoS), that is a mathematical relation which determines the general connection between two or more thermodynamical quantities, such as energy, density and temperature. [3]

The research for an EoS for nuclear matter is essential in many branches of modern nuclear physics, ranging from nuclear structure [16, 141], to the modeling of compact stellar objects [65, 147].

It is therefore really interesting to broaden our awareness on the behavior of the nuclear matter even apart from the density conditions corresponding to the saturation in nuclei.

In the last decade, in particular, the perspectives offered by nuclear astrophysics and the possibility to take advantage of the new radioactive beams for nuclear reactions has stimulated a growing interest in the isospin degree of freedom and so in the behavior of the asymmetric nuclear matter (ANM). Many investigations have been in particular concentrated on the isovector part of the effective interaction, which depends on the difference between the densities of the two nuclear species, and on the corresponding term in the nuclear EoS, the so-called symmetry energy [113, 153, 177]. Such a term is widely discussed in the description of heavy ion collisions [14, 50, 77] and also in astrophysics, as far as the modeling of supernova explosions and neutron

[3] Schematically one can define two different situations in nuclear physics where the temperature is a perfectly well defined theoretical concept:

- temperature and all related thermal quantities naturally emerge in quantum statistical mechanics when the system is complex enough that the exact quantum microstate cannot be known exactly, as it occurs for isolated nuclei in the laboratory, when they are excited by a nuclear reaction into the continuum well above the particle separation energy [12];
- the nuclei are in a thermal bath, that is they are immersed in an external hot environment, as in astrophysical sites in the cosmos. In this case one can safely assume that the nuclear system is in thermodynamic equilibrium, meaning that the temperature of the environment can be equalized to the nuclear temperature [87].

Once its definition has been clarified, in the following discussion, the temperature will be introduced and treated as an external parameter.

stars is concerned [34, 113, 171].

Symmetry energy. The general expression for the energy per nucleon in ANM is based on the empirical parabolic dependence on the asymmetry parameter $I = \frac{\rho_n - \rho_p}{\rho_n + \rho_p}$ [123]:

$$\frac{E}{A}(\rho, I) \approx \frac{E}{A}(\rho, I = 0) + \frac{E_{sym}}{A}(\rho) I^2, \tag{1.53}$$

that is it can be seen as an expansion in power of I, where the higher order terms are usually neglected.

The symmetry energy per nucleon can so be defined as

$$\frac{E_{sym}}{A}(\rho) = \frac{1}{2} \frac{\partial^2}{\partial I^2} \frac{E}{A}(\rho, I) \bigg|_{I=0} \tag{1.54}$$

and, if the parabolic approximation holds, it can be evaluated as the difference between the energy per nucleon for the pure neutron matter ($I = 1$) and symmetric nuclear matter (SNM) ($I = 0$).

Around a reference density ρ_0 moreover, the symmetry energy is usually expanded in terms of $\chi = \frac{\rho - \rho_0}{\rho_0}$ as [201]

$$E_{sym}(\rho) = E_{sym}(\rho_0) + \frac{L(\rho_0)}{3} \chi + \frac{K_{sym}(\rho_0)}{18} \chi^2 + o(\chi^3) \tag{1.55}$$

where $L(\rho_0) = 3\rho_0 \frac{\partial E_{sym}}{\partial \rho}|_{\rho=\rho_0}$ and $K_{sym}(\rho_0) = 9\rho_0^2 \frac{\partial^2 E_{sym}}{\partial \rho^2}|_{\rho=\rho_0}$ are the density slope and curvature parameters, which characterize the density dependence of the symmetry energy around ρ_0. Unfortunately, the symmetry energy is not well constrained from experimental knowledge far from the density values around normal condition at $\rho_0 \sim 0.16$ fm^{-3} and hence it exists a large uncertainty on its value and slope, when one deviates from the saturation value. The symmetry energy per nucleon for a Skyrme type EoS can be in fact expressed as

$$\frac{E_{sym}}{A}(\rho) = \frac{\epsilon_F}{3} + D_0 \rho + D_3 \rho^{\alpha+1} + \frac{2m}{\hbar^2} \left(\frac{C_{eff}}{3} + D_{eff} \right) \epsilon_F \rho \equiv \frac{\epsilon_F}{3} + C_{pot}(\rho) \tag{1.56}$$

that is a sum of a kinetic contribution and of a potential part[4].

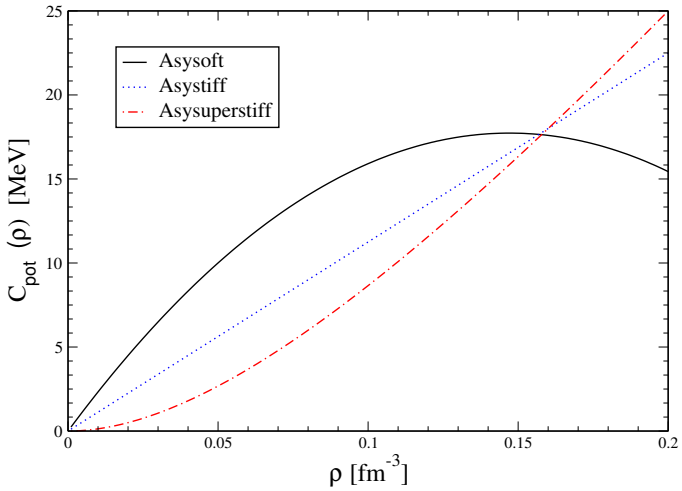

Figure 1.2: Different density parameterizations for the potential part of the symmetry energy.

The former, coming from the Pauli principle, turns to be model-independent and can be exactly evaluated. For the latter one, contrariwise, many functional form have been proposed, with some constraints given by experiments on structure and reactions. One of these constraints is that symmetry energy has to reproduce the a_I coefficient of the Bethe-Weizsäcker mass formula [56] (see eq. Eq. (2.2) in section 2.1), which is well-known with a reasonable experimental accuracy. As alarge variety of predictions of its density dependence have been formulated and many efforts to find some possible sensitive observables (such for instance collective flows, isospin diffusion, light cluster emission) have been performed [46, 106, 155].

However, the final word seems to be still far from getting. For that reason, many effective interactions, which are rather different in the isovector channel such as those plotted in Fig. 1.2, have been taken into account so far. Looking at the Fig. 1.2, one can suddenly notice how, generally speaking, different parameterizations of $C_{pot}(\rho)$ converge below saturation density ρ_0. This contribution, being positive, is wherever repulsive, so that the system will tend to reduce the asymmetry, enhancing the attraction between neutrons and protons.

[4]For sake of simiplicity, the kinetic term has been written by considering the zero temperature case, and by denoting with $\epsilon_F = \frac{\hbar^2 k_F^2}{2m}$ the Fermi energy at density ρ.

1.6.2 Stability of the system: free-energy curvature

Regardless of the effective interaction adopted, the EDF theory provides a way to extract, in a given statistical ensemble, the corresponding thermodynamical potential. It is known from statistical mechanics that the stability of a thermodynamical system is completely characterized through the study of the curvature of its potential [47]. [5]

For example, for a nuclear system characterized by a given value of the temperature T and fixed particle number A, the thermodynamical potential will be given by the Helmotz free-energy $F = E - TS$, where S is the total entropy of the system.[6] By fixing the neutron and proton numbers, N and Z respectively, in the thermodynamical limit, viz:

$$\frac{N}{V} \xrightarrow{N,V\to\infty} \rho_n, \qquad \frac{Z}{V} \xrightarrow{Z,V\to\infty} \rho_p, \tag{1.59}$$

the free-energy comes out to be proportional to the volume and so the chemical potentials can be evaluated, according to their definition, as:

$$\mu_n \equiv \frac{\partial F}{\partial N} = \frac{\partial \mathcal{F}}{\partial \rho_n}, \qquad \mu_p \equiv \frac{\partial F}{\partial Z} = \frac{\partial \mathcal{F}}{\partial \rho_p} \tag{1.60}$$

where $\mathcal{F} = F/V$ is the free-energy density. In this framework, if one wants to analyze the stability of the system in the space of particle density fluctu-

[5] In order to ensure that an extremum configuration $[\bar{X}_1, \bar{X}_2, \ldots, \bar{X}_k]$ be stable for a given functional W of the thermodynamical parameters $\{X_i\}_{i=1}^k$, one must insist that it has a minimum in correspondence of that, which in turn requires the second-order variation to be positive definite:

$$0 < \sum_{i,j=1}^{k} \frac{\partial^2 W_i}{\partial X_i \partial X_j}\bigg|_{\mathbf{X}_i=\bar{X}_i} \delta X_i \delta X_j, \tag{1.57}$$

or, equivalently, if and only if the curvature matrix $\mathbf{C}_{ij}^W = \frac{\partial^2 W_i}{\partial X_i \partial X_j}$ has only positive eigenvalues.

[6] According to its usual definition in statistical mechanics, denoting by k_B the Boltzmann constant, the entropy of the system is defined as [98]

$$S = k_B \ln \sum_{\{n_i\}} \Gamma\{n_i\}, \tag{1.58}$$

so it essentially depends on the number of states of the system which corresponds to the occupation number $\{n_i\}$.

ations, one must look at the following curvature matrix $\mathbf{C}$, that is:

$$\mathbf{C} = \begin{pmatrix} \partial\mu_n/\partial\rho_n & \partial\mu_n/\partial\rho_p \\ \partial\mu_p/\partial\rho_n & \partial\mu_p/\partial\rho_p \end{pmatrix}. \tag{1.61}$$

The two eigenvectors of the curvature matrix Eq. (1.61) correspond to the normal oscillation modes of the system in the space of density fluctuations. In SNM, these two modes, labeled as isoscalar or isovector mode depending on whether the two nuclear species move in or out of phase respectively, are fully decoupled. This characterization does not strictly hold anymore in ANM case, where because of the asymmetry of the matter, the two species cannot oscillate with the same amplitude, even if they can still move in phase (isoscalar-like) or out of phase (isovector-like), and this leads to a coupling between the two normal modes [13].

1.6.3 Liquid-gas phase transition: spinodal instability

In the general context of many-body systems, another common feature is the possible occurence of different kinds of phase transitions. Since nuclear forces have an attractive finite-range part and a repulsive hard core, the nuclear matter resembles a Van der Waals fluid. As a consequence, in analogy with the latter system, for homogeneous nuclear matter at sub-saturation density and relatively low temperature, a liquid-gas phase transition (p.t.) is expected to appear, driven by the instability exhibited by the mean-field [47]. In ANM at a fixed temperature T, it emerges therefore the occurence of matter instabilities, associated to the region where the free-energy density is concave at least in one direction. This ensemble of unstable points where the lower eigenvalue of the curvature matrix is negative, is known in literature as spinodal region [14].

In this region of the phase diagram, an homogeneous infinite system exhibits therefore a mechanical instability associated to a region of negative matter incompressibility K,[7] which leads to a phase separation; this can explain why the liquid-gas phase transition has been considered as a good

[7]The incompressibility of the nuclear matter is related to the curvature of the EoS and

candidate to interpret the mechanism responsible for the production of intermediate mass fragment (IMF) producted in heavy ion collisions at Fermi energies ($\sim 30 \div 50$ MeV/A) [28]. Such a process is also closely linked to the occurrence of clustering phenomena in the inner crust of neutron stars [86, 110, 179].

Inside the spinodal region of ANM, moreover, the mixing between the two modes leads also to a re-assembling of the chemical composition of the two phases on which the system tends to separate, so that the higher density phase (liquid) becomes more symmetric than the low-density one (gas). This phenomenon, known as isospin distillation mechanism [13] is significantly influenced by the symmetry energy and it will be discussed more in detail in the next chapter. Lastly, it is useful to underline that the spinodal instability discussed above is a general phenomenon in many-body systems, rather than merely an artifact of the mean-field approximation adopted in this chapter.

can be defined at saturation density as:

$$K(\rho_0) = 9\rho_0^2 \frac{\partial^2 E/A(\rho)}{\partial \rho^2}\bigg|_{\rho=\rho_0} \tag{1.62}$$

Chapter 2

Superfluidity in nuclear matter: pairing correlations

This chapter is entirely dedicated to the investigation of one characteristic phenomenon of many-body systems, which has been intensively studied in several domains of physics: superfluidity. In the next sections, this concept is analyzed starting from the experimental evidences from which the existence of pairing correlations is inferred, until the main theoretical schemes developed for its interpretation.

A modification of the HF theory, presented in Chapter 1, is going to be introduced, in order to take into account in a consistent formalism this kind of correlations. Correspondingly, the Hartree-Fock-Bogolioubov (HFB) theory is discussed, together with an important approximation: the Bardeen-Cooper-Schrieffer (BCS) theory, that has proven to be extremely successful in describing the superconducting phenomena in condensed matter.

Similarly to what it was shown in the first chapter, the discussion is then extended to the dynamical case, in order to highlight the changes that pairing may establish, albeit incorporating these correlations in a time dependent mean field theory.

Once the contribution of the pairing interaction to the EDF is determined, the last part of this chapter is finally focused on the analysis of the pairing role in characterizing the thermodynamical (spinodal) instability exhibited

by nuclear matter in the low density region, up to moderate temperatures.

2.1 Experimental evidences of pairing in nuclei

Pairing correlations constitute a kind of particle-particle correlations, which occur under suitable conditions in fermionic systems and whose existence have historically been deduced by several experimental facts. It is therefore useful to have a brief digression on the most relevant results revealing the emergence of this coupling in nuclear many-body systems.

The gap in the energy spectrum. A first interesting issue which has been dealt by using the idea of pairing is the energy gap observed in the spectrum of excitation energies of some nuclei. Considering for example a nucleus with an even number of protons Z, its spectrum shows remarkable differences depending on whether its mass number A is odd or even.

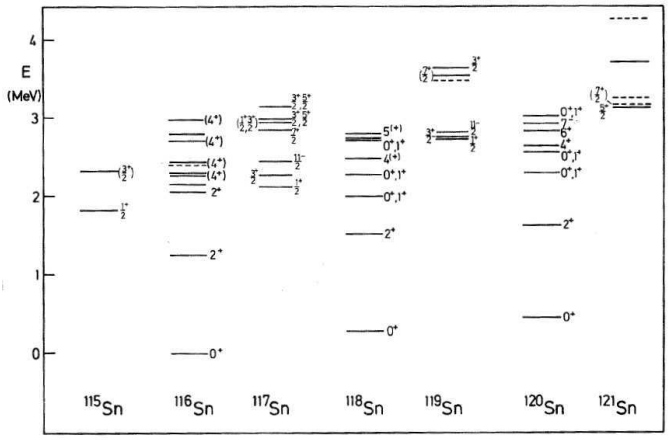

Figure 2.1: Spectrum of excitation energies for Sn isotopes, see [150, p. 218].

It is observed that, starting from the ground state, even-even nuclei have only few collective levels up to 1.5 MeV of excitation energy; conversely, even-odd nuclei have many excited states of both collective and independent particle nature in the same energy range. This is clearly exemplified by Fig. 2.1, where this gap is shown for different tin isotopes. Such abnormal behavior has a simple explanation by admitting the presence of pairing correlations: whereas in even-odd nuclei the unpaired nucleon can easily be excited above the Fermi surface; in even-even nuclei, nucleons are coupled and so to excite the system it is necessary

to provide the energy to break up the couple, or alternatively to excite the couple itself.

Odd-even effect. Another relevant experimental evidence for the existence of the pairing interaction is the renowned odd-even effect in the neutron and proton separation energy.

It is experimentally found that the binding energy[1] of an even-odd nucleus is lower than the average binding energies of the two even-even neighboring nuclei. It is known, in fact, that the binding energies are well reproduced by the semi-emipirical mass formulas, such as that one tuned by Bethe and Weizsäcker [56]:

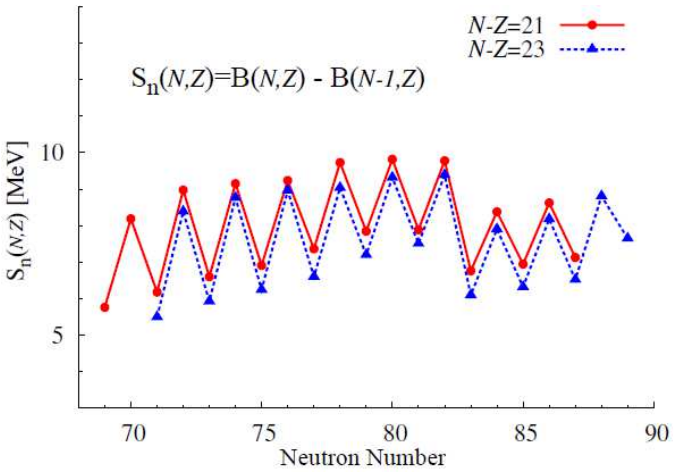

Figure 2.2: Neutron separation energy $S_n(N, Z)$ as a function of the neutron number N, taken from [67].

$$B(A, Z) = a_V A + a_S A^{2/3} + a_C \frac{Z^2}{A^{1/3}} + a_I \frac{(N - Z)^2}{A} + \Delta(A). \tag{2.2}$$

In the latter expression together with volume, surface, Coulomb and symmetry term, denoted by a_V, a_S, a_C and a_I respectively, one notices the presence

[1]The binding energy $B(A, Z)$ of a nucleus, in a units reference frame where the light speed $c = 1$, as it is known, is given by this formula

$$B(A, Z) = ZM_p + NM_n - M(A, Z), \tag{2.1}$$

with M_n and M_p referring to the neutron and proton mass, respectively, while M is the total mass of the (A, Z) nucleus.

of a pairing term, labeled with $\Delta(A)$ such that

$$\Delta(A) = \begin{cases} \Delta & \text{even-even nuclei} \\ 0 & \text{even-odd nuclei} \\ -\Delta & \text{odd-odd nuclei,} \end{cases} \tag{2.3}$$

where Δ is a mass dependent positive number, which is accountable for the staggering behavior shown in Fig. 2.2. Since the semi-empirical mass formula Eq. (2.2), for a fixed A value, has a quadratic dependence in Z, it produces a single parabola for isobars with odd number of mass; but, because of the pairing term, it also determines two parabolas for nuclei with equal A, one for even-even nuclei and the other in the odd-odd configuration, exactly as it is observed in the experiments [3].

Moment of inertia and deformation in nuclei. Also the experimental data concerning moment of inertia of nuclei can be reproduced only under the hypothesis of paired nucleons in a nucleus (see Fig. 2.3).

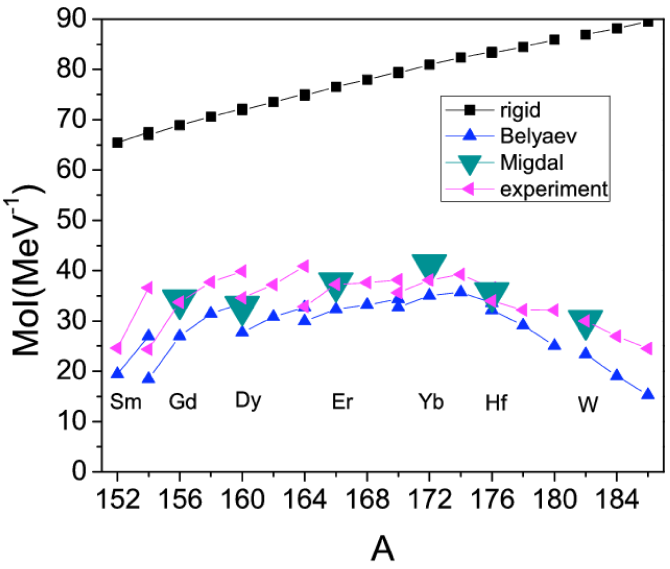

Figure 2.3: Moments of inertia of deformed nuclei as a function of mass number A in the so-called rare-earth region ($150 < A < 190$). Experimental data are compared with theoretical calculations including pairing correlations or assuming a rigid rotator (readapted from [73]).

Furthermore, the moment of inertia of even-even nuclei is always lower than the corresponding value for the neighboring even-odd nuclei. Owing to pairing correlations, it is intuitive to expect that a system formed by

couples of nucleons has surely a more compact geometrical shape than one with unpaired nucleons.

Concerning the deformation, instead, from the experiments it emerges that nuclei, whose mass number do not deviate too much from the closed shell configuration still preserve an approximately spherical symmetry in their ground state, as an evidence of pairing correlations.
In conclusion, all experimental results reviewed in this section indicate the existence of a two-body attractive interaction, accountable for the formation of nucleon pairs. These couples, named as Cooper pairs, show a close resemblance to those determining the phenomenon of superconductivity in metals.

2.2 Hartree-Fock-Bogolioubov (HFB) theory

It has been already stressed in Chapter 1 that many properties of nuclei can be explained adopting a model of independent particles moving in an average potential. Under this assumption, in the first chapter, looking for a wave function describing the ground state of the nucleus and restricting ourselves to an independent single-particle product ansatz (Slater determinant), the Hartree-Fock method was developed just minimizing the total energy of the system. However, in order to extend this framework and to take into account the effect of the pairing, one must consider, still within a mean-field approach, a more general many-body wave function than a Slater determinant.

The Hartree-Fock-Bogoliubov (HFB) theory generalizes the HF method by introducing the concept of the so-called Bogoliubov "quasi-particles" [23]. The basic idea is to represent the ground state $|\Phi\rangle$ of a nucleus as a vacuum for these quasi-particles:

$$\hat{\beta}_k |\Phi\rangle = 0, \tag{2.4}$$

where $\hat{\beta}_k$ and its adjoint $\hat{\beta}_k^\dagger$ are the quasi-particle operators, which are connected to the creation and annihilation operator defined in section 1.2.2 by

the Bogoliubov linear transformations:

$$\begin{cases} \hat{\beta}_k &= \sum_i \left(u^*_{ik} \hat{a}_i + v^*_{ik} \hat{a}^\dagger_i \right) \\ \hat{\beta}^\dagger_k &= \sum_i \left(v_{ki} \hat{a}_i + u_{ki} \hat{a}^\dagger_i \right) . \end{cases} \tag{2.5}$$

The latter system can be rewritten in a matrix form as

$$\begin{pmatrix} \hat{\beta} \\ \hat{\beta}^\dagger \end{pmatrix} = \begin{pmatrix} u^\dagger & v^\dagger \\ v^T & u^T \end{pmatrix} \begin{pmatrix} \hat{a} \\ \hat{a}^\dagger \end{pmatrix} = \mathcal{W}^\dagger \begin{pmatrix} \hat{a} \\ \hat{a}^\dagger \end{pmatrix} , \tag{2.6}$$

where the matrix $\mathcal{W}$

$$\mathcal{W} = \begin{pmatrix} u & v^* \\ v & u^* \end{pmatrix} , \tag{2.7}$$

must satisfy the unitary constraint: $\mathcal{W}\mathcal{W}^\dagger = \mathcal{W}^\dagger\mathcal{W} = \mathbb{1}$. Even if the Bogoliubov transformations written in Eq. (2.5) do not uniquely define the HFB wave function $|\Phi\rangle$, it is possible to demonstrate [150] that this uniqueness is preserved in the definition of the following quantities:

$$\rho_{ij} = \langle \Phi | \, \hat{a}^\dagger_j \hat{a}_i \, | \Phi \rangle , \qquad \kappa_{ij} = \langle \Phi | \, \hat{a}_j \hat{a}_i \, | \Phi \rangle , \tag{2.8}$$

where ρ_{ij} has the same form identified in Eq. (1.8) and is denominated hereafter as normal density, to be distinguished from κ_{ij}, which is referred as abnormal (pairing) density.

The Bogoliubov transformations violate the symmetry related to the particle number conservation so that, in order to preserve this symmetry, one should correspondingly modify the Hamiltonian operator $\hat{H}$ defined in Eq. (1.11) as:

$$\hat{H}' = \hat{H} - \mu \hat{\mathcal{N}}, \tag{2.9}$$

where $\hat{\mathcal{N}}$ is the number operator, and μ is a Lagrangian multiplier which, by its definition, coincides with the chemical potential.

Analogously as it has been done in Eq. (1.14), the total energy of the system, namely the expectation value of the (grancanonical) Hamiltonian

Eq. (2.9), can be derived as a functional of both densities defined above:

$$E^{\mathrm{HFB}}[\rho,\kappa] = \sum_{ij}\left[\left(T_{ij} - \mu\delta_{ij} + \frac{1}{2}U_{ij}\right)\rho_{ji} + \frac{1}{2}\Delta_{ij}\kappa^*_{ji}\right], \tag{2.10}$$

where the pairing field $\hat{\Delta}$, added to the self-consistent field $\hat{U}$, is defined as

$$\Delta_{ij} = \frac{1}{2}\sum_{kl}\bar{V}_{ijkl}\kappa_{kl}. \tag{2.11}$$

The fields introduced above account for different contributions: the field $\hat{U}$ accounts for all the long range *ph*-correlations, while $\hat{\Delta}$ contains the short-range pairing correlations responsible for the superfluid state.

Similarly to the HF case, one can make the variation with respect to the normal and abnormal densities and, by employing the Rayleigh-Ritz principle, one finds the well-known HFB equations:

$$\begin{pmatrix} h-\mu & \Delta \\ -\Delta^* & -h^*+\mu \end{pmatrix}\begin{pmatrix} u_k \\ v_k \end{pmatrix} = E_k \begin{pmatrix} u_k \\ v_k \end{pmatrix}, \tag{2.12}$$

where this extension of the definition of single particle hamiltonian h_{ij} given in Eq. (1.17) has been applied

$$h_{ij} = \left.\frac{\partial E[\rho,\kappa]}{\partial\rho_{ij}}\right|_{\kappa}. \tag{2.13}$$

It could be interesting to put these equations in a more compact form. This is possible by defining a generalized density matrix $\mathcal{R}$

$$\mathcal{R} = \begin{pmatrix} \rho & \kappa \\ -\kappa^* & \mathbb{1}-\rho^* \end{pmatrix}, \tag{2.14}$$

which is hermitian and idempotent, as a mere algebraic calculation shows. Denoted as $\mathcal{H}$ the matrix involved in the r.h.s. of the Eq. (2.12)

$$\mathcal{H} = \begin{pmatrix} h-\mu & \Delta \\ -\Delta^* & -h^*+\mu \end{pmatrix}, \tag{2.15}$$

in the basis corresponding to the operator $\hat{\beta}_k$, both matrices $\mathcal{H}$ and $\mathcal{R}$ are diagonal, so that the HFB equations become

$$[\mathcal{H}, \mathcal{R}] = 0, \tag{2.16}$$

as in the formulation presented in Eq. (1.20) for the HF theory.

Although HF and HFB equations look formally the same, some important differences exist in their resolution. On the one hand, in fact, it has been already mentioned that HFB equations require an additional constraint to impose the conservation of the average number of particles, which is automatically preserved in HF theory. On the other hand, while in the HF ground state only the first A energy levels are involved and so necessarily implemented in the resolution, in the HFB one should take into account also the states above the Fermi level, because they can be populated by the quasiparticles. The computational time one needs to solve HFB equations is hence much larger than the corresponding HF one.

2.2.1 Bardeen-Cooper-Schrieffer (BCS) approximation

An intermediate approximation between HF and HFB, which can reduce the complexity of the calculations is given by the well-known Bardeen-Cooper-Schrieffer (BCS) approximation [17].

The BCS theory has been historically a significant development of the HF method. Although it is not fully adequate for nuclei, the BCS approximation is the correct mean-field limit for infinite matter. As provided by this theory, the state with the lowest energy is constitued only by Cooper pairs, since the coupling between the two particles leads to a decrease in the energy of the system; this variation exceeds also the increase in the kinetic energy caused by the unavoidable occupation of states with energy higher than the Fermi level.

Because of pairing the occupation numbers for hole and particle states, u_k and v_k respectively, are unknown, id est they become variational parameters one should evaluate, contrarily to the HF case where are known a priori.

The basic idea of the BCS method is to suppose that the pairing field

matrix Δ_{ij} couples only conjugate states $(i, \bar{i})$, that are states with the same quantum numbers except for the opposite projection of the angular momentum:

$$\Delta_{ij} \approx \Delta_{i,\bar{i}} \equiv \Delta_i. \tag{2.17}$$

In order to make easier the discussion, one can limit to even-even nuclei. Under this assumption, the variational ansatz for the BCS ground state of a superfluid even-even nucleus can be written as

$$|\mathrm{BCS}\rangle = \prod_{i>0} \left(u_i + v_i \hat{a}_i^\dagger \hat{a}_{\bar{i}}^\dagger \right) |0\rangle \,, \tag{2.18}$$

where, as anticipated above, u_i and v_i are arbitrary variational parameters, with the only one constraint given by the vector normalization:

$$\left|u_i\right|^2 + \left|v_i\right|^2 = 1. \tag{2.19}$$

The sign of i is determined by the projection of the angular momentum, so that for each state with $i > 0$, it exists a conjugate state $\bar{i} < 0$ and vice versa; the product in Eq. (2.18) can be therefore restricted only to half of the whole single-particle space.

In the basis where the density matrix ρ_{ij} is diagonal, the expected value of the Hamiltonian Eq. (2.9), in analogy with the corresponding HFB functional derived in Eq. (2.10) can be written as:

$$E^{\mathrm{BCS}} = \sum_i \left(T_{ii} - \mu + \frac{1}{2} U_{ii} \right) v_i^2 - \sum_{i>0} \Delta_i u_i v_i, \tag{2.20}$$

where the quantity

$$\Delta_i = -\sum_{j>0} \bar{V}_{i\bar{i}j\bar{j}} u_j v_j \tag{2.21}$$

denotes the energy gap of the superfluid state, that means the energy owned by the Cooper pair as a consequence of the pairing introduced.

As usually the variational parameters are obtained after the energy minimization, that is performed by maintaining constant the normalization given

in Eq. (2.19). A straightforward algebraic calculation leads to:

$$v_i^2 = \frac{1}{2}\left(1 - \frac{\xi_i}{\sqrt{\xi_i^2 + \Delta_i^2}}\right) \tag{2.22}$$

$$u_i^2 = \frac{1}{2}\left(1 + \frac{\xi_i}{\sqrt{\xi_i^2 + \Delta_i^2}}\right), \tag{2.23}$$

with ξ_i defined by

$$\xi_i = T_{ii} - \mu_i^*, \tag{2.24}$$

where T_{ii} is the single-particle kinetic energy, while the effective chemical potential μ_i^* writes in terms of the mean field U_{ii} as

$$\mu_i^* = \mu - U_{ii}. \tag{2.25}$$

The definitions given above allow us to rewrite the gap in this way

$$\Delta_i = -\frac{1}{2}\sum_{j>0} \bar{V}_{i\bar{i}j\bar{j}} \frac{\Delta_j}{\sqrt{\xi_j^2 + \Delta_j^2}}. \tag{2.26}$$

The latter equation is known in literature as the gap equation and it is solved together with that one preserving the conservation of the average number $\mathcal{N}$ of particles:

$$\mathcal{N} = 2\sum_{j>0} v_j^2 = \sum_{j>0}\left(1 - \frac{\xi_j}{\sqrt{\xi_j^2 + \Delta_j^2}}\right), \tag{2.27}$$

where the coefficient 2 in front of the summation accounts for the spin degeneracy.

The system constituted by the equations Eq. (2.26) and Eq. (2.27) is closed, since it has a number of equations exactly equal to the number of quantities one needs to calculate (the gap of each state and the chemical potential). In spite of it, that system is not easy to solve, because the two equations are coupled. The self-consistency inherently exhibited by the system requires therefore the adoption of an iterative solution, which will be developed in section 2.4.2 and will lead to several applications in the next

chapters.

By exploiting the microscopic ab-initio calculations for the gap, the BCS theory can in fact be used to have a (quasi)-exact treatment of infinite matter and allow extrapolations to be able to treat dynamics.

2.3 Time Dependent Hartree Fock Bogoliubov (TDHFB) theory

The derivation of the TDHFB equations fully traces the procedure followed in Appendix A.2 in the case of the TDHF theory. The only difference obviously regards the presence of the abnormal pairing density κ_{ij} and so all the terms where it is involved.

In Appendix A.4, it is determined the temporal evolution of both normal and abnormal densities and the result is shown in these equations:

$$\begin{aligned} i\hbar\dot{\rho} &= [h, \rho] + \kappa\Delta^* - \Delta\kappa^* \\ i\hbar\dot{\kappa} &= h\kappa + \kappa h^* + \Delta\left(\mathbb{1} - \rho^*\right) - \rho\Delta \end{aligned} \tag{2.28}$$

By repeating the procedure for their hermitian matrices, at the end one obtains the well-known TDHFB equations:

$$i\hbar\frac{\partial\mathcal{R}}{\partial t} = [\mathcal{H}, \mathcal{R}]\,, \tag{2.29}$$

where $\mathcal{H}$ and $\mathcal{R}$ are the matrices defined in Eqs. (2.14) and (2.15) and whose time-independent case trivially coincides with the Eq. (2.16).

A weak point of the TDHFB theory is without any doubt the computational cost of its implementation. A reasonable estimation of the time consumed by a TDHFB code is two or three orders of magnitude higher than the one of a TDHF numerical calculation [163]. As a consequence, very few TDHFB applications employing realistic interactions have been done so far, usually adopting restrictions on the model space [92, 175]. Conversely, several approximated methods have been developed with the aim to reduce the computational time.

2.3.1 Canonical-basis (Cb-TDHFB) approximation

A reliable and successful method to save computational time is for example based on the Canonical-basis TDHFB (Cb-TDHFB) approximation. Starting from the TDHFB equations Eq. (2.28), the derivation of the Cb-TDHFB equations is based on the possibility to express the normal and abnormal density matrices in the orthonormal canonical basis and, in the same basis, on taking into account only the diagonal part of the pair potential [68]. Under these assumptions, the Cb-TDHFB equations are written in the following way:

$$\begin{aligned} i\hbar\frac{\partial\varphi_k(t)}{\partial t} &= (h[\rho](t) - \eta_k(t))\,\varphi_k(t) \\ i\hbar\frac{\partial\eta_k(t)}{\partial t} &= \kappa_k(t)\Delta_k^*(t) - \Delta_k(t)\kappa_k^*(t) \\ i\hbar\frac{\partial\kappa_k(t)}{\partial t} &= \kappa_k(t)\,(\eta_k(t) + \eta_{\bar{k}}(t)) + \Delta_k(t)(2\eta_k(t) - 1), \end{aligned} \tag{2.30}$$

where $\varphi_k(t)$ is single-particle wave function as defined in Eq. (1.40), while $\eta_k(t)$ is an arbitrary time-dependent function, whose value does not influence the evolution of the other observables.[2] Moreover, one should underline that, in the stationary limit, the Cb-TDHFB approach is completely equivalent to the ordinary BCS approximation.

The resolution of these TDHF+BCS equations will be then faced in Chapter 5, in order to address the dynamical effects of the pairing correlations.

2.3.2 Quasi-particle RPA and semi-classical methods

Although they are not used in the present work, one should mention some other important methods developed to describe the collective excitations of atomic nuclei in presence of pairing correlations.

[2] Actually, in order to minimize the numerical error in the differential equation resolution, it is usually adopted the suitable choice

$$\eta_k(t) = \langle\varphi_k(t)|h[\rho]|\varphi_k(t)\rangle\,. \tag{2.31}$$

Several extensions of the RPA theory described in section 1.3.2 have been introduced in the last decades to take into account pairing correlations, in complete analogy to the normal case. These Quasi-particle RPA (QRPA) approaches may therefore profitably encapsulate in only one coincise form, both *ph* and *pp* excitations of small amplitude, to provide a microscopic description of the low-lying collective states [89, 129]. In the small amplitude limit, in fact, the QRPA is completely equivalent to the TDHFB. For spherical nuclei, there are extensive studies with the QRPA to investigate excited states in stable and unstable nuclei [175] and the coupling with continuum states [102]. Furthermore, recently the QRPA calculations have become possible also for nuclei with axially deformed ground states, allowing to get a description of quadrupole, octupole and pairing vibrations for these systems [116]. However, these fully self-consistent QRPA calculations require yet a massive computational cost.

At the same time, the problem of extending the semi-classical Vlasov equation derived in section 1.5.2 to superfluid systems has been tackled many years ago by Di Toro and Kolomietz in the nuclear physics context [58] and, more recently, by Urban and Schuck [183] to study the dynamics of trapped systems made of atomic fermions. In these mesoscopic systems, the semi-classical approach simplifies the fully quantum calculation. Unfortunately, the application of this method to study the linear response of heavy nuclei has allowed so far to evaluate pairing effects in low-energy excitations only under quite drastic approximation [1]. Otherwise, the adoption of the semi-classical approach does not lead to a concrete simplification of the equations.

2.4 Pairing effective interaction

The formalism adopted in the HFB theory has provided an useful tool to investigate the nature of a paired many-body system in a very general case. Nevertheless, in the general context of the nuclear EDF theory discussed in Chapter 1, the HFB equations could be also obtained simply by minimizing the energy with respect to the normal and pairing density matrices for a fixed average number of neutrons and protons [60]. All one needs is the

specification of the pairing contribution $\mathcal{E}_{\rm pair}$ to the nuclear energy density functional presented in Eq. (1.37) and so it would be desirable to introduce, rather than the general interaction considered so far, a suitable pairing effective interaction which allows one to easily perform the calculations and, at the same time, to well describe the pairing properties of both finite nuclei and infinite nuclear matter.

The pairing effective interaction most commonly adopted in literature [43] is a spin-independent and contact range interaction[3], viz:

$$V_{\rm pair}(\mathbf{r}_1, \mathbf{r}_2) = \frac{1}{2}\left(1 - \hat{P}_\sigma\right) v_{\pi q}\left[\rho_n(\mathbf{r}), \rho_p(\mathbf{r})\right] \delta(\mathbf{r}_{12}) \qquad q = p, n, \tag{2.32}$$

where $v_{\pi q}$ is the so far unspecified strenght of the pairing interaction, while $\hat{P}_\sigma$ is the spin-exchange operator defined in section 1.4.1.

Although the microscopic analysis in semi-infinite nuclear matter suggests the presence of a surface component for the pairing in nuclei [10], the density dependence of the pairing interaction is still poorly known nowadays. Despite of it, in the next, the following density dependence of the strength is adopted [20]:

$$v_{\pi q}(\rho_n, \rho_p) \equiv v_\pi(\rho_q) = V_\pi^\Lambda \left[1 - \eta_\pi \left(\frac{2\rho_q}{\rho_0}\right)^{\alpha_\pi}\right], \tag{2.33}$$

where V_π^Λ, η_π and α_π are parameters one should properly choose.

It is quite interesting to underline that, while interactions with η_π equal to 0 or 1 correspond to the extreme cases where the pairing is considered uniquely a volume or a surface phenomenon, respectively, systematical studies in nuclei seem to prompt for a mixed nature of the pairing [59, 157]. Moreover, by considering a δ interaction as in Eq. (2.32), the orbital angular momentum is zero and so only the S-wave scattering is allowed.

[3]Because of the zero range of the interaction employed, a regularization procedure must be applied in order to avoid divergency problems [66].

2.4.1 Energy gap in pure neutron matter

Regardless of the parameterization of the pairing effective interaction one chooses, the interaction introduced in Eqs. (2.32) and (2.33) has however a phenomenological nature, with all its benefits and shortcomings. As mentioned in Chapter 1, though these forces have been widely applied in nuclear structure calculations, they have not any immediate connections with realistic nucleon-nucleon interactions and thus their reliability beyond the domain in which they are fitted is not fully guaranteed.

In order to establish a deeper relation with the real nucleon-nucleon interaction, in the framework of the infinite systems we are interested in, it has been recently proposed to determine the parameters of the pairing interaction by fitting the gap in nuclear matter as deduced from microscopic calculations that make use of a realistic force, in the BCS approximation [76] and in Brueckner-type calculations [39]. In the next sections, in particular, the calculations which are going to be considered are based on the realistic nucleon-nucleon interaction Argonne v_{14} [39]. Anyway, the calculations making use of the BCS theory with the single free particle spectrum give back similar results even employing different interactions [9, 57].

Unluckily, the evaluation of the gap is available only for matter with extreme values of the asymmetry I, that is for SNM ($I = 0$) or in the pure neutron matter ($I = 1$) case. Moreover, although in principle the pairing interaction can act between particles belonging to different nuclear species, it has been observed that in the $^1S_0$ pairing channel we are focusing on, which characterizes nucleons with zero angular momentum l and opposite spin projection, the neutron-proton pairing is strongly quenched as soon as the asymmetry I of the matter exceeds 0.1 [164]. Thus, even a small difference on the Fermi surfaces of the two species involved destroys the np pairing.

Since in our work we are mainly interested in the behavior of asymmetric nuclear matter, also in connection with the important astrophysical implications of superfluidity (see Chapters 3 and 4), it has been decided finally to extract the $^1S_0$ gap from the pure neutron matter case and therefore to consider the pairing only in nn or pp channel, by extrapolating to protons

the results obtained for the neutron-neutron pairing strength.

Moreover, one should mention that, because of the contact range of the interaction adopted in Eq. (2.32), the $^1S_0$ neutron gap Δ_n is momentum-independent and therefore, by considering its value at the Fermi momentum $p_n^F = \hbar k_n^F$, it turns to be only density dependent, greatly simplifying the resolution of the BCS gap equation Eq. (2.26).

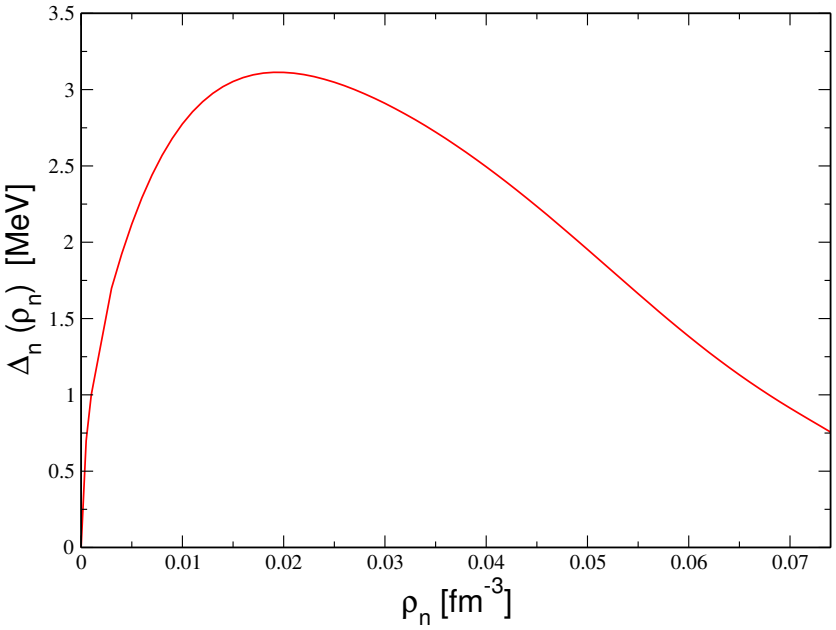

Figure 2.4: The $^1S_0$ neutron pairing energy gap Δ_n evaluated at the Fermi momentum p_n^F, as obtained in Brueckner calculations of pure neutron matter, as a function of the neutron density ρ_n.

Fig. 2.4 shows the (neutron) density dependence of the $^1S_0$ pairing gap, as given in [115]. In this figure, it clearly emerges that this kind of correlations in neutron matter are mostly active in the sub-saturation density region (below 0.1 fm^{-3}). Specifically, the $^1S_0$ pairing gap exhibits a rather extended peak, with a maximum around 3 MeV for very low density values ($\sim \rho_M = 0.02$ fm^{-3}), together with a smooth decrease at higher densities and a quite sharp vanishing when ρ approaches zero.

2.4.2 Determination of the strength: gap equations

Once the $^1S_0$ gap is fixed, the density dependence of the pairing strength Eq. (2.33) can be evaluated, for any value $\Delta(\rho_q)$, by inverting the Eq. (2.26), together with the equation for the conservation of the number of particles (Eq. (2.27)). Both equations, still in the zero temperature case, are re-written below in the thermodynamical limit as:

$$\begin{aligned} I_\Delta &\equiv -v_\pi(\rho_q) \int \frac{d\mathbf{p}}{(2\pi\hbar)^3} \frac{1}{2E_q^\Delta} = 1 \\ I_\rho &\equiv \int \frac{d\mathbf{p}}{(2\pi\hbar)^3} \left(1 - \frac{\xi_q}{E_q^\Delta}\right) = \rho_q, \end{aligned} \tag{2.34}$$

where $E_q^\Delta = \sqrt{\xi_q^2 + \Delta_q^2}$ is the single quasi-particle energy, ξ_q is given by

$$\xi_q = \frac{p^2}{2m_q^*} - \mu_q^*, \tag{2.35}$$

and having denoted with m_q^* the nucleon effective mass. The definition of this latter quantity, bearing in mind the analytical form of the energy density functional $\mathcal{E}$ given in Eq. (1.37), is expressed by this relation [147]:

$$\frac{m_q^*}{m} = \frac{\hbar^2}{2} \left(\frac{\partial \mathcal{E}}{\partial \tau_q}\right)^{-1}, \tag{2.36}$$

thus it differs from the bare nucleon mass m only in case of momentum-dependent interactions.

Let us highlight some general features of Eqs. (2.34). First of all it is important to underline that the effective masses introduce a connection between the values of the parameters of the pairing effective interaction and those of the Skyrme parameterization employed. On the other hand, parameterizations with the same effective mass are going to have the same values for the parameters in Eq. (2.33).[4] Another important remark regarding the effective masses is the coupling produced in the gap equations of the two

[4]It obviously implies that even all momentum independent interactions present the same values for V_π^Λ, η_π and α_π.

nucleonic species, whereas Eqs. (2.34) would be fully decoupled in case again of momentum independent interactions. Finally, let us stress that, in order to cure the divergency exhibited at high p-values by the gap equation, it has been decided to put a cut-off on the single particle kinetic energy so that $\epsilon_\Lambda = \frac{p_\Lambda^2}{2m_q^*} - \mu_q^*$ is equal to 16 MeV [43]. Such a regularization necessarily affects the value of the strength parameters, especially for V_π^Λ. At very low densities, in fact, both the pairing gap and the effective chemical potential vanish, so from the gap equation it is easy to demonstrate that:

$$V_\pi^\Lambda = \lim_{\rho_q \to 0} v_\pi(\rho_q) = -\frac{4\pi^2}{\sqrt{\epsilon_\Lambda}} \left(\frac{\hbar^2}{2m}\right)^{3/2}, \tag{2.37}$$

and so the parameter V_π^Λ comes out to be strongly dependent (only) on the energy cut-off ϵ_Λ introduced, under the constraint that $m_q^* \xrightarrow{\rho_q \to 0} m$. This relation between V_π^Λ and ϵ_Λ has to be taken into account when one fits the strenght of the pairing interaction.

2.4.3 Inclusion of the pairing in the nuclear EDF

The definition of the pairing effective interaction Eq. (2.32) allows one to associate to the nuclear EDF the following pairing energy density [44]:

$$\mathcal{E}_{\text{pair}} = \frac{1}{4} \sum_{q=n,p} v_\pi \left[\rho_q(\mathbf{r})\right] \tilde{\rho}_q^2(\mathbf{r}), \tag{2.38}$$

where the local pairing density $\tilde{\rho}$ is defined, in the coordinate space, as

$$\tilde{\rho}_q(\mathbf{r}s, \mathbf{r}'s') = -2s'\kappa_q(\mathbf{r}s, \mathbf{r}' - s'). \tag{2.39}$$

The local part of the latter, in particular, in the BCS approximation and by summing up over the spin values and taking into account the relation Eq. (2.11), can be written as

$$\tilde{\rho}_q(\mathbf{r}) = \sum_s \tilde{\rho}_q(\mathbf{r}s, \mathbf{r}s) = -\kappa^q_{\uparrow\downarrow}(\mathbf{r}) + \kappa^q_{\downarrow\uparrow}(\mathbf{r}) = 2\kappa^q_{\downarrow\uparrow}(\mathbf{r}) = 2\frac{\Delta_q}{v_\pi(\rho_q(\mathbf{r}))} \tag{2.40}$$

so that one can achieve the following relations:

$$U_q = \left(\frac{\partial \mathcal{E}}{\partial \rho_q}\right)_{\tilde{\rho}_q}, \qquad \Delta_q = \left(\frac{\partial \mathcal{E}}{\partial \tilde{\rho}_q}\right)_{\rho_q}. \tag{2.41}$$

It should be taken into account that, since the Eq. (2.38) depends on the normal nucleon densities, $\mathcal{E}_{\rm pair}$ also contributes to the mean-field potential U_q.

2.5 Impact of superfluidity on thermodynamical properties of ANM

In this section, making use of the pairing effective interaction introduced in Eqs. (2.32) and (2.33) and of its contribution to the EDF Eq. (2.38), we are going to show the effect of the pairing on some thermodynamical properties of ANM. For the sake of simplicity, we will consider a simplified version of the Skyrme energy density functional defined in Eqs. (1.37) and (1.38), in which the momentum dependent terms are neglected ($C_{eff} = D_{eff} = 0$) and the incompressibility modulus K (see Eq. (1.62)) equals 200 MeV [32]. As far as the symmetry energy is concerned, the parametrizations considered allow for two different types of density dependence, associated with two different parametrizations of the potential part of the symmetry energy coefficient, $C_{pot}(\rho)$ of Eq. (1.56). For the *asy-stiff* EoS, $C_{pot}(\rho) = 18\frac{\rho}{\rho_0}$ MeV, while the *asy-soft* case corresponds to a parametrization with $C_{pot}(\rho) = \frac{\rho}{2}(482 - 1638\rho)$ MeV, associated with a small value of the slope parameter L. In this framework, the curve describing the density behavior of the strength function v_π, as obtained for pure neutron matter, is shown in Fig. 2.5 while the corresponding values of the coefficients V_π^Λ, η_π and α_π are given in Table 2.1[5].

[5]The value of V_π^Λ listed in Table 2.1 is actually not consistent with the analytical formula given in Eq. (2.37), because the pairing interaction has been fixed in this case to reproduce the gap in the density range 0.003 fm$^{-3} \leq \rho_q \leq$ 0.075 fm^{-3}. In the following chapters, whereas the behavior at very-low density will be considered, we will take into account the prescription given in Eq. (2.37).

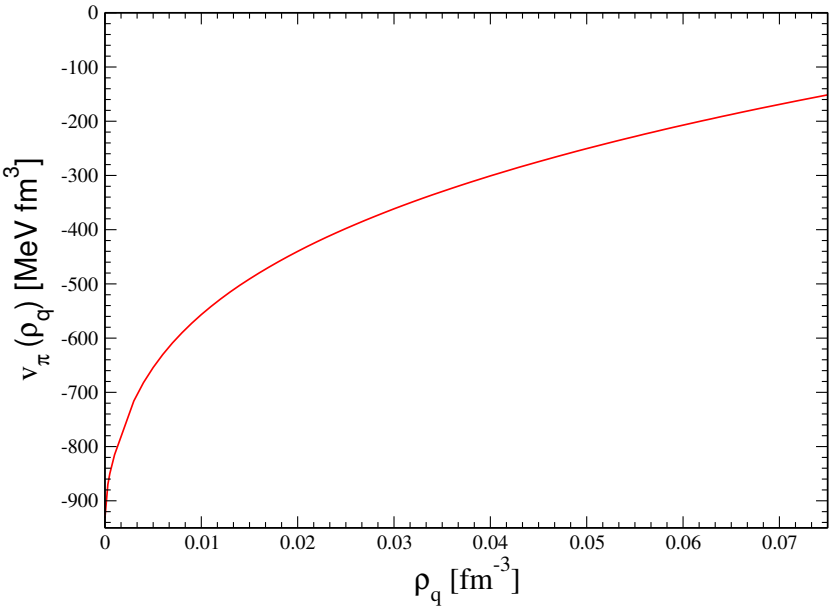

Figure 2.5: The neutron pairing strength v_π as a function of the neutron matter density ρ_n, as evaluated for momentum independent Skyrme interaction.

Table 2.1: The values of the parameters in the pairing effective interaction as achieved employing a simplified Skyrme interaction, without the momentum dependence.

V_π^Λ[MeV fm^3]	η_π	α_π
-1157.51	0.884	0.256

2.5.1 Influence on chemical potential and its derivatives

The solution of the gap equations allows one to evaluate not only the density dependence of the strength, but also the behavior with respect to ρ_q of the effective chemical potential μ_q^*. It may be useful to recall that, in absence of pairing, the latter quantity coincides with the Fermi energy ϵ_q^F of the nucleonic species q. Its modification caused by the coupling between particles is shown in Fig. 2.6.

The latter figure illustrates that the difference between the two functions is around 0.4 MeV at very low-density, but smoothly vanishes when increasing the density, until the two quantities converge. As one can expect, the repulsive pairing effect on μ_q^*, which can be connected to the Pauli blocking,

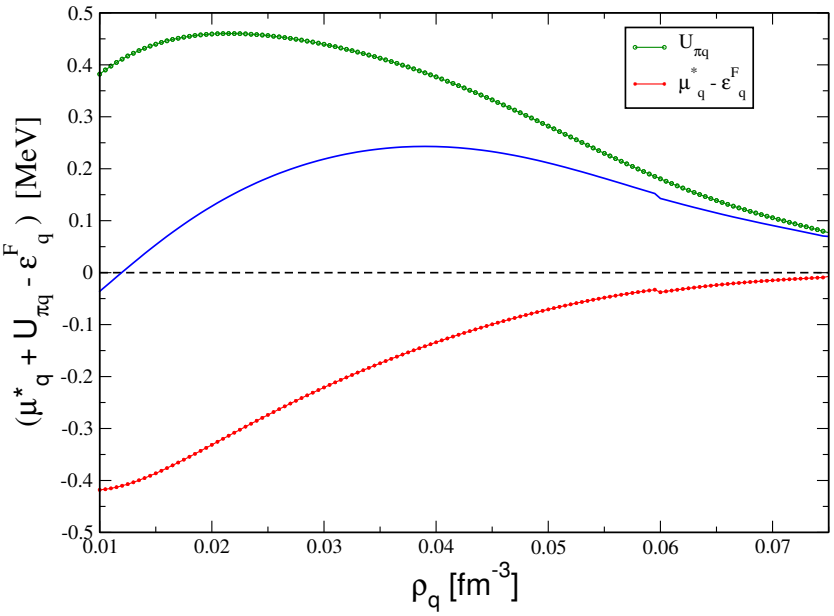

Figure 2.6: Difference between the chemical potentials, as evaluated for superfluid and normal matter respectively, as a function of the nucleonic density ρ_q (blue curve). The red curve represents also the difference between μ_q^* in superfluid matter and the corresponding Fermi energy ϵ_q^F for the normal case, as a function of the density ρ_q. The green curve shows the density behavior of the potential contribution of the pairing to the chemical potential.

depends on the ratio $\frac{\Delta_q}{\mu_q^*}$ and so it is more important on the one hand when the gap is close to its maximum, on the other hand when μ_q^* is smaller.

Actually, keeping in mind the relation Eq. (2.25) and by reminding that, because of the density dependence of the pairing strength, the mean-field potential U_q defined in Eq. (2.41) also gets the contribution $U_{\pi\, q}$ from the pairing energy density $\mathcal{E}_{\rm pair}$ [44], one easily deduces:

$$\mu_q = \mu_q^* + U_{{\rm Sky}\, q} + U_{\pi\, q}, \tag{2.42}$$

with

$$U_{\pi\, q} = \left(\frac{\partial \mathcal{E}_{\rm pair}}{\partial \rho_q}\right)_{\tilde{\rho}_q} = \frac{\partial v_\pi(\rho_q)}{\partial \rho_q}\left[\frac{\Delta_q}{v_\pi(\rho_q)}\right]^2, \tag{2.43}$$

where the latter term is the (attractive) potential contribution of the pairing to the chemical potential and it has been evaluated by using the definition

Eq. (2.40) of $\tilde{\rho}_q$. This quantity partially counterbalances the kinetic correction, but since the two contributions do not cancel each other, the global pairing effect on the chemical potential turns to be appreciable in a quite wide range of density values.

In Chapter 1, it also emerged the importance to study the chemical potential derivative with respect to the density, since this quantity is connected to the compressibility of the matter and, more generally, to its stability. The evaluation of the derivative of Eq. (2.42) requires the knowledge of the following derivatives: $\partial\mu_q^*/\partial\rho_q$ and $\partial\Delta_q/\partial\rho_q$ (the latter appears in the derivative of the potential $U_{\pi\,q}$), which can be obtained by solving the following set of equations, derived from the gap equations Eq. (2.34):

$$\begin{cases} \dfrac{\partial I_\Delta}{\partial\rho_q} + \dfrac{\partial I_\Delta}{\partial\mu_q^*}\dfrac{\partial\mu_q^*}{\partial\rho_q} + \dfrac{\partial I_\Delta}{\partial\Delta_q}\dfrac{\partial\Delta_q}{\partial\rho_q} = 0 \\ \dfrac{\partial I_\rho}{\partial\mu_q^*}\dfrac{\partial\mu_q^*}{\partial\rho_q} + \dfrac{\partial I_\rho}{\partial\Delta_q}\dfrac{\partial\Delta_q}{\partial\rho_q} = 1 \end{cases} \tag{2.44}$$

Actually, since the Skyrme term is not affected by the pairing, a deeper insight into the amplitude of the superfluidity effect on the chemical potential derivatives can be obtained by looking directly at the quantity

$$\delta_q = \frac{\partial\mu_q^*}{\partial\rho_q} + \frac{\partial U_{\pi\,q}}{\partial\rho_q}. \tag{2.45}$$

The latter is displayed in Fig. 2.7, as a function of the density ρ_q, together with the corresponding value of normal nuclear matter (which is the density derivative of the Fermi energy). The two curves exhibit a larger difference in two different ranges of density values, where moreover an opposite variation with respect to the normal matter case is shown. This particular behavior leads, as it will be seen in the following sections, to very interesting results and applications.

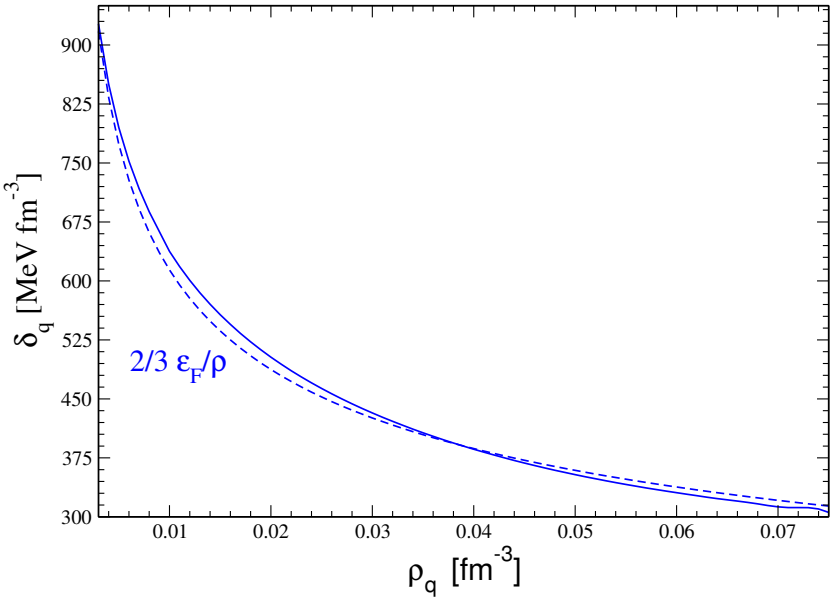

Figure 2.7: The quantity δ_q (see text) as a function of the density, in normal (dashed line) and superfluid (full line) matter.

2.5.2 Finite temperature: normal-superfluid phase transition

The impact of superfluidity on the properties of ANM has been so far investigated in the case of zero temperature. The introduction of the temperature T, as another degree of fredoom, makes the scenario depicted above more complicated. First of all, the mofication introduced by temperature on the particle occupation number determines the following change on the gap equations Eq. (2.34):

$$
\begin{aligned}
1 &= -v_\pi(\rho_q) \int \frac{d\mathbf{p}}{(2\pi\hbar)^3} \frac{1}{2E_q^\Delta} \tanh \frac{E_q^\Delta}{2T} \\
\rho_q &= \int \frac{d\mathbf{p}}{(2\pi\hbar)^3} \left(1 - \frac{\xi_q}{E_q^\Delta} \tanh \frac{E_q^\Delta}{2T} \right),
\end{aligned}
\tag{2.46}
$$

secondly, as a consequence, the energy gap Δ turns to be now temperature dependent. Since the solution of the Eq. (2.34) at zero temperature has fixed the pairing strength, by solving the gap equations Eq. (2.46), one can

evaluate the gap for any finite temperature T. The results are shown, for several T values, in Fig. 2.8. Looking at this figure, one notices how, for each

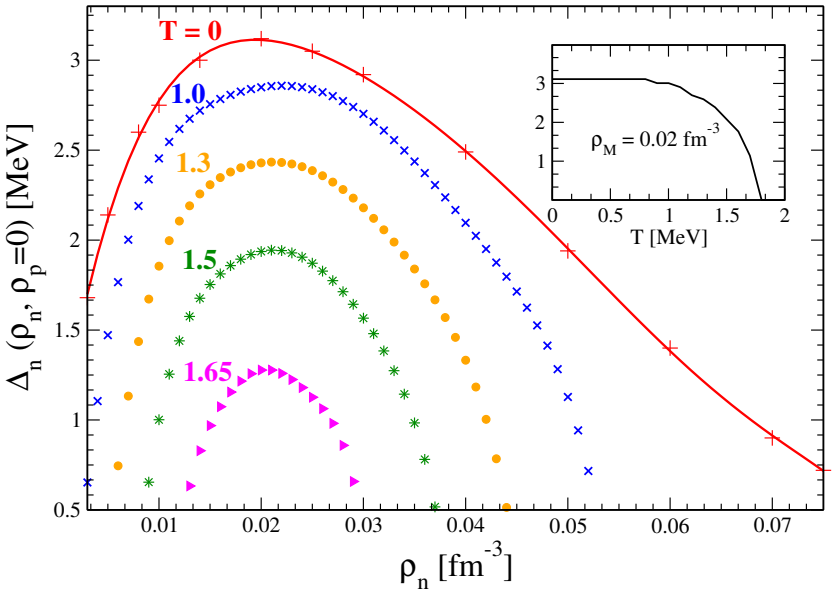

Figure 2.8: The energy $^1S_0$ pairing gap Δ_n, as a function of the neutron density ρ_n for several values of the temperature T. The inset show the same quantity, but as a function of the temperature and for the density $\rho_M = 0.02$ fm^{-3} which corresponds to the maximum of the gap.

ρ-value, it exists a temperature above which the gap disappears: this is the so-called critical temperature T_c for the superfluid-normal phase transition. The critical temperature naturally depends on the density and a reliable approximation for its value is given by the relation $T_c\ (\rho_q) = 0.57\Delta(\rho_q, T = 0)$ [71]. The inset of Fig. 2.8 displays that its maximum value, reached when $\rho = \rho_M$, is 1.8 MeV.

Similarly to what has been done in section 2.5.1 for the zero temperature case, let us move now to discuss the impact of the superfluidity on the chemical potential derivatives at finite temperature T. Looking at the Fig. 2.9, one can observe again the quantity δ_q defined in Eq. (2.45), now as a function of the temperature, for three fixed densities. Comparing the calculations including pairing correlations with the results of normal nuclear matter, as a rather interesting feature, it clearly leaps out the appearance of a discontinuity in the superfluid curve, in correspondence of the critical

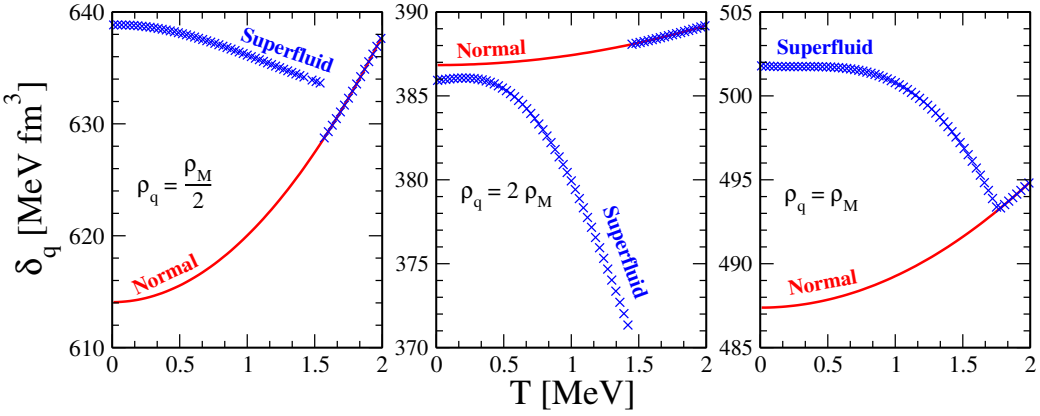

Figure 2.9: The quantity δ_q (see text) is represented as a function of the temperature T, for three nucleonic density values. Crosses indicate the calculations including pairing effects, whereas dashed lines are for normal nuclear matter.

temperature for the superfluid/normal phase transition.

Since the chemical potential derivatives involve the second derivative of the thermodynamical potential, this jump explicitly manifests the transition under investigation is a second order one. It is well known that at the critical temperature of a second order p.t. the heat capacity exhibits a discontinuity [72] (see Chapter 4), but here it is demonstrated that, together with this widely discussed effect, discontinuities also appear in the behavior of the density derivative of the chemical potential, which, we remind, is connected to the matter compressibility.

It is also rather interesting to observe that, according to the opposite trend with T exhibited by normal and superfluid calculations, the amplitude of the jump is higher when the curve obtained including pairing correlations lies below the normal one already at zero temperature (see Fig. 2.7). Moreover, owing to the features of the gap function illustrated in Fig. 2.8, the jump disappears at the density $\rho_q = \rho_M$, where the energy gap Δ_q is maximum and so its derivative vanishes at all temperatures.

2.6 Pairing effects on spinodal decomposition

As one can notice, there is an evident overlap between the region of the $^1S_0$ neutron superfluidity and the range of ρ values where nuclear matter manifests the liquid-vapor phase transition described in the first chapter. This coincidence reinforces the interest in introducing the pairing on the study of nuclear systems in low-density region and so it suggests to investigate how these correlations can affect not only the thermodynamical properties of nuclear matter, but also the characterization of the instability discussed in section 1.6.2.

2.6.1 Isospin distillation mechanism in normal matter

It has been already mentioned in section 1.6.2 that, in ANM at low density, instabilities correspond to isoscalar-like density oscillations, whereas the two species move in phase but with different amplitudes, according to the eigenvector components $(\delta\rho_p, \delta\rho_n)$.

In particular, denoting θ the angle in the space of proton-neutron density fluctuations so that $\tan\theta = \delta\rho_n/\delta\rho_p$, from the diagonalization of the curvature matrix given in Eq. (1.61) and re-written here for sake of simplicity as

$$\mathbf{C} = \begin{pmatrix} a & c/2 \\ c/2 & b \end{pmatrix}, \tag{2.47}$$

one obtains [13]:

$$\tan 2\theta = \frac{c}{a-b}. \tag{2.48}$$

In normal nuclear matter, it is generally found that the asymmetry of the density fluctuations, that is

$$\delta I = \frac{\delta\rho_n - \delta\rho_p}{\delta\rho_n + \delta\rho_p}, \tag{2.49}$$

is smaller than the system initial asymmetry I. As it has been anticipated in Chapter 1, this mechanism, named as isospin distillation, is mainly ruled by the effect of the symmetry potential, which enhances the neutron-proton at-

traction. Indeed, the symmetry energy tends to reduce the difference between proton and neutron chemical potential derivatives, i.e., the term $(a - b)$ in Eq. (2.48), so that neutrons and protons will oscillate with close amplitudes, in spite of the system initial asymmetry. This phenomenon experimentally leads to the formation of more symmetric nuclear clusters [113] and it is more effective especially in case of a stiffer parameterization of the symmetry energy behavior with respect to the density.

2.6.2 Role of the pairing on the isospin distillation

The aim of our recent work [32] has been to evaluate the impact of pairing correlations on the main features of the spinodal instability characterized above.

Actually, the strength of the instability, i.e., the amplitude of the negative eigenvalue λ_s of $\mathbf{C}$, is mainly determined by the isoscalar part of the nuclear mean field potential, which is by far the dominant term of the interaction. Thus the pairing interaction has practically no effect on it, at least far away from the spinodal border where it vanishes.

On the other hand, the distillation mechanism, which is connected to the strength of the symmetry potential, could be sensitive to the pairing interaction. Therefore, we focus on the interplay between the pairing force, coupling particles of the same type in a spin-singlet state, and the isovector interaction, which on the contrary enhances the attraction between particles of different kind.

Since the coefficient c, which is related to the mixed density derivative of the chemical potential, is not affected by pairing in the case of momentum independent interaction,[6] one relevant quantity to evaluate the amplitude of the pairing effect on the isospin distillation is the difference $\gamma = a - b$ of Eq. (2.48). In Fig. 2.10 we thus considered its percentage variation in superfluid nuclear matter, with respect to the normal matter case, as a function of the global density ρ, for different global asymmetries, in case of

[6] Actually, even for momentum dependent interactions, the influence of the pairing on the coefficient c is introduced only by the effective masses and is pratically negligible.

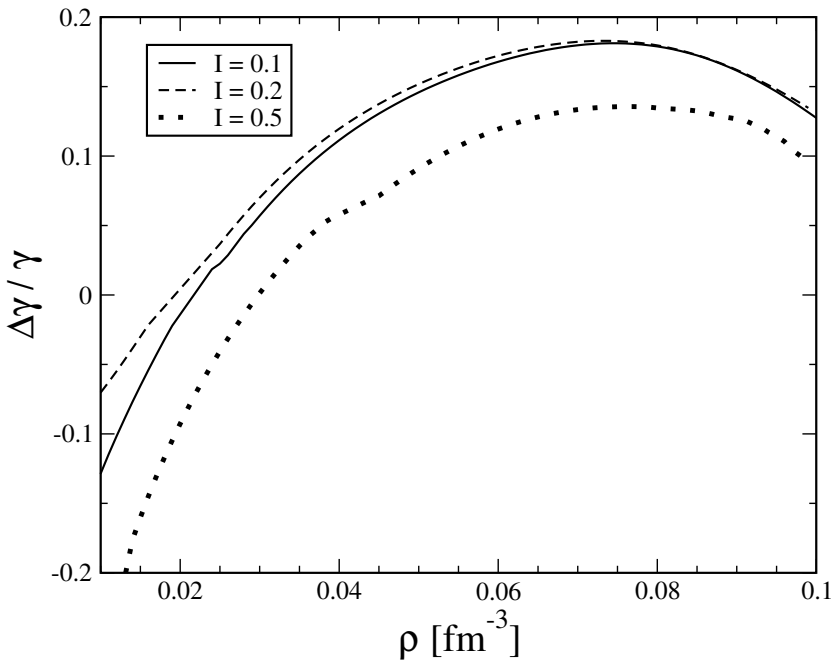

Figure 2.10: The percentage variation induced by the pairing on the quantity γ (see text) as a function of the total matter density ρ, at zero temperature, for three values of the asymmetry I and in case of an asy-stiff symmetry potential.

zero temperature and a stiff symmetry potential.

From the latter figure, it emerges that the physical conditions where pairing correlations have the largest impact on the isospin distillation are identified at total densities around 0.08 fm^{-3} and asymmetries $I \approx 0.1 \div 0.2$. These conditions corresponds to density of each nuclear species ρ_q which lies around the crossing (≈ 0.04 fm^{-3}) between the two curves of Fig. 2.7, so where the difference on the slope of the two trends is more important. In this thermodynamical (ρ, I) state, it is possible to reach hence an effect of 20% for the variation of γ at zero temperature.

This density region coincides also with the ρ_q values where the chemical potential derivatives manifest the largest amplitude of the discontinuity at finite temperature (see Fig. 2.9). Let us move therefore to discuss the impact of pairing correlations at finite temperature directly on the asymmetry δI of the unstable density oscillations. Results are displayed in Fig. 2.11, for nuclear matter again at $\rho = 0.08$ fm^{-3} and three values of the asymmetry I.

Moreover, two parametrizations of the symmetry energy are considered.

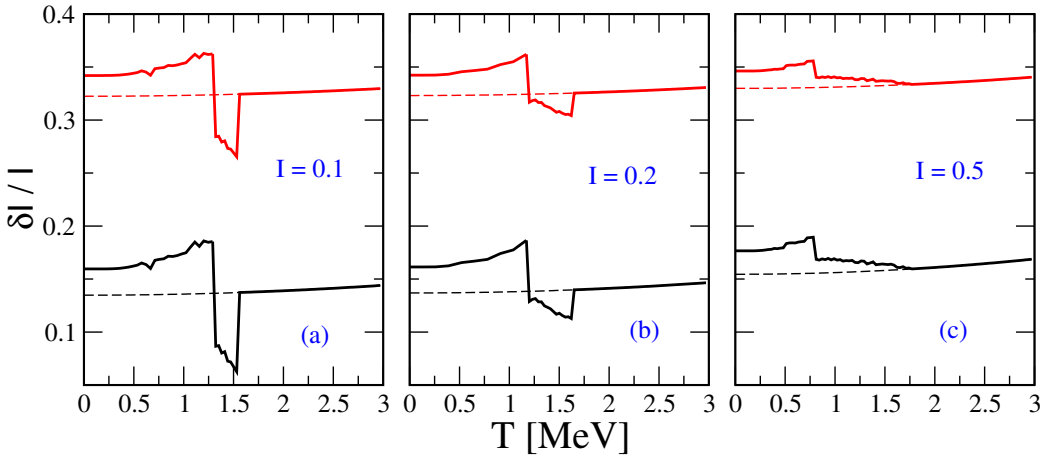

Figure 2.11: The asymmetry of the unstable oscillations δI is plotted as a function of the temperature, for nuclear matter at total density $\rho = 0.08$ fm^{-3} and three asymmetry values. Results are shown for both superfluid (full lines) and normal (dashed lines) matter and for asy-stiff (black) and asy-soft (red) parametrizations.

First of all one notices that the overall effect of the isospin distillation-mechanism is rather important. Indeed $\delta I/I$ is lower than 0.5 in all cases. The effect is larger in the asy-stiff case, which is characterized by a steeper variation of the symmetry energy with the density, in agreement with previous studies [51].

The asymmetry δI is moreover more sensitive to a variation on the symmetry energy parametrization (black vs. red lines) than to the introduction of pairing correlations (full vs. dashed lines). Thus these results essentially confirm the leading role of the symmetry energy in the isospin distillation mechanism.

Nevertheless, new interesting effects appear at a moderate increase of the temperature. Owing to the trend followed by the chemical potential derivatives, the calculations including the pairing interaction exhibit two discontinuities, in correspondence of neutron and proton critical temperatures, which may cause important variations of δI. As already stressed above, in Fig. 2.9 the discontinuity is more pronounced at neutron and proton densities ρ_q around $2\rho_M \approx 0.04$ fm^{-3}, so this explains why the largest effect for δI is seen, at the total density $\rho = 0.08$ fm^{-3}, at small asymmetries (panel (a)).

Hence, one can conclude that, under suitable density and temperature conditions, pairing correlations may lead to significant deviations of the asymmetry from its average. In particular, pairing correlations may have not negligible effects, especially around the transition temperature to the superfluid phase, on the isotopic features of the density fluctuations leading to cluster formation. These results might be relevant to the study of pairing correlations in low temperature nuclear fragmentation processes, as far as effects related to level density and isotopic composition of the primary fragments are concerned [53]. Moreover, as it will be discussed in Chapters 3 and 4, the presence of pairing correlations may also affect the description of low-density clustering phenomena occurring in compact stellar objects, such as in the crust of neutron stars.

Chapter 3

Cooling process in compact stars: neutrino emission

In this chapter, in parallel with the next one, we investigate the role of neutron superfluidity and proton superconductivity in the astrophysical setting of compact stars. We focus on the thermal evolution of these stellar objects, paying wide attention to the two main ingredients characterizing their cooling process: the neutrino emissivity and the specific heat. In this third chapter, in particular, we present a review of the modeling of neutron star and cooling mechanism, in order to bring out the reason why superfluidity is considered as a key feature in its understanding. Then we investigate the neutrino production and emission processes, and concentrating on the analysis of the neutrino interaction with a nuclear medium, we try to highlight the influence of the pairing correlations on the neutrino-baryon scattering cross section.

3.1 Essential physics of neutron stars

Since its discovery, neutron stars have been recognized as promising laboratories for studying nuclear matter under diverse conditions. As one deduces from the theoretician's view of a neutron star illustrated in Fig. 3.1, the study of these compact stellar objects involves a large variety of topics, character-

izing the research in modern nuclear physics.

3.1.1 Neutron star envelope and crust

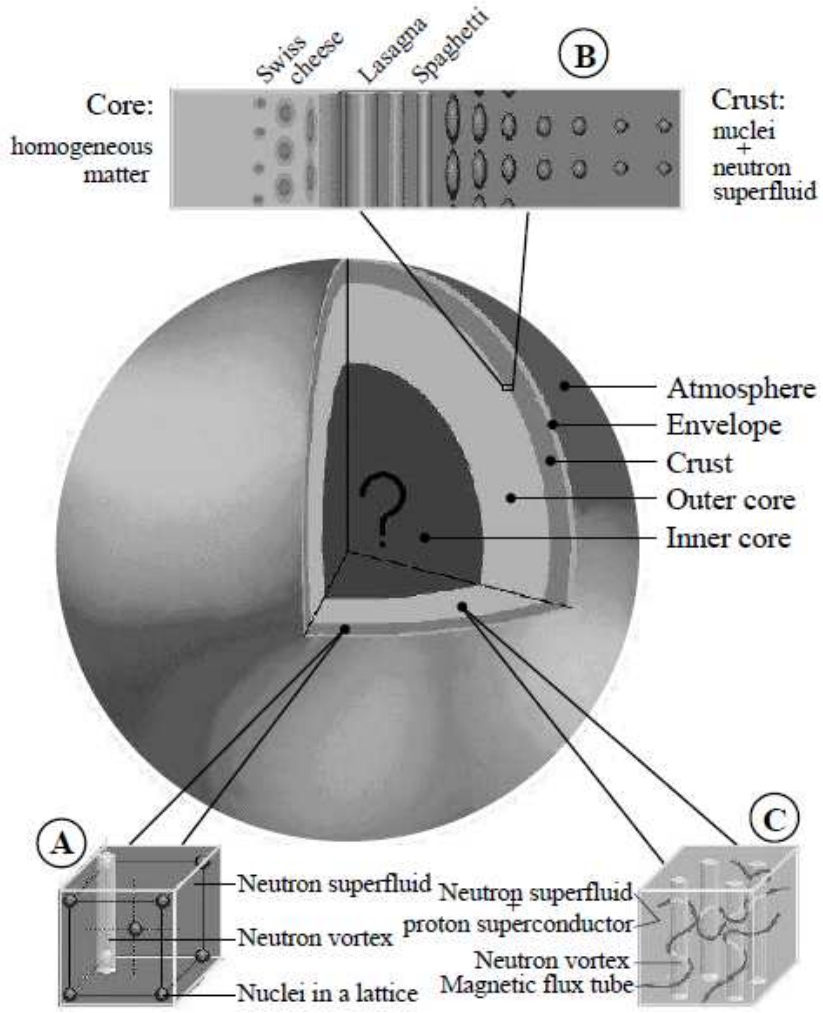

Figure 3.1: Structure of a neutron star.

A neutron star can be naively described as a giant and compressed nucleus, with a radius of $10 \div 20$ km. In the outer part of the star, above the surface, one expects the presence of an atmosphere, lying above a solid surface. A few meters below the surface, ions are completely pressure-ionized and matter consists of a solid lattice of nuclei in the Fe-Ni immersed in a quantum liquid of relativistic electrons. Here, and at higher densities, electrons

form an almost perfect Fermi gas. These low-density layers are commonly referred to as the envelope or the outer crust.

With growing ρ, lattice nuclei become progressively neutron-rich and one achieves the neutron drip point at which the neutron density is so large that some neutrons become unbound. Matter then consists of a crystal of nuclei immersed in a Fermi gas of electrons and a quantum liquid of dripped neutrons. This region is usually called inner crust and, in most part of it, the dripped neutrons are predicted to be superfluid. Furthermore, in the whole crust which has a thickness of $\lesssim 1$ km, if the matter was constitued only by an homogeneous liquid of nucleons, the system would be located inside the spinodal region, being mechanically unstable (see Chapter 1). Stability is, however, restored by the formation of nuclei, or nuclear clusters [133]. Moreover, the composition of the crust and the characteristics of the crust-core phase transitions depend very strongly on the symmetry energy. As a consequence, these objects are considered as a laboratory for testing the EoS.

As $\rho \sim 0.3\rho_0$, the shapes of nuclei can undergo drastic changes: from spherical shapes nuclei are expected to deform, becoming elongated into 2D or 1D structures named pasta phases, still surrounded by the superfluid neutron gas which occupies an increasing portion of the volume. The homogeneous phase is finally reached in the core of the star, when $\rho \gtrsim 0.5\rho_0$.

3.1.2 Neutrinos in neutron star interior

A "pure neutron star" as originally conceived by Oppenheimer and Volkoff [128], cannot really exist. Neutrons in a ball should β-decay into protons through

$$n \to p + e^- + \bar{\nu}_e. \tag{3.1}$$

Therefore, starting with a ball of nearly degenerate neutrons, the β-decay (3.1) will briefly create a degenerate sea of protons, electrons and anti-neutrinos. The inverse reaction

$$p + e^- \to n + \nu_e. \tag{3.2}$$

also occurs since not all particles are in their lowest energy states at all times.

The mean free paths of anti-neutrinos (and neutrinos) exceed by far the size of the star. In a neutron star, these can be assumed to immediately vacate the star, implying $\mu_\nu = 0$. Thus, these reactions will ultimately result in the neutrino-less β-equilibrium condition

$$\mu_n = \mu_p + \mu_e. \tag{3.3}$$

A neutron star, however, is not born from the collapse of a "ball of neutrons", but rather from the collapse of the iron core of a massive star. During the collapse, the reaction Eq. (3.2) therefore initially dominates over Eq. (3.1) in order to reduce the proton fraction. As the density increases, moreover, the neutrino mean free paths become smaller than the collapsing core's size, so the neutrinos ν_e are temporarily trapped within the core. In this case $\mu_\nu > 0$, altering β-equilibrium and permitting to the proton fraction to remain relatively large. Only after neutrinos are able to diffuse away, the final β-equilibrium condition Eq. (3.3) can be achieved.

3.1.3 Superfluidity in stellar matter

Soon after the introduction of the BCS theory, Migdal proposed to extend the idea of Cooper pair of fermions to the astrophysical context and specifically to the interior of neutron stars [121]. Since it has been introduced in the study of compact stellar objects, a huge amount of works has been dedicated to stellar superfluidity and various types of pairing of nucleons, hyperons or quarks have been considered.

The onset of nucleon pairing is expected to take place in some parts of a neutron star's interior within minutes to thousands of years after its birth and, as we will see, leads to the alteration of several important properties of matter. As a two-particle correlation, the Cooper pair can appear in many spin-orbital angular momentum states, as already stressed before. In a neutron star, in particular, one expects that nucleons could pair in a spin singlet state, $^1S_0$, at low densities, whereas a spin-triplet $^3P_2$ pairing should occur at high densities. The gap in the $^1S_0$ pairing channel, as deduced in

Chapter 2 in the case of homogeneous nuclear matter, is mainly active for the dripped neutrons in the inner crust. However, one should consider that the presence of nuclear clusters, especially in the pasta phase region, may modify the uniform matter value.

Although pairing does not affect significantly the pressure-density relation and, therefore, the overall structure of neutron stars, the specific heat of dense matter and the emissivity of neutrinos are dramatically influenced up to the pairing critical temperature [133].

Superfluidity can also be important in dynamical phenomena concerning neutron stars. It has long been suspected, for example, that the so-called glitch phenomenon observed in pulsars is due to the existence of superfluids within the neutron star crust and perhaps the outer core.

In this thesis, we are focusing on the important consequences that superfluidity implies mainly for the thermal evolution of neutron stars.

3.2 Thermal evolution of a compact star

The challenging study of neutron star cooling is tackled following the temporal evolution of the stellar energy balance. At its birth, a huge amount of gravitational energy is converted into thermal energy: almost its totality is emitted in neutrinos during the first minutes, the proto-neutron star phase, while the remaining part is transferred to the supernova eject or is left as thermal energy in the new-born neutron star.

Most thermal evolution calculations involve the heat transport and energy balance equations, in their fully general-relativistic form [132]. However the main features can be illustrated, in a simplified way, under the hypothesis that the star's interior is isothermal, by the global energy-balance as [133]:

$$\frac{dE_{\rm th}}{dt} = C_V \frac{dT}{dt} = -L_\nu - L_\gamma + Q_{diss} \tag{3.4}$$

where $E_{\rm th}$ is the star total thermal energy, C_V its heat capacity, L_ν and L_γ its neutrino and photon luminosity, respectively, while Q_{diss} denotes the contribution given by some other heating dissipative processes, which will

be neglected hereafter. Within the isothermal approximation, which is a resonable state in a core-collapse supernova few decades after its birth, the three major ingredients of this study are therefore C_V, L_ν and L_γ.

The surface photon luminosity is essentially described by the Stefan-Boltzmann equation, by introducing instead of T a much lower effective temperature, which essentially depends on the gradient existing, even in the isothermal interior case, with the outermost layers [133]. The heat capacity and neutrino emission require instead a more detailed discussion since, as we already mentioned, they are strongly affected by the pairing correlations.

3.2.1 Heat capacity and pairing correlations

The stellar matter is constituted by leptons, baryons, mesons, and, possibly, deconfined quarks at the highest densities. Since the heat capacity at constant volume C_V is an extensive quantity, one has:

$$C_V = \sum_i C_{V,i} \qquad \text{with} \qquad C_{V,i} = \int c_{V,i}\, dV \tag{3.5}$$

where $c_{V,i}$ is the specific heat of the constituent i ($i = e$, μ, n, p, nuclei, hyperons, quarks). In the theory of quantum fluids, for a normal (i.e., unpaired) degenerate fermion system at low temperature, one naturally has $c_{V,i} \propto T$, but since most part of these components are superfluid, the pairing significantly reduces C_V. However this reduction is no more than a factor of the order of ten because leptons do not pair in any case.

Regarding the crust thermalization time, it is known that the cooling time is essentially determined by the inner-crust matter. The crustal specific heat should be, in principle, dominated by the unbound neutrons in the inner crust but, as these are certainly extensively paired, also the contribution of electrons and nuclear cluster lattice can be relevant.

In Chapter 4, we propose a stellar matter model which includes pairing correlations and clusters as degrees of freedom, in order to accurately evaluate the heat capacity of the inner crust.

3.2.2 Neutrino emission processes

The thermal evolution of neutron stars with ages $\lesssim 10^5$ yrs is driven by neutrino emission. The main neutrino production processes involving nucleons are listed and classified in table 3.1.

Table 3.1: A sample of neutrino emission processes involving nucleons [131].

Name	Process	Efficiency
Direct Urca	$\begin{cases} n \to p + e^- + \bar{\nu}_e \\ p + e^- \to n + \nu_e \end{cases}$	Fast
Cooper pair	$\begin{cases} n + n' \to [nn'] + \nu + \bar{\nu} \\ p + p' \to [pp'] + \nu + \bar{\nu} \end{cases}$	Medium
Brehmsstrahlung	$\begin{cases} n + n' \to n + n' + \nu + \bar{\nu} \\ n + p \to n + p + \nu + \bar{\nu} \\ p + p' \to p + p' + \nu + \bar{\nu} \end{cases}$	Slow
Modified Urca (neutron branch)	$\begin{cases} n + n' \to p + n' + e^- + \bar{\nu}_e \\ p + n' + e^- \to n + n' + \nu_e \end{cases}$	Slow
Modified Urca (proton branch)	$\begin{cases} n + p' \to p + p' + e^- + \bar{\nu}_e \\ p + p' + e^- \to n + p' + \nu_e \end{cases}$	Slow

The simplest neutrino emitting processes in the table are given by Eqs. (3.1) and (3.2), which collectively are generally referred to as the nucleon Direct Urca (DU) cycle. The conditions for the DU process are likely reached at some supra-nuclear density [131], but they strongly depend on the density behavior of the symmetry energy. At densities below the threshold, where the DU process is forbidden at low temperatures, a variant of this process, the Modified Urca (MU) process can operate. As it involves the participation of five degenerate particles, the MU process is much less efficient than the DU process. Unlike the nucleon DU process, both branches of the MU process operate at any density when neutrons and protons are present. The class of brehmsstrahlung processes differs from the MU cycle in that each reaction results in the production of a pair $\nu\bar{\nu}$ having any neutrino flavor. Bremsstrahlung reactions are less efficient than the MU processes, but may

make important contributions in the case that the MU process is suppressed by pairing of neutrons or protons. Bremsstrahlung involving electron-ion scattering is also an important source of neutrino emission in the neutron star crust:

$$e^- + (A, Z) \to e^- + (A, Z) + \nu + \bar{\nu} \tag{3.6}$$

where (A, Z) designates the participating ion.

The formation of the fermonic pair condensate also triggers a new neutrino emission process [165] which has been denominated Pair Breaking and Formation (PBF) process. Whenever any two fermions form a Cooper pair, the binding energy can be emitted as a ν-$\bar{\nu}$ pair. Under the right conditions, this PBF process can be the dominant cooling agent in the evolution of a neutron star [133]. Such efficiency is due to the fact that during the cooling of the star, the pairing phase transition starts when the temperature T reaches T_c and the pairs begin to form, but thermal agitation will constantly induce the breaking of pairs with subsequent re-formation and possible neutrino pair emission.

3.3 Neutrino interaction with a nuclear medium

Regardless the mechanism responsible for its production, neutrino interactions in a neutron-rich nuclear medium play a crucial role in core-collapse supernovae [96] and in the early thermal relaxation phase of newly formed neutron star [119]. The neutrino flux is moreover the only direct probe of the mechanism of supernovae and the structure of proto-neutron stars [11, 21, 35, 100, 145].

Recently, many efforts have been devoted in describing neutrino production and interactions in great detail [95, 119, 134, 192]. In such a context, the most important ingredient in transport calculations is the neutrino opacity, essentially determined by charged current absorption and neutral current scattering reactions. In the next sections we are going to investigate in particular the latter mechanism, hence focusing on the (elastic) neutrino scattering process on an homogeneous nuclear medium, owing to its strong

connection with the characterization of the unstable region exhibited by the nuclear mean-field and pointed out in the previous chapters. At the onset of spinodal instabilities, in fact, it is emerged that, according to the global isoscalar-like character of the instability, the density response function is enhanced, thus modifying the neutral current neutrino opacity [118]. The assumption of homogeneous matter implies anyway some drawbacks which will be underlined in the following.

3.3.1 Neutral current neutrino scattering

Let us consider nonrelativistic nucleons coupled to neutrinos through only the vector neutral current, neglecting contributions from the axial current. The weak-interaction Lagrangian density is

$$\mathscr{L}_W = \frac{G_F}{\sqrt{2}} \bar{\psi}_\nu(x) \left(1 - \gamma_5\right) \gamma_0 \psi_\nu(x) J_0^{(N)}(x), \tag{3.7}$$

where G_F is the weak coupling costant, $\psi_\nu(x)$ the neutrino field operator, γ_0 and γ_5 the Dirac matrices, as in their standard notation, and

$$J_0^{(N)}(x) = \sum_{i=n,p} c_V^{(i)} \rho_i(x), \tag{3.8}$$

with $c_V^{(n)} = -0.5$ and $c_V^{(p)} = 0.036$, is the nucleon density operator.

Then the differential cross section (per unit of volume V) for scattering in a nuclear medium of neutrinos with energy E_ν, as a function of the neutrino final energy E'_ν and scattering angle θ, is given by [36, 99]:

$$\frac{1}{V} \frac{d^3\sigma}{dE'_\nu d\Omega^2} = \frac{G_F^2}{8\pi^3} (E'_\nu)^2 (1 + \cos\theta) S_V^{00}(\omega, \mathbf{q}), \tag{3.9}$$

where[1] $\omega = E_\nu - E'_\nu$ denotes the energy transfer to the medium, $\mathbf{q}$ is the momentum transfer and S_V^{00} identifies the dynamic form factor, which can

[1] We use the natural units: $\hbar = c = k_B = 1$.

be expressed in terms of the nucleon density-density correlation factor as:

$$S_V^{00}(\omega, \mathbf{q}) = \int dt\, d\mathbf{r}\, e^{i\omega t}\, e^{-i\mathbf{q}\cdot\mathbf{r}} \langle J^{(N)0}(t, \mathbf{r}) J^{(N)0}(0, 0)\rangle. \tag{3.10}$$

The momentum transfer $\mathbf{q}$ is related to ω and to the neutrino scattering angle θ as:

$$q = \left[E_\nu^2 + (E_\nu - \omega)^2 - 2E_\nu\,(E_\nu - \omega)\cos\theta\right]^{1/2}. \tag{3.11}$$

Considering the heavy nucleon mass, when we integrate the differential cross section over a range of ω values, the other factors in the integrand can be evaluated at $\omega = 0$, so that:

$$S_V^{00}(\omega, \mathbf{q}) \to \delta(\omega) \int d\omega' S_V^{00}(\omega', \mathbf{q}) = 2\pi\delta(\omega) S_V^{00}(\mathbf{q}), \tag{3.12}$$

where $S_V^{00}(\mathbf{q})$ is the static structure factor, which, according to Eq. (3.10), corresponds to $n-n$, $p-p$ and $n-p$ density fluctuation correlations taken at equal time:

$$S_V^{00}(\mathbf{q}) = \langle \delta J^{(N)\,0}(\mathbf{q}) \delta J^{(N)\,0}(-\mathbf{q})\rangle. \tag{3.13}$$

Exploiting the fluctuation-dissipation theorem [109] and neglecting quantum fluctuations, the static structure factor can be expressed, for a system at temperature T, as:

$$S_V^{00}(\mathbf{q}) = T\ \left[{c_V^{(n)}}^2 \mathbf{C}_{nn}^{-1}(q) + {c_V^{(p)}}^2 \mathbf{C}_{pp}^{-1}(q) + 2c_V^{(n)} c_V^{(p)} \mathbf{C}_{np}^{-1}(q)\right], \tag{3.14}$$

where the matrix $\mathbf{C}^{-1}$ is the inverse of curvature matrix of the system free energy density [36].

It has been evidenced that the static structure factor, and so the neutrino interaction, is clearly affected by general phenomena, such as phase transitions manifesting in interacting many-body systems. It emerged, in particular, that large density fluctuations, associated with the first order nuclear liquid-gas phase transition, could hugely increase the scattering of neutrinos [118], thus quenching their emissivity processes in low density regions.

3.3.2 Free-energy density matrix in stellar matter

Homogenous stellar matter can be considered as a nuclear medium where the proton charge is globally neutralized by a Fermi gas of electrons. A way to address such a system is to study its stability against finite-size density fluctuations [64]. The local energy density, which is a function of the total density $\rho = \rho_n + \rho_p$, the proton fraction $y_p = \rho_p/\rho$ and the electron density ρ_e, can be written as:

$$\mathcal{E}_{tot}(\rho, y_p, \rho_e) = \mathcal{E}_{HM} + \mathcal{E}^f_{HM} + \mathcal{E}_{Coul} + \mathcal{E}_e(\rho_e), \tag{3.15}$$

where $\mathcal{E}_e$ is the energy density associated with the electron kinetic energy and the contributions of the Coulomb term, $\mathcal{E}_{Coul}$, related to the interaction between all charges (protons and electrons), and of nuclear matter surface terms, $\mathcal{E}^f_{HM}$, are explicitly evidenced.

The electron term is readily evaluated in the approximation of a degenerate, ultrarelativistic Fermi gas. The spin-saturated homogeneous nuclear matter energy density, $\mathcal{E}_{HM}$, at finite temperature T and in the BCS approximation, as determined in Chapter 2, reads:

$$\mathcal{E}_{HM}(\rho, y_p) = \sum_{i=n,p} \left[2 \int \frac{d\mathbf{p}}{(2\pi)^3} f_i \frac{p^2}{2m_i^*} + \frac{1}{4} v_\pi(\rho_i) |\tilde{\rho}_i|^2 \right] + \mathcal{E}_{Sky}, \tag{3.16}$$

where the occupation number for a nucleon of species i with momentum $\mathbf{p}$, according to Eqs. (2.22) and (2.46), is:

$$f_i(\mathbf{p}) = \frac{1}{2} \left(1 - \frac{\xi_i}{E_i^\Delta} \tanh \frac{E_i^\Delta}{2T} \right), \tag{3.17}$$

while the other quantities have been already defined in Chapter 2.

Within this framework, one can then determine the derivatives of μ_i with respect to ρ_i and so evaluate the curvature matrix [64], which is needed in

the calculation of the cross section:

$$\mathbf{C}(q) = \begin{pmatrix} \partial_{\rho_n}\mu_n & \partial_{\rho_p}\mu_n & 0 \\ \partial_{\rho_n}\mu_p & \partial_{\rho_p}\mu_p & 0 \\ 0 & 0 & \partial_{\rho_e}\mu_e \end{pmatrix} + 2q^2 \begin{pmatrix} C^f_{nn} & C^f_{np} & 0 \\ C^f_{pn} & C^f_{pp} & 0 \\ 0 & 0 & 0 \end{pmatrix} + \frac{4\pi e^2}{q^2} \begin{pmatrix} 0 & 0 & 0 \\ 0 & 1 & -1 \\ 0 & -1 & 1 \end{pmatrix}, \tag{3.18}$$

where $e^2 = 1.44$ (MeV·fm) and the coefficients C^f_{ij} are combinations of the Skyrme surface parameters [64].

3.4 Pairing effect on ν-transport in star matter

In Chapter 2, we have stressed that, since pairing correlations are mostly active at low density and relatively low temperature, in a certain region of the nuclear matter phase diagram volume instabilities may co-exist with strong pairing effects. Pairing interaction modifies in fact neutron and proton chemical potentials and their derivatives, which appear in the curvature matrix in Eq. (3.18), and thus in suitable conditions of density, asymmetry and temperature, we can expect a non–negligible impact on the neutrino differential cross section [33].

As stressed before, neutrino trapping is quite influenced by large density fluctuations of the nuclear density, which develop close to the spinodal border and may lead to clustering phenomena. Within the approach adopted here, the amplitude of neutron and proton density fluctuations is essentially related to the inverse of the eigenvalues of the curvature matrix and in particular becomes quite large when the isoscalar-like one, $\lambda_S(q)$, is small. In this case, we expect pairing correlations to have a large relative weight on the curvature matrix elements, especially close to the critical temperature, T_c, for the transition from normal to superfluid matter, where discontinuities appear in the chemical potential derivatives (see section 2.5.2).

3.4.1 Spinodal border and superfluid phase transition

In order to bring out possible pairing effects, we investigate stellar matter at moderate temperature (below 2 MeV), at density and asymmetry conditions

close to the spinodal border, where λ_S vanishes. In the following numerical applications, we make use of the SAMi-J35 parametrization [151] of the Skyrme energy functional for the local energy density $\mathcal{E}_{sky}$ and the effective nucleon mass m_i^*. For the pairing term, the parameters of the effective interaction introduced in Eq. (2.33) are correspondingly deduced. For the sake of simplicity, moreover, we consider only neutron pairing, since as it is shown in the following, the latter leads in any case to the largest effects.

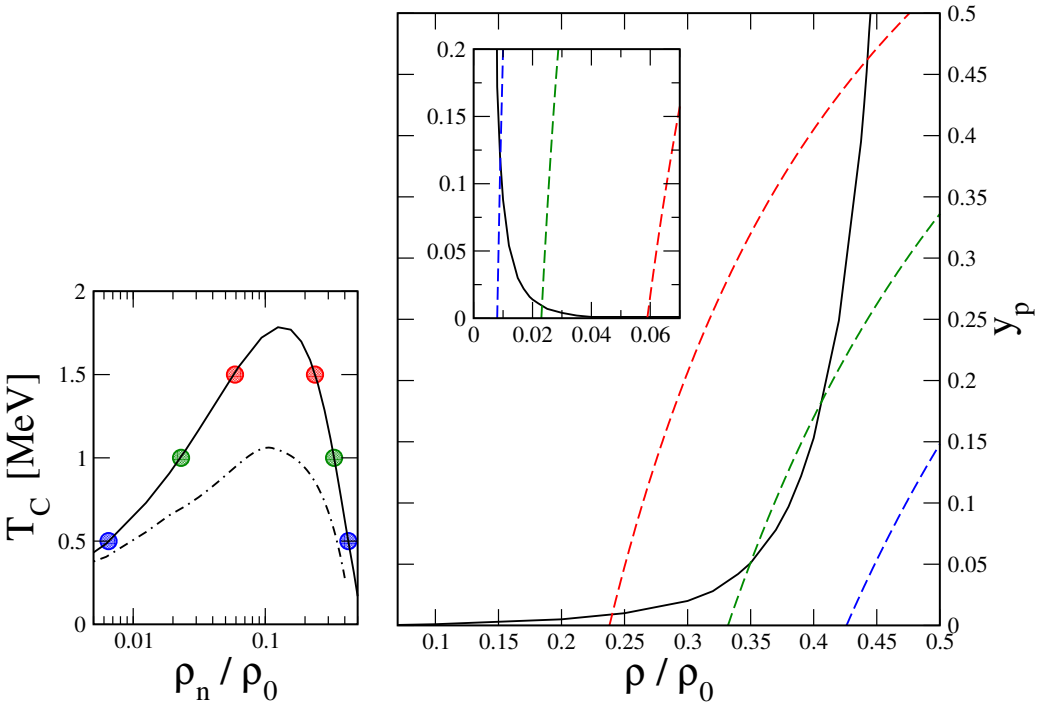

Figure 3.2: Left panel: critical temperature for the transition from superfluid to normal matter, as a function of the reduced neutron density ρ_n/ρ_0, as obtained in the strong pairing (full line) and weak pairing (dot-dashed line) cases. Right panel: spinodal border (full line), in the (ρ, y_p) plane, associated with temperature T = 0.5 MeV and momentum transfer q = 30 MeV. The inset shows a zoom in the low-density region. The dashed lines are curves of constant neutron density, corresponding to the values associated with the circles in the left panel (see text for more details).

In Fig. 3.2 (left panel) we represent the critical temperature T_c as a function of the neutron density. Since the magnitude of the gap in neutron matter is not clear yet, we considered, together with the case of the bare nucleon-

nucleon interaction (already introduced in Chapter 2 and denoted as strong pairing hereafter), another possible scenario for the pairing, obtained by taking into account in-medium effects on two-body interaction and self-energy, which lead to a considerable reduction of the pairing gap (denoted as weak pairing) [39]. The parameters of the pairing effective interaction, as determined for SAMi-J35 parameterization are listed in Table 3.2, for both strong and weak pairing cases.[2]

Table 3.2: The parameters of the pairing effective interaction as achieved employing SAMi-J Skyrme parameterizations.

	V_π^Λ[MeV fm^3]	η_π	α_π
Strong	-931.83	0.830	0.366
Weak	-931.83	0.842	0.265

The right panel shows the spinodal border (full line), in the (ρ, y_p) plane, at temperature and q values of interest for our study. It should be noticed that, because of Coulomb and surface effects, the spinodal border depends on q, but it is not very sensitive to the temperature, within the range considered in our study. For a fixed value of the temperature T, the plot on the left panel allows one to identify two values of the neutron density ρ_n (see the circles) for which the temperature considered corresponds to the critical one, so pairing effects could be large. Each value of the neutron density defines an hyperbole in the (ρ, y_p) plane (see the dashed lines on the right panel). Then the crossing of the dashed lines with the spinodal border identifies the density-asymmetry regions where large density fluctuations can coexist with important pairing contributions. It appears that a variety of conditions, from very small densities up to $\rho \approx 0.4\rho_0$ and with proton fraction ranging from quite low values up to $y_p \approx 0.5$, are good candidates for our study. These conditions may occur in the inner crust of a neutron star or in the pre-bounce phase of a supernova explosion, when the temperature is still low (see e.g. refs. [34, 37, 120, 145]).

However, since our pairing interaction has been fitted to reproduce the gap in neutron matter, we concentrate our analysis mainly to thermodynam-

[2]Actually, the same values hold also for the other SAMi-J parameterizations presented in Table 1.1, since they have the same effective mass.

ical conditions involving a rather small value of the proton fraction. If one wants to apply our study to the supernova matter in the pre-bounce phase, whereas the proton fraction is known to be large ($y_p \sim 0.3$) [146], then it would be better to extrapolate the results obtained trying to reproduce the pairing gap also for symmetric matter. Moreover, as it will be underlined in the next chapter, the clusterization of the stellar matter can significantly affect the thermodynamical conditions of these systems. The latter issue will be discussed in the last part of this chapter.

3.4.2 Impact on neutrino-nucleon cross section

Guided by the previous analysis, in the following we discuss the results obtained for the two opposite density regimes:

(1) $\rho = \rho_0/100$;

(2) $\rho = \rho_0/4$.

Several y_p values will be tested, close to the points suggested by Fig. 3.2.

Dependence on neutrino energy and scattering angle. To stress the impact of superfluidity, in the two opposite density regimes considered above, we focus on temperatures where we expect large pairing effects, that is $T = 0.5$ MeV in case (1) and $T = 1.4$ MeV in case (2). For the conditions considered now, only neutrons are paired, because the temperature values are always above the proton critical temperatures. Fig. 3.3 (left panel) illustrates the neutrino differential cross section

$$\sigma_{VE} \equiv \frac{1}{V E_\nu^2} \frac{d^2\sigma}{d\Omega^2}, \tag{3.19}$$

as a function of the neutrino energy E_ν and at a scattering θ angle such that $q = E_\nu$. To stress pairing effects, the results related to the complete calculation (full lines) are shown together with those obtained by neglecting the pairing interaction (dashed lines).

One can observe that, due to Coulomb repulsion, at small momentum transfer q values, the eigenvalue $\lambda_S(q)$ is always positive and so the density oscillations are stable. Actually, at the lowest density considered (case (1), panel (a)), the proton fraction $y_p = 0.045$ corresponds to stable conditions for all q values. Within such a thermoynamical configuration, the density os-

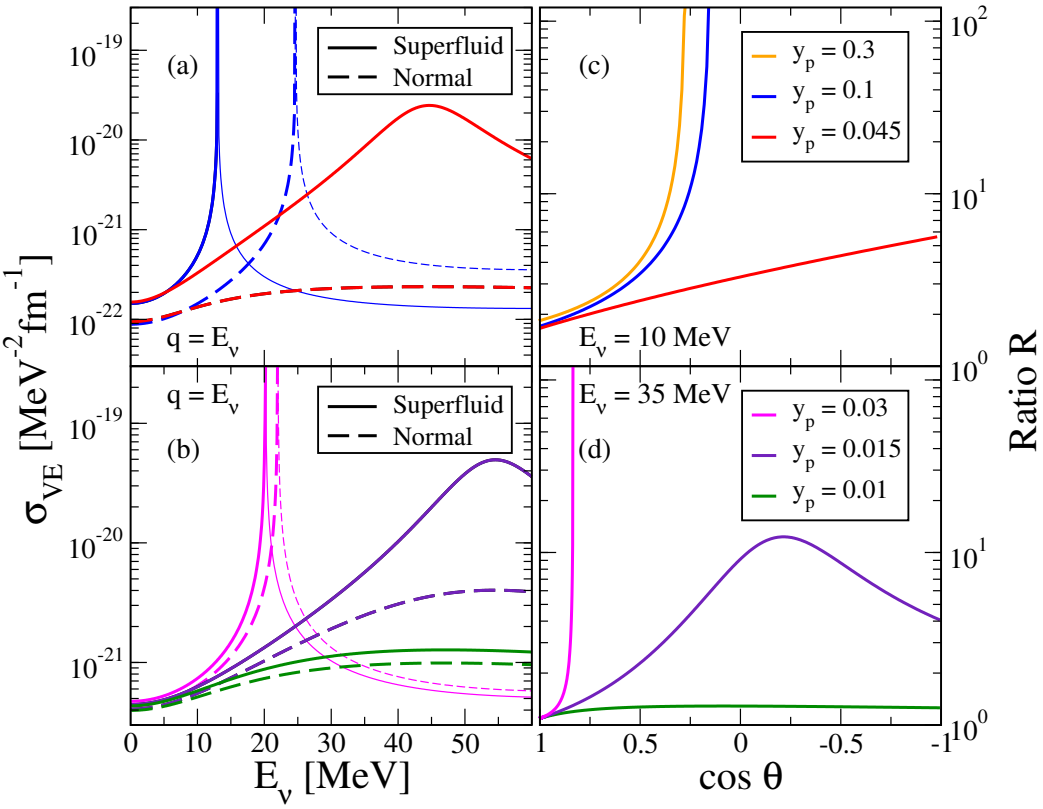

Figure 3.3: Left panels: neutrino differential cross sections, σ_{VE} (see text), as a function of the neutrino energy E_ν, obtained in the full calculation (strong pairing case, full lines) or neglecting the pairing interaction (dashed lines). Right panels: ratio R between the full calculation and the results obtained neglecting the pairing interaction, as a function of the cosine of the neutrino scattering angle θ, for selected neutrino energies. Results are shown for the following conditions: $\rho = \rho_0/100$ - T = 0.5 MeV (panels (a) and (c)) and $\rho = \rho_0/4$ - T = 1.4 MeV (panels (b) and (d)). The proton fractions considered are indicated inside the figure.

cillations are not much influenced by Coulomb (acting at small qs) or surface (acting at large qs) effects, so that λ_S remains close to zero for an appreciable range of the momentum transfer and the relative weigth of pairing effects is

clearly enhanced. As a consequence, an important influence of superfluidity emerges on the cross section, especially for intermediate neutrino energies, where a bump is observed. On the contrary, for the higher proton fraction case (see the result for $y_p = 0.1$), the matter crosses the spinodal border already for oscillations having low momentum transfer and a divergent behavior is observed for density fluctuations and neutrino cross section.

Clearly here one should carefully evaluate these density fluctuations going beyond the curvature of the free energy, but it is important to remark that, already at this level, a strong pairing effect on the neutrino opacity comes out. As a quite general result, in fact, one can observe that pairing interaction significantly reduce the curvature of the free energy density, leading to an increase of density fluctuations and related neutrino cross section. This effect, associated with neutron pairing, indicates that neutron correlations favour matter clustering. One can notice, moreover, that pairing correlations cause a not negligible shift to smaller values of the neutrino energy associated with the divergency in the full calculations. This implies that also less energetic neutrinos have more chances to be trapped, so that the energy flux carried away by neutrinos is necessary damped.

For $y_p = 0.1$, larger transfer momenta qs correspond instead to unstable oscillations and, since $\lambda_S(q)$ is negative, the prescription given in Eq. (3.14) does not hold to evaluate neutron and proton density fluctuations. Indeed, while the variance associated with isoscalar-like stable fluctuations reads as $\sigma_S(q) = T/\lambda_S(q)$, in presence of instabilities it grows exponentially with time to reach a new equilibrium condition, corresponding to clustered matter [47]. Therefore, the correct equilibrium fluctuations inside the spinodal region cannot be estimated within our framework. However assuming, as a first order approximation, that they are close to the value obtained, for each q, at a time of the order of the instability growth time (see [51]), one gets $\sigma_S(q) \approx T/|\lambda_S|$ and so the curvature matrix components Eq. (3.18) are modified accordingly. The corresponding neutrino cross sections are indicated by thin lines in Fig. 3.3. A similar behavior is observed at the higher proton fraction $y_p = 0.3$ (not shown on the panel (a)). The panel (b) displays the results obtained for case (2), where, as indicated by the analysis shown in

Fig. 3.2, we take smaller proton fractions y_p. We note that this also corresponds to the trend predicted for the proton fraction in the inner crust of neutron stars (see Table 4.1 in Chapter 4) [34, 64]. The same considerations made above for the lower density case hold. However here pairing effects, though still quite significant, are reduced with respect to the previous case, just because they are linked to the derivative of the pairing gap (and thus of the critical temperature) with respect to the density [32], which is steeper for case (1) (see Fig. 3.2). To emphasize the role of pairing effects, panels (c),(d) of Fig. 3.3 represent the ratio R between the cross section associated with the full calculations and the results obtained neglecting the pairing interaction, as a function of $\cos\theta$, for selected neutrino energies, representative of β–equilibrium conditions and for stable oscillations only. From this representation, it clearly emerges again how important pairing effects become approaching the spinodal border.

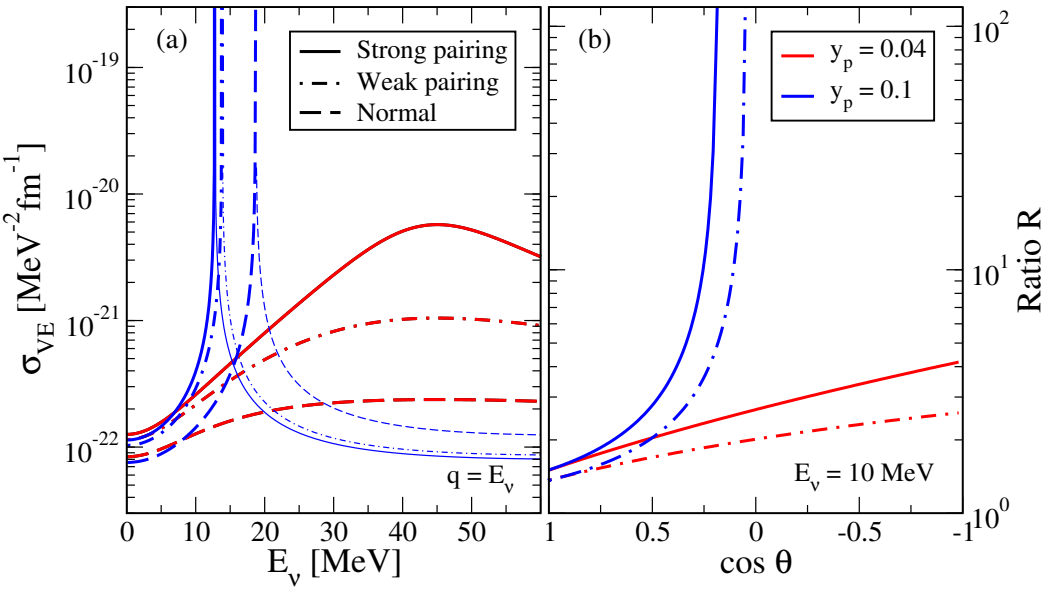

Figure 3.4: Same as in Fig. 3.3, for $\rho = \rho_0/100$ - T = 0.4 MeV, but employing the full calculation with the strong pairing (full lines) or weak pairing (dashed-dotted line) case, respectively.

Sensitivity to the strength of the pairing interaction. To explore the sensitivity of our results to the strength of the pairing interaction, calcula-

tions have been performed also for the weak pairing case. Results are shown in Fig. 3.4 for the lowest density case. Since, as one can observe in Fig. 3.2, the density derivative of the critical temperature is smaller in the case of the weak pairing, the influence of the pairing correlations on the neutrino cross section is reduced, though still appreciable. Clearly, the most important consequence of the weak pairing assumption is the strong reduction of the maximum critical temperature (see Fig. 3.2), which restricts considerably the range of applicability of our calculations.

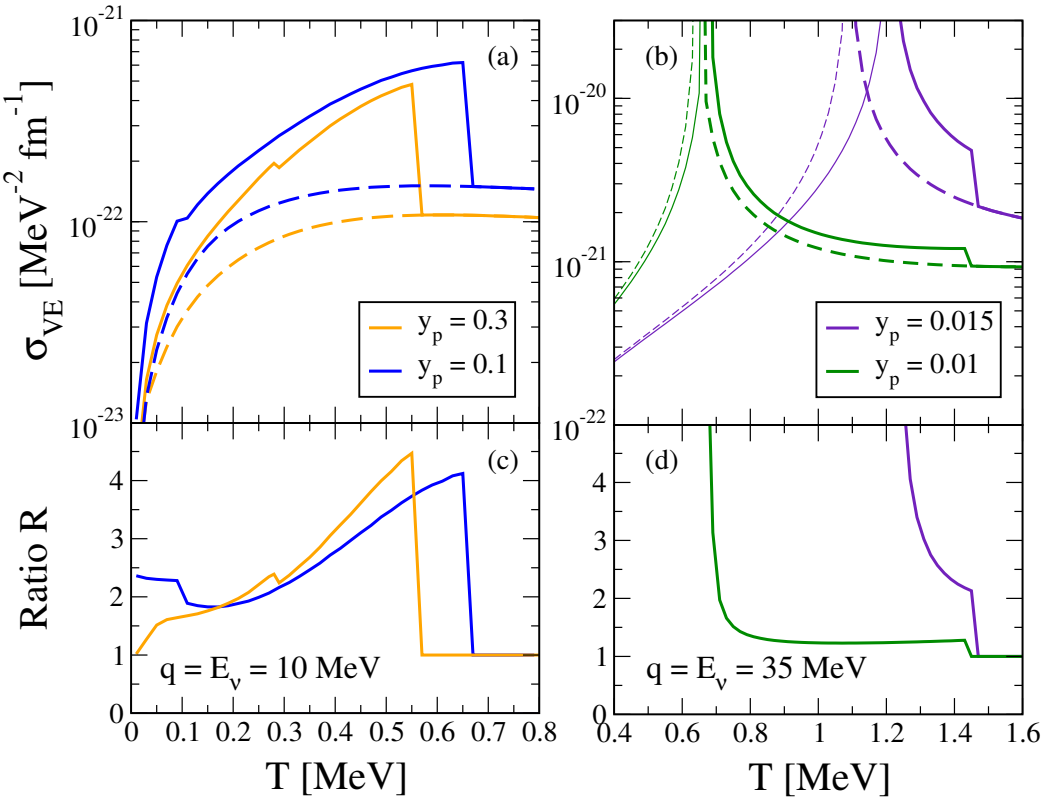

Figure 3.5: Top panels: Neutrino differential cross sections, σ_{VE} (see text), as a function of the temperature T, obtained in the full calculation (strong pairing case, full lines) or neglecting the pairing interaction (dashed lines).Results are shown for the following conditions: $\rho = \rho_0/100$ (panels (a) and (c)) and $\rho = \rho_0/4$ (panels (b) and (d)). The proton fractions considered are indicated inside the figure.

Temperature behavior of the cross section The influence of the temperature on our results is discussed in Fig. 3.5, where the quantity σ_{VE} is

displayed, for selected neutrino energies and $q = E_\nu$, as a function of T, for density conditions as in case (1) (panel (a)) and case (2) (panel (b)). The full calculations, performed for the strong pairing case, are compared to those obtained neglecting the pairing interaction.

The momentum transfer considered in panel (a) corresponds to stable oscillations. Pairing effects are quite important already at very low temperature, where *pp* pairing is also present, but they increase approaching the neutron critical temperature, $T_c \approx 0.65(0.55)$ MeV for $y_p = 0.1(0.3)$, and then vanish. Indeed, quite interestingly, we observe a jump in the cross section at $T = T_c$, which suddenly reaches the value of normal nuclear matter. A small jump also occurs, for both proton fractions, at a lower temperature, due to the disappearance of proton pairing. The jumps observed are related to the discontinuity emerging in the density derivative of the chemical potential, $\partial\mu_i/\partial\rho_i$, which has been addressed in section 2.5.2.

The conditions of panel (b) of Fig. 3.5 are such that the q value considered corresponds to fluctuations which are unstable at zero temperature. A divergency occurs for the cross sections at the temperature associated with the crossing of the spinodal border, whereas at higher temperature, density oscillations become stable. Also in this case a discontinuity is observed at the neutron critical temperature.

Final remarks. Some important final remarks are in order to conclude this chapter.

First of all, it should be noticed that our calculations are performed within the mean-field approximation. In this context, focusing on neutral current neutrino scattering and on the behavior of low-density matter, close to the spinodal border, we generally observe an increase of the neutrino differential cross section in paired matter, which enhances neutrino trapping and reduces the energy flux carried out by neutrino emission. In this way, new hints emerge about a significant impact of pairing effects on the cooling mechanism, by neutrino emission, of low-density stellar matter at moderate temperature.

However, it is important to make some warnings about our results and the approach adopted. First of all, in fact, one should consider that the

presence of large clusters, as the ones associated with the occurrence of spinodal instabilities, may influence significantly the evaluation of pairing effects in the inner crust of a neutron star [72]. Furthermore and probably more important, as shown by sophisticated analyses, clustering phenomena can affect the thermodynamical conditions of the low-density matter interacting with the neutrinos [147, 180]. Many-body correlations, going beyond our mean-field approach, are indeed responsible for the emergence of light clusters and extremely neutron-rich resonances, whose formation cannot be addressed within the spinodal mechanism. As it will be shown in the next chapter, this clusterization can significantly modify the global asymmetry of the matter and, correspondingly, the range of applicability of our results.

Horowitz and coworkers, in particular, have calculated both the static and the dynamic response function for the realistic case of clusterized matter [95, 96]. In these works, they have shown that the increase of the density fluctuation exists but is smaller than the one predicted by the mean field; clustered matter, in fact, does not exhibit the instability associated to the homogeneous mean-field approximation. Therefore, our hypothesis of homogeneous matter should be reconsidered. However, work is in progress to include these effects in our analysis, in order to find some configurations where also clusterized stellar matter is soft enough to allow an important relative weight for the pairing effect.

One advanced beyond-mean field model, which accounts for the nuclear clusters as degrees of freedom, will be instead employed in the next chapter, in order to give an estimation of the other key ingredient of the neutron star cooling process: the heat capacity.

Chapter 4

NSE cluster model: heat capacity of neutron stars

From Chapter 3, it has been mentioned that the crust thermalization time, which basically depends only on the cooling of the inner part, is strongly influenced by pairing correlations [72]. The specificity of the inner crust is the simultaneous presence of clusters and homogeneous matter, which are both influenced by pairing interactions. In Chapter 2, it has been shown how pairing correlations can affect the properties of clusterized matter. In a similar way, the occurrence of inhomogeneities has a non-negligible influence on the pairing properties of the inner crust [18, 45, 72, 137, 158], and consequently on the time evolution of the surface temperature of the neutron star. Hence, the study of the inner crust cooling and, in particular, the evaluation of its heat capacity is a problem far from trivial.

In this chapter, we are going to deal with this question, in the framework of an extended version of the Nuclear Statistical Equilibrium (NSE) model [147], which accounts for both mean-field and pairing correlations [34].

4.1 Beyond mean-field and cluster approach

Present studies of crust superfluidity at finite temperature are typically done by solving the mean-field Hartree-Fock-Bogoliubov (HFB) equations in the

so-called single nucleus approximation [125], i.e., assuming that the cluster component is given by a single representative quasi-particle configuration, corresponding to a single representative nucleus immersed in a neutron gas. These works do not consider the fact that at finite temperature a wide distribution of nuclei is expected to be populated at given crust pressure and temperature conditions.

Furthermore, at the extremely low proton fractions associated to the inner crust, deformed nuclear structures and light nuclear resonances beyond the drip-line can appear, which might be too exotic to be well described by standard mean-field calculations. At sufficiently high temperatures, light particles can even become dominant in the composition of matter [6, 153], modifying the local distribution of neutron density and the associated pairing field.

A way to include these beyond-mean field effects is given by finite temperature Nuclear Statistical Equilibrium (NSE) models.

4.1.1 Extended Nuclear Statistical Equilibrium model

The most recent NSE implementations [37, 74, 93, 94, 147, 148] are based on a full distribution of clusters, obtained self-consistently under conditions of statistical equilibrium. In the following, we discuss in particular the main features of the NSE model developed by Gulminelli and Raduta [148], where a statistical distribution of compressible nuclear clusters immersed in a homogeneous background of self-interacting nucleons and electrons is taken into account.

This approach, however, was not adequate to describe the heat capacity of the crust because it did not consider the presence of pairing correlations. The aim of our recent work has been therefore to extend the NSE model, by introducing pairing correlations both in the cluster and homogeneous matter components and to study the effect of the cluster distribution on the heat capacity of the inner crust.

At the same time, it is interesting to analyze how the non-homogeneity of the crust matter and the associated wide distribution of nuclear species

can affect the superfluid properties of the crust.

Density and bulk asymmetry. We label each nuclear species by its mass number and bulk asymmetry (A, δ). Even below drip, the asymmetry in the bulk for a nucleus in the vacuum, δ_0 differs from the global asymmetry I of the nucleus because of the presence of a neutron skin and Coulomb effects. The relation between δ_0 and I is given in Refs. [123, 190]:

$$\delta_0 = \frac{I + \frac{3a_C}{8Q}\frac{Z^2}{A^{5/3}}}{1 + \frac{9E_{sym}}{4Q}\frac{1}{A^{1/3}}}, \tag{4.1}$$

where E_{sym} is the symmetry energy (Eq. (1.54)) at saturation, Q is the surface stiffness coefficient extracted from a semi-infinite nuclear matter calculation [124] and a_C is the Coulomb parameter of Eq. (2.2).

The continuum states leading to the existence of a free nucleon gas can in first approximation be modelled as a constant density contribution. As a consequence, the bulk asymmetry inside the clusters can be decomposed into the asymmetry of the gas δ_g weighted by the gas fraction $x_g = \rho_g/\rho_0^b$ inside the cluster, plus the asymmetry of the cluster in the vacuum δ_0 weighted by the complementary mass fraction $x_{cl} = (\rho_0^b - \rho_g)/\rho_0^b$, namely

$$\delta = \left(1 - \frac{\rho_g}{\rho_0^b}\right)\delta_0 + \frac{\rho_g}{\rho_0^b}\delta_g. \tag{4.2}$$

In the previous equation ρ_0^b denotes the bulk density, which corresponds to the saturation density at the corresponding bulk asymmetry. This means that, at the second order in asymmetry, the following expression can be used for the bulk density [135]:

$$\rho_0^b = \rho_0\left(1 - \frac{3L\delta^2}{K + K_{sym}\delta^2}\right), \tag{4.3}$$

where L and K_{sym} are the slope and the curvature of the symmetry energy at saturation density, as defined in Eq. (1.55), whereas K is the incompressibility modulus defined in Eq. (1.62). Then, solving the coupled Eqs. (4.2) and (4.3),

it is possible to extract the bulk density and asymmetry.

Free energy density of the superfluid nucleon gas. The free energy density of the nucleon gas of density ρ_g and asymmetry δ_g is obtained in the mean-field approach adding the entropy term $\mathcal{S}_{HM}$ to the energy density $\mathcal{E}_{HM}$ as deduced in the local BCS approximation in Eq. (3.16):

$$\mathcal{F}_{HM}(\rho_g, \delta_g) = \mathcal{E}_{HM}(\rho_g, \delta_g) - T\mathcal{S}_{HM}(\rho_g, \delta_g). \tag{4.4}$$

According to the definition given in Eq. (1.58), the entropy density is given by :

$$\mathcal{S}_{HM}(\rho_g, \delta_g) = -2 \sum_{q=n,p} \int \frac{d\mathbf{p}}{(2\pi)^3} [n_q \ln n_q + (1 - n_q) \ln (1 - n_q)], \tag{4.5}$$

where $n_q = \frac{1}{1+\exp(E_q^{\Delta}/T)}$ is the Fermi distribution for the quasi-particles.

The cluster distribution. A given thermodynamic condition in terms of temperature, baryonic density and proton fraction (T, ρ_B, y_p) is characterized by a mixture of configurations defined by $k = \{V_{WS}^{(k)}, A^{(k)}, \delta^{(k)}, \rho_g, \delta_g\}$ with a free energy given by [88]:

$$F_{WS}^{(k)} = F_{cl}(A^{(k)}, \delta^{(k)}, \rho_g, \delta_g) + V_{WS}^{(k)} \mathcal{F}_{HM}(\rho_g, \delta_g) + V_{WS}^{(k)} \mathcal{F}_{el}(\rho_p). \tag{4.6}$$

In the latter expression, $\mathcal{F}_{el}$ is the electron free-energy density, ρ_p is the total proton density, $V_{WS}^{(k)}$ denotes the Wigner Seitz cell volume and F_{cl} is the free energy of the cluster immersed in the nucleon gas:

$$F_{cl}(A, \delta, \rho_g, \delta_g) = E^0(A, \delta) - TS_t + \delta F_{bulk} + \delta F_{surf} + \delta F_{Coul}. \tag{4.7}$$

We can observe that the cluster energy is modified with respect to the corresponding vacuum energy E^0 owing to both nuclear and Coulomb in-medium effects. The modification of the nuclear free-energy consists of a bulk term

$$\delta F_{bulk} = -\mathcal{F}_{HM}(\rho_g, \delta_g) V_{cl}, \tag{4.8}$$

due to the presence of the gas in the same effective spatial volume $V_{cl} = \frac{A}{\rho_0(\delta)}$ occupied by the cluster, and a surface term δF_{surf} which accounts for the modification caused by the gas at the surface of the cluster. The calculation of the latter term will be in particular detailed in section 4.4. The screening effect of electrons which neutralize the Wigner-Seitz cell leads to a modification of the cluster free-energy according to:

$$\delta F_{coul} = a_c f_{WS}(\rho_p, \rho_{0p}) A^{5/3} \frac{(1-I)^2}{4}, \tag{4.9}$$

with $\rho_{0p} = \rho_0(1-\delta)/2$ and the Coulomb screening function in the Wigner-Seitz approximation written as

$$f_{WS}(\rho_p, \rho_{0p}) = \frac{3}{2}\left(\frac{\rho_p}{\rho_{0p}}\right)^{1/3} - \frac{1}{2}\left(\frac{\rho_p}{\rho_{0p}}\right). \tag{4.10}$$

In Eq. (4.7), we have also introduced the translational entropy

$$S_t = \ln\left(g_T V A_e^{\frac{3}{2}}\right). \tag{4.11}$$

In the latter expression, we label with V the total volume, while g_T represents the temperature dependent degeneracy factor, which includes the sum over the cluster excited states as:

$$g_T = \left(\frac{mT}{2\pi}\right)^{3/2} \int_0^{<S>} dE \left[\varrho_{A,\delta}(E) e^{-E/T}\right], \tag{4.12}$$

where $\varrho_{A,\delta}$ is the density of states of the cluster, while $\langle S \rangle$ is the minimum of the average particle separation energies of neutrons and protons. However, mean-field models are known to be far off in the reproduction of these observables, and empirical adjustements have to be done. For this reason we use a back-shifted Fermi gas model with parameters fitted from experimental data [188] (see [88] for more details). Moreover, to insure additivity of the cluster and the gas component, only the bound part of the cluster $A_e = A\,(1 - \rho_g/\rho_0)$ appears in the translational term of Eq. (4.7).

Concerning the cluster binding energy $E^0(A, \delta)$, theoretical coherence

with the treatment of the gas demands that it is evaluated with the same EDF employed for the gas component. So, we adopt the analytical expression proposed in [54]:

$$E^0 = a_V A - a_S A^{2/3} - a_I(A) A I^2 - a_C A^{5/3} \frac{(1-I)^2}{4}, \tag{4.13}$$

with the asymmetry energy coefficient:

$$a_I(A) = \frac{a_V^I}{1 + \frac{a_V^I}{a_S^I A^{1/3}}}, \tag{4.14}$$

where the parameters are fitted from numerical Skyrme calculations in slab geometry [54]. The pairing contribution to the cluster energy is evaluated according to the phenomenological expression: $\Delta(A) = \pm 12/\sqrt{A}$, where the +(-) sign refers to even-even (odd-odd) nuclei. It is important to observe that the formula in Eq. (4.13), similarly to any other mean-field model, systematically underbinds light particles, which will then tend to be underestimated in the calculations. We will discuss the effect of this limitation in section 4.3.3.

Analogously to the definition of A_e, one may also introduce the bound charge fraction of the cluster as $Z_e = Z\,(1 - \rho_{gp}/\rho_{0p})$, so that the volume of the Wigner-Seitz cell associated to each nuclear species turns out to be univocally defined by the charge conservation constraint:

$$\rho_p = \rho_e = \frac{Z_e}{V_{WS}} + \rho_{gp}, \tag{4.15}$$

which leads to

$$V_{WS} = \frac{Z}{\rho_{0p}} \frac{\rho_{0p} - \rho_{gp}}{\rho_p - \rho_{gp}}. \tag{4.16}$$

The equilibrium distribution is obtained by minimizing the total free energy corresponding to an arbitrary collection of different cells k, subject to the constraints of total baryonic and charge density conservation [88]:

$$\rho_B = \frac{\sum_k n^{(k)} (A_e^{(k)} + V_{WS}^{(k)} \rho_g)}{\sum_k n^{(k)} V_{WS}^{(k)}}, \tag{4.17}$$

$$\rho_p = \frac{\sum_k n^{(k)}(Z_e^{(k)} + V_{WS}^{(k)}\rho_{gp})}{\sum_k n^{(k)} V_{WS}^{(k)}}. \tag{4.18}$$

The result is a NSE-like expression for the cluster multiplicities $n^{(k)}$ [88]:

$$\ln n^{(k)} = -\frac{1}{T}\left[F_{cl}(A^{(k)}, \delta^{(k)}, \rho_g, \delta_g) - \mu_B A_e - \mu_p Z_e\right], \tag{4.19}$$

where the chemical potentials can be expressed as a function of the gas densities only:

$$\mu_B \equiv \frac{\partial \mathcal{F}_{HM}}{\partial \rho_g}, \tag{4.20}$$

$$\mu_p \equiv \frac{\partial \mathcal{F}_{HM}}{\partial \rho_{gp}}. \tag{4.21}$$

The numerical solution of the two Eqs. (4.18) for the two unknowns ρ_g, ρ_{gp} closes the model. The results obtained with the improved model described above are presented in the next section.

4.2 Composition of the inner crust

In order to facilitate a quantitative comparison with previous works, we have chosen ten representative values for the baryonic density which have been proposed in the seminal paper by Negele and Vautherin [125]. These values cover the inner crust of the neutron star, approximately from the emergence of the neutron gas close to the drip point (cell 10) to a density close to the crust-core transition (cell 1), where bubbles and possibly other exotic nuclear shapes, not included in our model, start to form.

The corresponding values of the baryonic density, as well as the proton fraction, the gas density and the average value of the Wigner-Seitz cell radius we obtain by imposing the neutrino-less β-equilibrium condition (Eq. (3.3)) at the lowest temperature ($T = 100$ keV) considered in this study, are given in Table 4.1. For comparison, proton fraction, gas density and radius of Wigner-Seitz cell obtained at zero temperature in the full HFB calculation

Table 4.1: From left to right are given: the total baryonic density, the proton fraction at T=100 keV, the proton fraction at T=0 considered in [72], the gas density at T=100 keV, the gas density obtained at T=0 in [72], the radius (in fm) of the average Wigner-Seitz volume calculated at T=100 keV and the radius (in fm) of the cell at T=0 calculated in [72].

Cell	ρ_B [fm^{-3}]	y_p^0	$y_p^{\rm HFB}$	ρ_g^0 [fm^{-3}]	$\rho_g^{\rm HFB}$ [fm^{-3}]	$\langle R_{WS}^0 \rangle$	$R_{WS}^{\rm HFB}$
1	4.8×10^{-2}	0.032	0.027	3.9×10^{-2}	3.8×10^{-2}	9	20
2	2.0×10^{-2}	0.035	0.028	1.7×10^{-2}	1.7×10^{-2}	22	28
3	9.0×10^{-3}	0.040	0.037	7.5×10^{-3}	7.5×10^{-3}	30	33
4	5.8×10^{-3}	0.045	0.045	4.8×10^{-3}	4.6×10^{-3}	33	36
5	3.7×10^{-3}	0.054	0.053	3.0×10^{-3}	3.0×10^{-3}	36	39
6	1.6×10^{-3}	0.083	0.080	1.2×10^{-3}	1.1×10^{-3}	41	42
7	9.0×10^{-4}	0.122	0.125	5.4×10^{-4}	5.3×10^{-4}	44	44
8	6.0×10^{-4}	0.162	0.160	2.8×10^{-4}	2.8×10^{-4}	46	46
9	4.0×10^{-4}	0.220	0.200	1.2×10^{-4}	1.3×10^{-4}	47	49
10	2.8×10^{-4}	0.284	0.222	2.8×10^{-5}	7.4×10^{-5}	48	54

employing the single nucleus approximation in [72] are also given in the same table. As in [72], the SLy4 Skyrme parametrization (see Table 1.1) for the energy density functional of the gas is adopted. This parameterization is in fact specifically fitted to reproduce heavy neutron-rich nuclei ground states and properties of neutron matter. The parameters for the pairing effective interaction in Eq. (2.33), obtained by assuming a strong pairing scenario (see Fig. 3.2 or Fig. 2.4), are correspondingly deduced and listed in the following: V_π^Λ = -931.83 MeV fm^3, η_π = 0.815 and α_π= 0.364.

As a general feature, we notice that the proton fraction increases, whereas the gas density decreases moving from cell 1 to cell 10.

Comparing the results from the two different models, as far as the gas density is concerned, the difference between the HFB values and our results, at the lowest temperature considered, is of the order of 2% or less, except for the lowest density case. This residual variation can be partly due to the different description of the cluster energy. Our simplified mass model from [54] is augmented of a phenomenological pairing term [88] but does not contain shell effects. Neutron shell effects do not play any role above drip, but proton shell closures are known to be still effective at zero temperature in the inner

crust [138]. This contribution can then slightly affect the neutron gas density close to the drip condition. More important, a quite significant difference in the density dependence of the pairing gap employed in the two calculations is the main origin of the variation observed, as it will be highlighted in the next section. Concerning the radius of the average volume of the Wigner-Seitz cell, again our results are in good agreement with HFB, except at the highest density (Cell 1). As it is shown in the following, this difference is due to the dominance of light resonances in our calculation, which are not included in a mean-field approach.

4.2.1 Proton fraction evolution with the temperature

In most HFB calculations related to the cooling problem [18, 45, 72, 137, 158], an approximation made is that the proton fraction does not evolve with the temperature and can be estimated by the value imposed, at each baryonic density, by the condition of neutrino-less chemical equilibrium at zero temperature in reference calculations [125]. Even with the inclusion of pairing, the NSE model is still much less numerically demanding than a full HFB calculation at finite temperature. For this reason, we have released this approximation and imposed Eq. (3.3) at each finite temperature. This condition is justified by the fact that the time scale of neutron star cooling is sufficiently slow to insure the chemical equilibrium of weak processes at all times [78].

The global proton fraction evolution with the temperature obtained by imposing consistently the neutrino-less β-equilibrium condition at each T value is illustrated in Fig. 4.1, for four representative cells spanning the density and temperature interval concerned by this study.

One can notice that the change of the proton fraction is very small close to the crust-core transition (up to cell 4), but it cannot be neglected at lower densities (cells 5 to 10), so important effects can be expected close to the drip point because of the temperature evolution of y_p along a β-equilibrium path of the star.

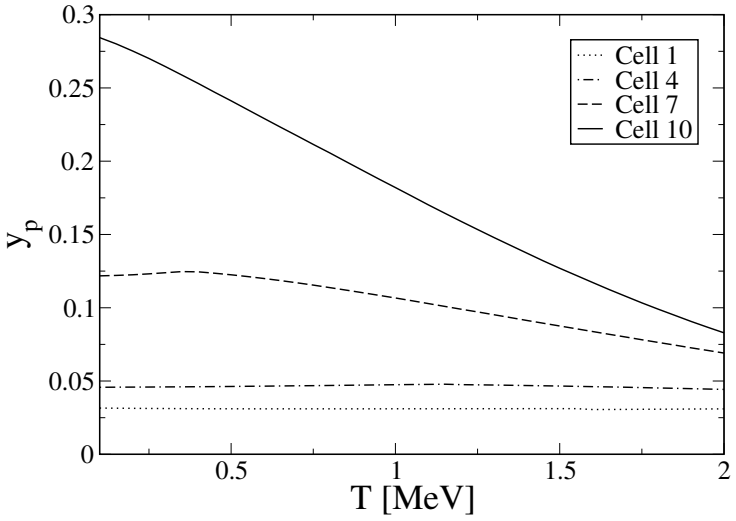

Figure 4.1: Temperature evolution of the global proton fraction y_p obtained by imposing the neutrino-less β-equilibrium condition Eq. (3.3) for four representative cells.

4.2.2 Temperature behavior of the unbound component

The density corresponding to the unbound neutron component is shown in Fig. 4.2 for the same baryonic density conditions as in Fig. 4.1. One can appreciate the impact of the β-equilibrium condition on the gas density by comparing full and dashed lines. It clearly emerges that the β-equilibrium condition should be consistently implemented at each temperature, especially in the outer layers of the inner crust.

In order to evidence some possible superfluid effects, the full calculation has been repeated neglecting the pairing interaction (dotted curve). Pairing comes to be responsible for the most striking feature observed in Fig. 4.2: the appearance of a discontinuity at the highest densities (up to cell 4 in the present calculation), corresponding to the transition point from superfluid to normal matter. At first sight it is surprising to observe a density discontinuity, which is characteristic of first order phase transitions, at the pairing transition, which, as it has been stressed in section 2.5.2, is a second order one. Actually, this behavior is due to the fact that we are not observing an equation of state but a specific thermodynamic transformation implied by the minimization of the total free energy of the system.

Specifically, one should consider that the pairing gap jumps, in a continous but abrupt way, to zero at the critical temperature. This behavior

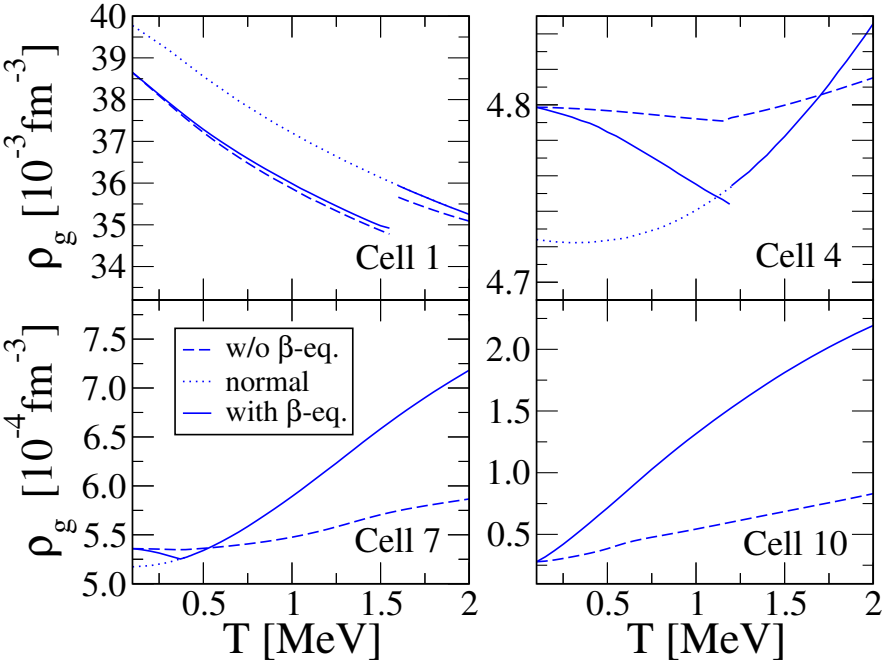

Figure 4.2: Temperature evolution of the unbound component density ρ_g in the same representative cells as in Fig. 4.1. Full line: complete NSE calculation. Dashed line: the value of the global proton fraction is assumed equal to the one calculated from β-equilibrium at the lowest temperature, $y_p(T) = y_p(0.1\text{MeV})$. Dotted line: as the full line, but neglecting the pairing interaction.

influences the energetics of the system and hence may create discontinuities in the solution obtained for the gas density. This is particularly evident in the cells where, as in Cell 1, the gas density is larger than the value associated with the maximum gap (see Fig. 2.8). In this case, the gas density solution corresponding to zero temperature in the full NSE calculation is lower than the one obtained neglecting the pairing interaction (dotted line in Fig. 4.2), because it corresponds to a larger gap energy. As the temperature increases, in the regime where pairing is still active, the gas density decreases because the (negative) pairing contribution to the gas energy reduces. At the critical temperature the non-superfluid solution is recovered as it should, then this corresponds to a higher density value and may lead to a discontinuity.

4.2.3 Mass and isotopic distribution of clusters

The mass distribution of clusters as a function of the temperature is displayed in Fig. 4.3, where $p^{(k)} = n^{(k)}/n_{tot}$ denotes the normalized cluster multiplicity, with $n_{tot} = \sum_k n^{(k)}$ the total cluster multiplicity.

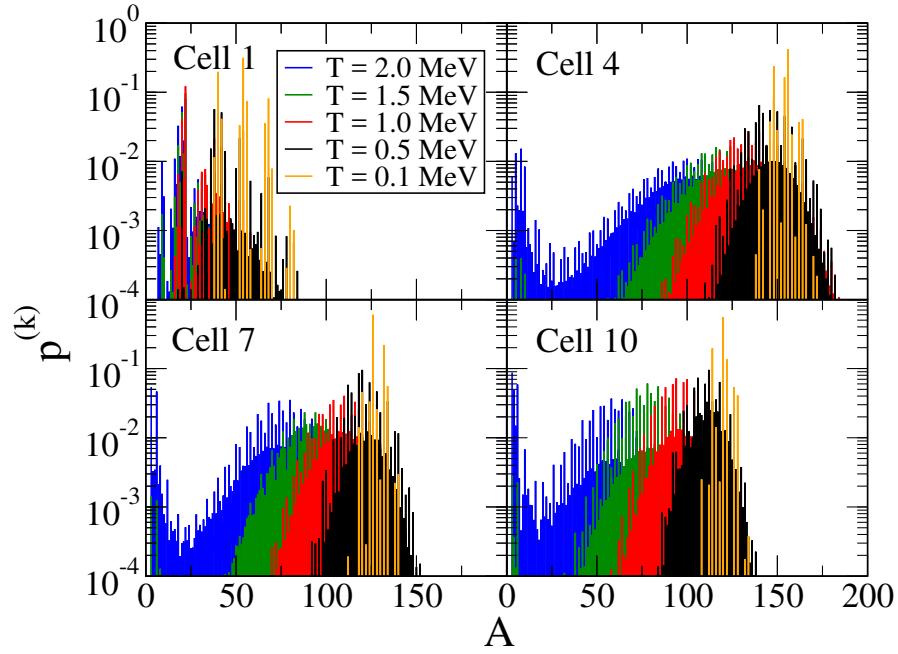

Figure 4.3: Normalized mass cluster distribution at different temperatures in the same four representative cells as in Fig. 4.1 and along a β-equilibrium trajectory.

We can see that at the lowest densities and temperatures the distribution is strongly peaked and can be safely assumed to be constituted only by a unique nucleus. However increasing the temperature and/or moving towards the inner part of the crust, many different nuclear species can appear with comparable probability. Light particles in particular systematically dominate at the highest temperatures. Close to the crust-core transition, instead, the matter is so neutron rich (see Fig. 4.1) that standard heavy clusters are not favored anymore even at very low temperature. In these thermodynamic conditions, the mass distribution extends up to $A \approx 100$ but light resonances prevail by far.

These clusters, which cannot be addressed in mean-field based formalisms like HFB, may be really exotic objects at the limit of the nuclear binding, as

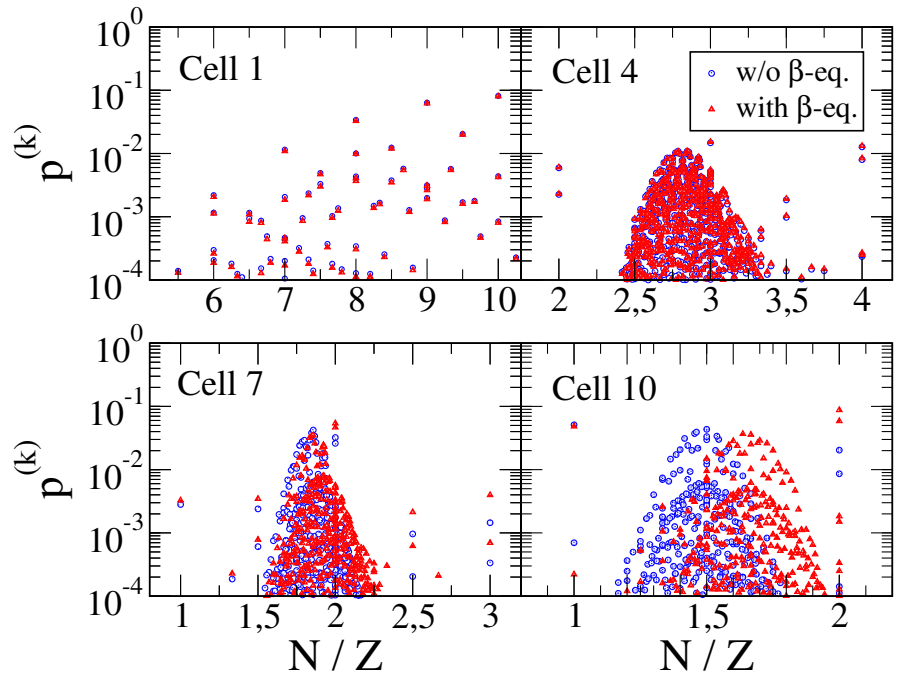

Figure 4.4: Normalized isotopic cluster distribution in the same four representative cells as in Fig. 4.1, as obtained at the highest temperature considered, $T = 2$ MeV. The different symbols indicate results at β-equilibrium (triangle) or assuming a global proton fraction equal to that one corresponding to β-equilibrium but at the lowest temperature, $y_p(T) = y_p(0.1\text{MeV})$.

one can deduce looking at the Fig. 4.4, where the normalized isotopic cluster distribution is plotted, for the same four cells and at the highest temperature considered in our study. In the same figure, the results obtained neglecting the proton fraction wvolution with the temperature are also shown. In such a way one can observe that, especially for the lowest density cells (Cells 7 and 10), the cluster asymmetry is significantly larger when the β-equilibrium condition is imposed. It is also interesting to notice that, at the high limits of the N/Z distribution, the yield is higher than the corresponding value obtained in absence of β-equilibrium. These N/Z values are obtained from the lightest clusters (see Fig. 4.3), which dominate at the temperature considered. Thus, the contribution of the most unbound clusters increases properly accounting for the β-equilibrium condition. From these results, one can foresee on the one hand that the Single Nucleus Approximation (SNA) is perfectly

adequate in some regions of the inner crust, but non-negligible effects of the cluster distribution are expected to appear especially close to the crust-core transition. On the other hand, neglecting the temperature evolution of β-equilibrium will lead to a strong underestimation at high temperature of the energy density and the associated specific heat, discussed in the next section.

4.3 Baryonic energy density and specific heat

In some early studies [112, 143], for the calculation of energy density and specific heat, the cluster contribution was completely ignored, and the nonuniform distribution was replaced with a uniform gas formed by the total number of neutrons in the cell or only by the number of the unbound neutrons. It has been shown in [72] that these approximations reproduce very poorely the baryonic specific heat of a complete HFB calculation: the shape of the peak is too sharp, and the transition temperature is underestimated.

In this section, we evaluate both energy density and specific heat considering the full NSE distribution but approximating the contribution of the cluster and the gas as simply additive, which corresponds to neglecting the term δF_{surf} in Eq. (4.7). The in-medium effects will be then introduced in section 4.4.

4.3.1 Excluded volume method

To compute the contribution of the gas to the energy density in the simplified hypothesis $\delta F_{surf} = 0$, we have to consider the volume V_g accessible to the gas, i.e., the volume left after excluding the volume of the clusters, and evaluate the corresponding gas volume fraction $x_g = \lim_{V\to\infty} \frac{V_g}{V}$. In the SNA employed in HFB calculations, we can consider a single representative Wigner-Seitz cell and write $x_g^{SNA} = 1 - V_{cl}/V_{WS}$.

Since in the NSE model the full distribution of clusters is accounted for,

the volume fraction x_g accessible to the gas results as

$$x_g = 1 - \lim_{V\to\infty} \frac{1}{V} \sum_k n^{(k)} \frac{A^{(k)}}{\rho_0(\delta^{(k)})}, \tag{4.22}$$

so the gas contribution to the energy density becomes:

$$\mathcal{E}_g = \mathcal{E}_{HM}\ x_g = \mathcal{E}_{HM} \left(1 - \frac{1}{\langle V_{WS} \rangle} \sum_k p^{(k)} \frac{A^{(k)}}{\rho_0(\delta^{(k)})} \right), \tag{4.23}$$

where the total volume has been written as $V = n_{tot}\langle V_{WS}\rangle$, being $\langle V_{WS}\rangle$ the average size of the Wigner-Seitz volume.

In this way, we finally get the following total baryonic energy density of star matter:

$$\mathcal{E}_{tot} = \mathcal{E}_g + \mathcal{E}_{cl} = \mathcal{E}_g + \frac{1}{\langle V_{WS} \rangle} \sum_k p^{(k)} \langle E(A^{(k)}, \delta^{(k)}) \rangle, \tag{4.24}$$

where the energy $E(A, \delta)$ is given by the vacuum energy value E^0 of Eq. (4.13), shifted by the electron screening effect $\delta E_{Coul} = \delta F_{Coul}$, and augmented of the average translational energy $\frac{3}{2}T$ and excitation energy $\langle E^* \rangle$ corresponding to the considered temperature and cluster density of states [88], so

$$\langle E(A, \delta, \rho_p, T) \rangle = E^0(A, \delta) + \delta E_{Coul}(A, \delta, \rho_p) + \frac{3}{2}T + \langle E^*(A, \delta, T) \rangle. \tag{4.25}$$

As shown by Eq. (4.7), this excluded volume effect can be simply formulated as the additivity of the gas with the bound part of the clusters.

4.3.2 Temperature behavior of energy and its derivative

The variation with temperature of the energy density is displayed, for the same density conditions as in the previous figures, in Fig. 4.5.

The effect of the temperature dependence of the β-equilibrium condition can be appreciated comparing the full thin lines with the dashed lines. As expected, we can see that the temperature evolution of the proton fraction has a strong effect on the energy density, especially at the lowest densities.

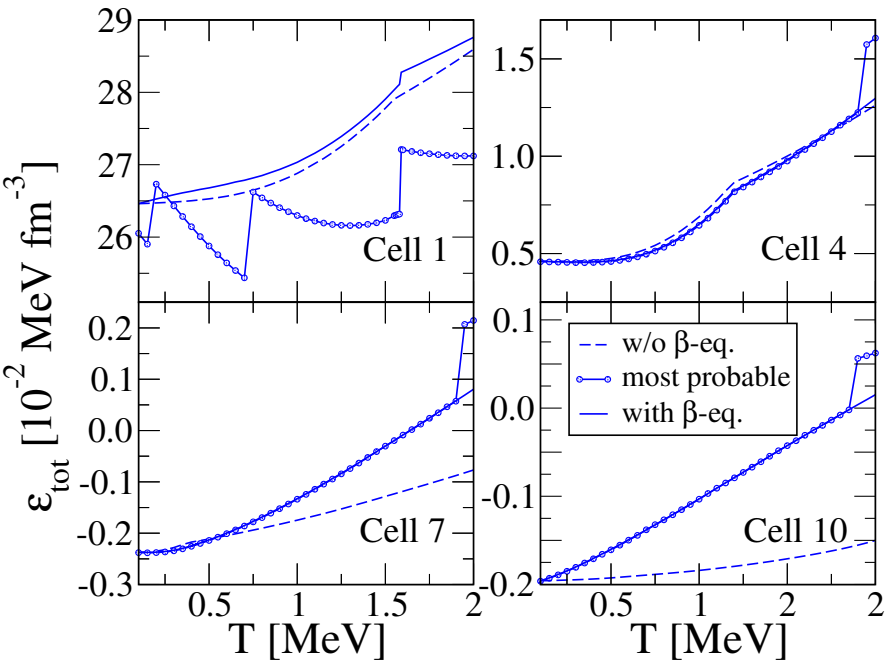

Figure 4.5: Temperature evolution of the baryonic energy density for the same representative cells as in Fig. 4.1. Full line: complete NSE calculation. Dashed line: as the full line, but the value of the global proton fraction is assumed equat to that one calculated from β-equilibrium at the lowest temperature, $y_p(T) = y_p(0.1\text{MeV})$. Lines with symbols: as the full line, but the NSE distribution is replaced with the most probable Wigner-Seitz cell.

The lines with symbols show instead the energy density of the most probable Wigner-Seitz cell, to be compared to the complete result (full lines) where the whole distribution of cells is taken into account. We can see that the effect of properly accounting for the cluster distribution is very important at the highest densities, but also at the lowest ones when the temperature gets higher; these situations are indeed dominated by the emergence of light clusters.

The energy density associated with the full distribution is very different from the one associated with the most probable cluster. Specifically, the discontinuities observed in the lines with symbols in Fig. 4.5 appear at the temperatures where a variation on the most probable element in the Wigner Seitz cell occurs.

This is more pronounced in Cell 1, where several peaks emerge in the

temperature evolution of the energy density, for the most probable case. Actually, it is important to remark that in this density region in principle non-spherical pasta phases, which are not included in our work, could dominate over the light resonances. This is certainly true for low temperatures and almost isospin-symmetric matter where the breaking of spherical symmetry leads to an important gain in binding energy [191]. However finite temperature calculations tend to show that non-spherical pasta phases are only marginally populated in β-equilibrium [6], meaning that the energy behavior displayed in Fig. 4.5 might be physical. A similar transition, from heavy cluster to light resonance dominated configurations is then observed at higher temperature in each other cell, where anyway the density is too low for pasta phases to be present. This transition, leading to a sharp discontinuity in the energy density of the most probable Wigner-Seitz cell, physically corresponds to the melting of clusters inside a hot medium. In a mean-field treatment, cluster disappearence can only lead to an homogeneous medium, because small wavelength fluctuations cannot be treated in these approaches. However, the NSE treatment clearly demonstrates that such fluctuations are entropically favored and naturally appear at high temperature.

The transition temperature from the superfluid to the normal fluid phase is signaled by a kink in the behavior of the energy density, which will lead to a peak in the associated specific heat. This transition occurs at the same point, for full NSE calculations or considering only the most probable Wigner-Seitz cell, because electron and nucleon gases are uniform along the different Wigner Seitz cells, meaning that by construction the density and isospin characteristics of the gas are the same in the two calculations. On the contrary, it is interesting to observe that a shift in the critical temperature of the superfluid phase transition would be observed if a SNA calculation is performed [88], as in the well-known Lattimer-Swesty model [111]. Indeed the baryonic density of the gas associated to the Wigner-Seitz cell of the single representative cluster is not the same as the total distribution. This is a consequence of the fact that, especially at high temperature, the most probable cluster can be very different from the average cluster, thus it is very important to consider the full cluster distribution, as in the NSE calculations.

This means that the consideration of the cluster distribution could modify the transition temperature, though the effect is expected to be small.

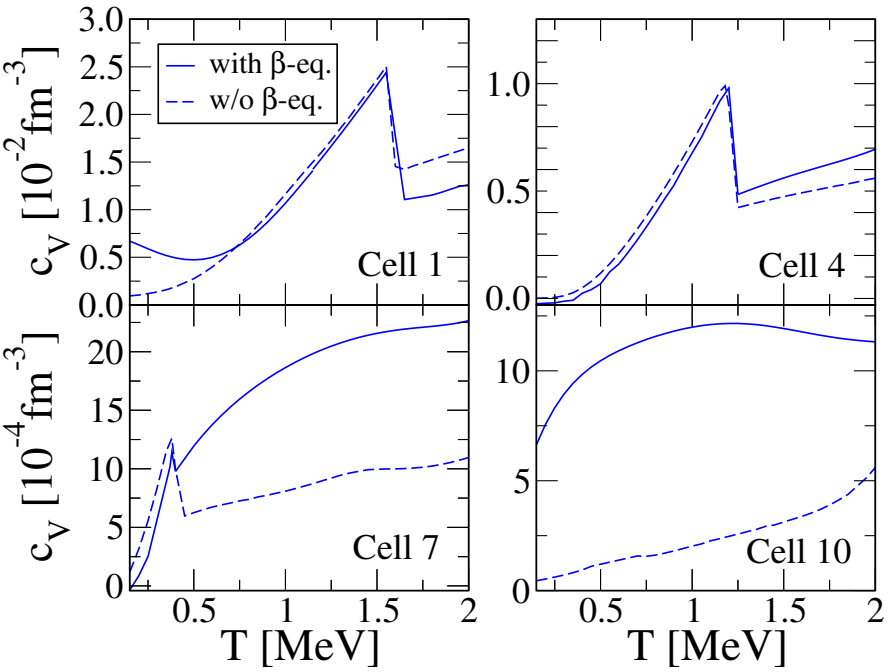

Figure 4.6: Temperature evolution of the baryonic specific heat for the same representative cells as in Fig. 4.1. Full line: complete NSE calculation. Dashed line: as the full line, but the value of the global proton fraction is assumed equal to that one calculated from β-equilibrium at the lowest temperature, $y_p(T) = y_p(0.1\text{MeV})$.

The temperature behavior of the total baryonic energy derivative with respect to temperature is shown in Fig. 4.6, in four different cells. The temperature derivative was performed numerically following the trajectory of β-equilibrium: this means that, in the full calculation, only the total baryonic density is constant, but the proton fraction is not. As we have anticipated observing the energy density behavior of Fig. 4.5, the temperature dependence of the β-equilibrium condition is seen to have a dramatic effect on the baryonic specific heat. In particular the peak due to the phase transition is strongly smeared out in the outer region of the inner crust, from cell 7 to 10, due to the rapid variation of the unbound component with temperature implied by the β-equilibrium condition (see Fig. 4.2). On the contrary, at the highest densities (cells 1 to 3) the consideration of the temperature variation

of the proton fraction increases the size of the peak. Indeed, in this case the β-equilibrium path favors a discontinuous trend of all thermodynamic quantities at the transition point (see Fig. 4.2).

4.3.3 Mass functional and experimental masses

In all the calculations presented in the previous sections, we have systematically used the Skyrme-based Liquid Drop Model (LDM) formula given in Eq. (4.13). This choice allows a consistent treatment of the bound and unbound matter component within the same energy functional. However, as already stressed, light clusters are systematically underbound with respect to heavier ones. To give an example, employing the parameters extracted in [54] for SLy4, the binding energy of an α particle is underestimated of $\left(\frac{\Delta B}{B}\right)_\alpha = 20$ % while it is overestimated of $\left(\frac{\Delta B}{B}\right)_{Pb} = 13$ % for ^{208}Pb. This effect is even more dramatic for the most neutron rich light resonances, at the limit of nuclear binding, which can in principle be excited in the extremely neutron rich β-equilibrated matter of proto-neutron stars at finite temperature: the last bound hydrogen isotope is ^3H according to the simplistic formula of Eq. (4.13), while controlled extrapolations from experimental mass measurements predict that ^7H should be bound by 6.58 MeV [4].

In Fig. 4.3, we have seen that at sufficiently high temperature, the last bound isotopes of light elements can become dominant in the composition of matter. It is therefore interesting to see how much our results depend on the poor energy description of light clusters of our mass formula. We have therefore repeated the same calculations, replacing the energy given by Eq. (4.13) with the experimental value of the binding energy, whenever this value is known [4].

In the inner crust, in fact, many nuclei populated with non-negligible probability in the different density and temperature conditions explored here are beyond the dripline. This means that their experimental binding energy is typically not known, hence Eq. (4.13) is still used for those nuclei in the new calculation. However experimental or extrapolated mass values exist for all bound isotopes of the lightest elements $Z \leq 3$, and in those cases the

experimental values are used.

We find that, in the range of temperatures considered, the results are similar to the ones presented in Fig 4.6 both for the highest (cells 1-2) and lowest (cells 7 to 10) densities. This means that the underbinding of light clusters does not influence the specific heat calculation. However, as shown

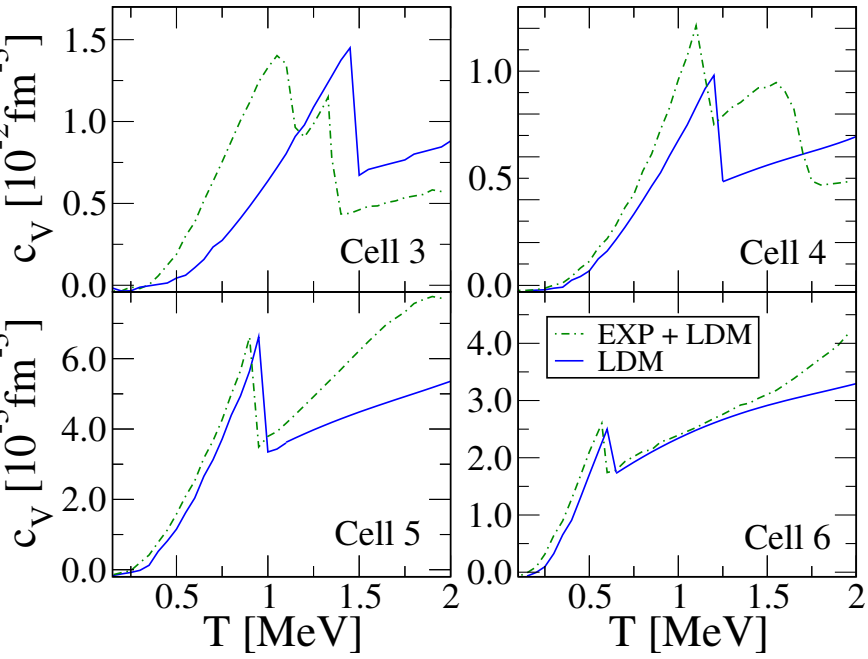

Figure 4.7: Temperature evolution of specific heat for four intermediate cells. Full lines: complete NSE calculation making use of the analytical expressions Eq. (4.13) for binding energies (labeled as LDM in the figure). Line with symbols: as the full line, but experimental binding energies, from [4], are used whenever available (EXP+LDM in the figure).

in Fig. 4.7, in the cells from 3 to 6 the situation is very different and the effect of accounting for the experimental binding energy of light clusters has a dramatic consequence. Indeed we see that the height of the specific heat peak and also its position in temperature are modified. Moreover, an extra peak appears, which was not present in the calculations of Fig. 4.6. This peak depends on the thermodynamical conditions of the cell and, as already anticipated, coincides with the temperature at which the nuclei melt into a gas of free particles and resonances. If resonances correspond to bound states, they will dominate over the standard nuclei component at much lower

temperatures than if they lie high in the continuum. The dominance of light clusters and resonances induces a change in the temperature dependence of the energy density, leading to an additional peak in the specific heat.

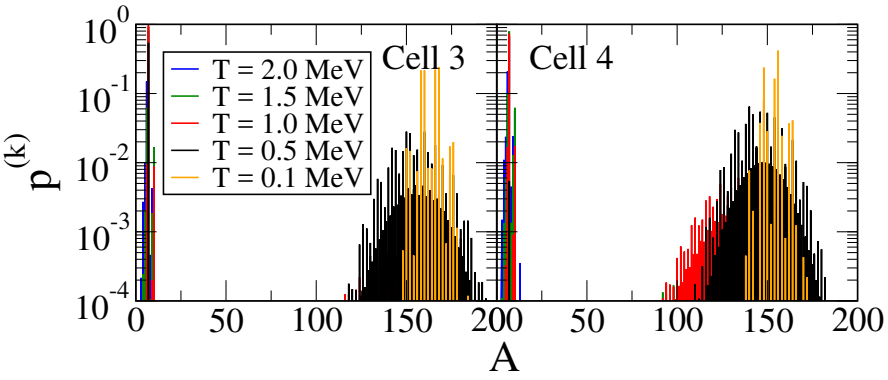

Figure 4.8: Normalized cluster size distribution at different temperatures, as obtained from complete NSE calculation using experimental binding energies from [4], whenever available. Results are shown for two representative cells where the transition to a dominance of light clusters is observed in the range of temperatures considered.

To better illustrate this point, Fig. 4.8 shows the cluster distribution obtained considering the experimental binding energies, whenever available, in the case of cells 3 and 4, where the second peak in the specific heat is observed. One can appreciate that the cluster distribution is quite different with respect to the results shown in Fig. 4.3. Moreover, we observe that the location of the second extended peak of the specific heat, shown in Fig. 4.7, exactly corresponds to the temperature where the cluster distribution starts to be dominated by light clusters. It should also be noticed that the same features could also appear in cells at lower densities, but at temperature values that are beyond the range considered in the present study.

4.3.4 Extended NSE model vs HFB calculation

Resorting to the experimental binding energies enhances therefore the light cluster dominance, which cannot be addressed by mean-field HFB calculations. Nevertheless, even employing the LDM functional parameterization of masses, the value of specific heat, as shown in Fig. 4.6, is different with

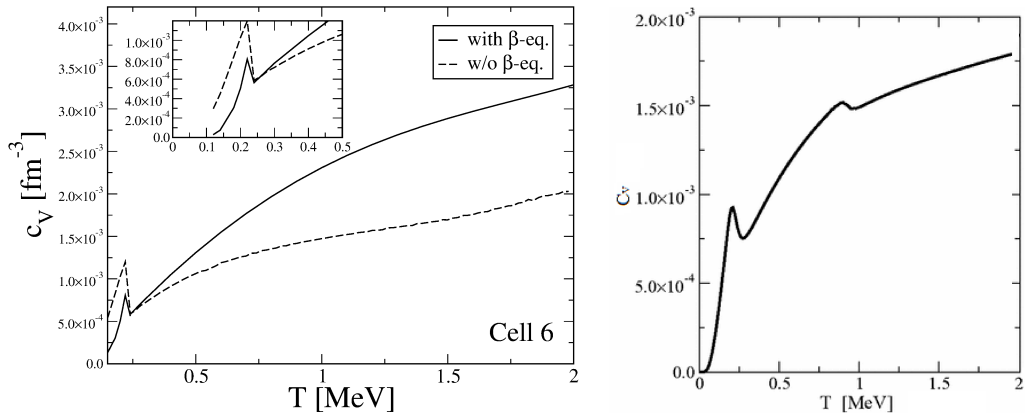

(a) Extended NSE model **(b)** HFB calculation

Figure 4.9: Temperature evolution of specific heat for Cell 6.
(a) Extended NSE model calculations obtained considering a pairing interaction with the same parameters of [72] and the analytical expressions Eq. (4.13) for binding energies. Full line: complete NSE calculation. Dashed line: as the full line, but the value of the global proton fraction is assumed equal to that one given in [72] (see also Table 4.1).
(b) HFB calculation of [72] (figure readapted).

respect to the results of previous HFB works [18, 45, 72, 137, 158] because of the different mean-field and/or pairing model, and because of the non-negligible effect of the cluster distribution that we have observed in Fig. 4.5. However, we have verified that the temperature location of the specific heat peak, its height and width are almost identical to the results of [72], if we take the same parameters for the pairing interaction employed in that work. This is illustrated in Fig. 4.9, where we represent the corresponding results for the specific heat, obtained imposing the β-equilibrium condition Eq. (3.3) or neglecting it (as in the HFB calculations). One can notice that the full curve compares rather well with the results of [72], but still the consideration of β-equilibrium induces non-negligible effects on c_V.

Although the transition temperature of the superfluid gas is correctly recovered, the peak is sharper than in the full HFB calculation. Moreover, in the latter case a second peak at higher temperature can appear, depending on the energy functional [72, 137]. This peak corresponds to the temperature at which the whole system becomes non-superfluid, according to the disap-

pearance of the pairing in the surface of the cluster. It has been proved in a recent HFB analysis [137] that this peak cannot be reproduced by simply decomposing the Wigner-Seitz cell into cluster and gas, accounting for the excluded volume effect. These observations show the importance to release the hypothesis of energy additivity adopted so far and, as we examine in the next section, to take into account the in-medium pairing corrections of the interface between cluster and gas.

4.4 In-medium effects to the cluster energy

The hypothesis that the bound part of the cluster and the gas contribution are additive, which leads to Eq. (4.24), neglects the modification of the cluster surface tension due to the presence of an external neutron gas. This residual in-medium modification of the cluster energy δE_{surf} can be computed by subtracting to the total energy in each Wigner-Seitz cell the contribution of the gas alone and of the nucleus alone, following [8]:

$$\delta E_{surf} = E_{tot} - E(A, \delta, \rho_p, T) - \left(V_{WS} - \frac{A}{\rho_0(\delta)} \right) \mathcal{E}_{HM}(\rho_g, \delta_g). \qquad (4.26)$$

Considering that this correction is expected to be a surface effect, it appears reasonable to compute it in the Local Density Approximation (LDA).

Actually, these in-medium corrections were evaluated in [8] adding to the LDA also higher orders in $\hbar$ in the semi-classical Thomas-Fermi development of the energy functional, but neglecting the pairing interaction and the temperature dependence. It was shown that δE_{surf} is indeed a surface term $\propto A^{2/3}$, but it displays a very complex behavior with the cluster bulk asymmetry δ, the gas density ρ_g and the gas asymmetry δ_g. In our work therefore we include the effect of the temperature and of the pairing gap according to Eq. (3.16), but we limit ourselves to the simple LDA. Gradient and spin-orbit terms are thus neglected in the surface correction.

4.4.1 Local Density Approximation (LDA)

In order to evaluate the in-medium surface correction in LDA a model for the density profiles has to be assumed. We use the simple Wood-Saxon analytical profiles proposed in [135] and successfully compared to full Hartree-Fock calculations in spherical symmetry [8, 135]:

$$\begin{aligned}\rho(r) &\equiv \frac{\rho_0 - \rho_g}{1+\exp(r-R)/a} + \rho_g, \\ \rho_p(r) &\equiv \frac{\rho_{0p} - \rho_{gp}}{1+\exp(r-R_p)/a_p} + \rho_{gp},\end{aligned} \tag{4.27}$$

such that the local asymmetry is given by $\delta(r) = 1-2\rho_p(r)/\rho(r)$. The radius parameters R and R_p entering the density profile Eq. (4.27) are related to the equivalent hard sphere R_{cl} radius by

$$R = R_{cl}\left[1 - \frac{\pi^2}{3}\left(\frac{a}{R_{cl}}\right)^2\right], \tag{4.28}$$

and a similar relation holds for R_p. The diffuseness parameters a and a_p of the total density profile are assumed to depend quadratically on the bulk asymmetry δ, $a_i = \alpha_i + \beta_i\delta^2$, where α_i and β_i were fitted from HF calculations in [135].

Using the two quantities defined in Eq. (4.27), the in-medium surface correction can be finally expressed as

$$\delta E_{surf}^{LDA} = 4\pi \int_0^{R_{WS}} dr r^2 \left[\mathcal{E}_{HM}(\rho(r),\delta(r)) - \mathcal{E}_{HM}(\rho_{cl}(r),\delta_{cl}(r))\right] - \mathcal{E}_{HM} x_g V_{WS}, \tag{4.29}$$

where $\delta_{cl}(r) = 1-2\rho_{p,cl}(r)/\rho_{cl}(r)$, with $\rho_{cl}(r)$ and $\rho_{p,cl}(r)$ the total and proton densities, respectively, as defined in Eq. (4.27) but evaluated in absence of the gas and corresponding to the same (A,δ) cluster, and R_{WS} is the radius of the Wigner-Seitz cell.

For the low temperatures which are of interest in our study, the in-medium surface energy correction computed here is expected to give a small effect to the composition of the inner crust [147]. The effect of the in-medium

correction will therefore be estimated perturbatively. We assume that, for a given thermodynamic condition (ρ_B, y_p, T), the in-medium surface correction $\delta E_{surf}(A, \delta, \rho_g, \delta_g)$ affects only slightly the gas density and composition, and consequently the chemical potentials. This correction will then be taken using the values for ρ_g, δ_g obtained from a NSE calculation where the in-medium effects are not considered. With this assumption, the modified binding energies solely depend on the cluster and on the thermodynamic condition and can therefore be simply added a-posteriori to the energy density.

The final expression for the total baryonic energy density at finite temperature is then given by:

$$\mathcal{E}_{tot} = \mathcal{E}_g + \frac{1}{< V_{WS} >} \sum_k p^{(k)} [\langle E(A^{(k)}, \delta^{(k)}) \rangle + \delta E_s(A^{(k)}, \delta^{(k)})], \qquad (4.30)$$

where all terms depend on the temperature, and on the gas density and composition.

4.4.2 Surface corrections on the specific heat

The effects of the surface corrections, as described above, are evidenced in Fig. 4.10. In the calculation illustrated by dashed lines, the total energy is simply given by the sum of the cluster and uniform gas components according to Eq. (4.24), as suggested in early papers [112, 143]. The energy contribution of the cluster-gas interface, according to Eq. (4.30), is shown by full lines. One observes a small, though appreciable, effect of the in-medium corrections on the specific heat. In particular, we notice that, in the calculations neglecting the surface effects (dashed line), the transition temperature from superfluid to normal matter is more sharply defined. This is due to the fact that the gas density is characterized by a single value at each temperature point. Our procedure to introduce surface corrections can partially cure this problem and leads , as expected and as it is observed in HFB calculations [72], to a smoothed peak at the transition temperature. Moreover a third small peak appears, at least in Cell 3 and at $T \approx 1.8$ MeV, due to the disappearance of pairing effects on the surface of the clusters, as

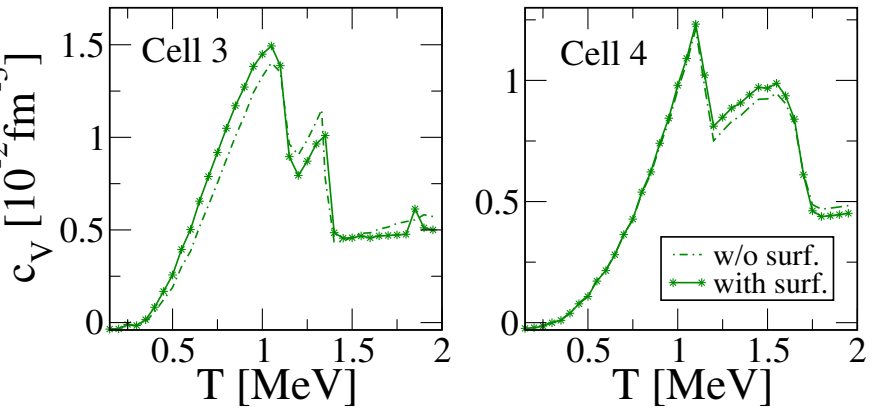

Figure 4.10: Temperature evolution of specific heat for the same two cells as in Fig. 4.8. Full line with symbols: complete NSE calculation using experimental binding energies, from [4], whenever available. Dashed line: as the full line but neglecting in-medium effects.

observed again in the temperature evolution of the specific heat evaluated by HFB models (see Fig. 4.9, panel (b)). To conclude, we argue that the effect of density fluctuations is not generally negligible, even if it represents just a correction of the total energy density, thus globally justifying the perturbative treatment developed so far.

However, a few words of caution are in order. Contrary to bulk in-medium effects of Eq. (4.8) which increase systematically the binding energy of the cluster, surface interaction with the surrounding gas is strongly dependent on the cluster asymmetry, as well as on the density and proton fraction of the gas. Surface in-medium shifts for very neutron rich species immersed in a neutron gas tend in particular to decrease the binding energy of the cluster [147]; it is therefore possible that a self-consistent inclusion of this energy term in the statistical calculation will reduce the contribution of the light resonances, especially when experimental masses are employed.

Moreover, our local density BCS approximation to evaluate the pairing contribution of an inhomogeneous density distribution, including the population of light resonances, is certainly a quite crude approximation. Indeed, the Local Density Approximation (LDA) so far adopted has been already compared to HFB calculations in the case of trapped fermionic atoms in [84] and it has been shown that even if it nicely works in small systems at zero

temperature, it rapidly deteriorates at finite temperature. In particular the LDA pairing field is seen to show a sudden drop at the surface, which is not apparent in the full HFB. We however expect this limitation of LDA to be less severe in our case because, contrarily to [84], we do not use the LDA to solve the variational problem, but only to calculate the energy correction. Moreover our physical system is obviously not the same as in [84]. We have verified that in our Wigner-Seitz cells the radial profile of the pairing field does not drop off but presents a decreasing tail, similar to HFB results.

Anyway, further corrections could be introduced in the case of very neutron rich species immersed in a neutron gas [147] and are currently under study.

4.5 Total specific heat of the crust matter

In the previous section, we have concentrated on the baryonic specific heat of the nonuniform inner-crust matter.

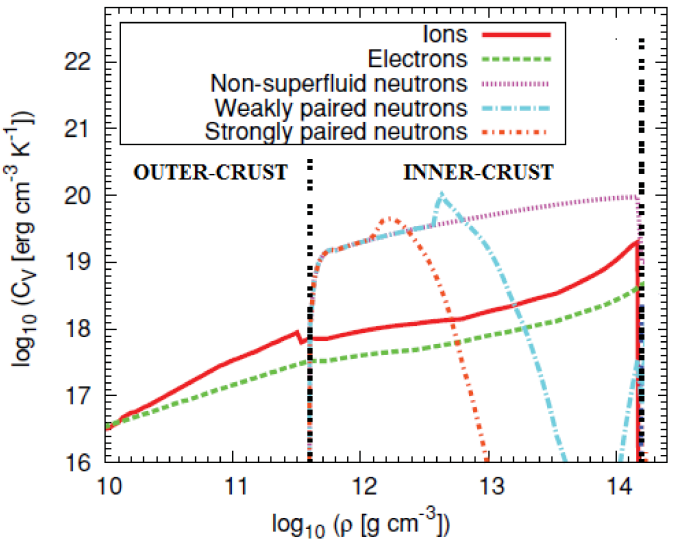

Figure 4.11: Specific heat for the different components of the neutron star matter, as obtained in HFB calculations for a temperature of 10^9 K $\approx$ 86 keV. Readapted from [72].

However, in order to get the total c_V of the inner part and also to extend the analysis to the whole crust matter, one should include also the contribution of the other components of the crust itself.

In Fig. 4.11, one can observe for example an estimation of the density dependence of the specific heat for the different components of the star matter, as obtained in [72] and at a tempera-

ture close to the lowest one considered in our study (100 keV). If the unbound neutrons were not superfluid, their contribution to the specific heat will dominate in the inner crust, at least at the temperatures of interest for the cooling of the neutron star. However, since neutrons are extensively paired, as it has been shown in the previous sections, in the superfluid regime the specific heat for the gas comes to be strongly suppressed, so that the relative contribution of ions and electrons is enhanced. Moreover, beyond the drip point, that is in the outer crust, these two contributions are the only relevant ones, so they should be taken into account for a reliable calculation of the cooling curve.

In our work, we have also underlined the importance of the temperature evolution of the β-equilibrium condition. We show here that a proper treatment of the modification with the temperature of the proton fraction could affect at moderate T-values not only the baryonic term of the specific heat, but also the electronic one.

4.5.1 Contribution of the electron plasma

In the neutron star crust, the electrons form an ultra-relativistic highly degenerate Fermi gas and their contribution to the heat capacity per unit volume is simply given by [144]

$$c_{V,e} = \frac{1}{3}\left(3\pi^2 \rho y_p\right)^{2/3} T, \tag{4.31}$$

where the proton fraction y_p should be determined consistently along a β-equilibrium trajectory of the matter. The temperature evolution of the electronic specific heat $c_{V,e}$, as given by the Eq. (4.31), making use of the temperature dependent proton fraction evaluated within the extended NSE model, is illustrated in Fig. 4.12, for four representative values of the total baryonic density of the inner-crust matter.

The effect of β-equilibrium appears pronounced again especially in the external layers of the inner crust and goes in the opposite direction observed for the baryonic term (see Fig. 4.6). However, the two contributions do not cancel each other, because the modification of the electron term is rather

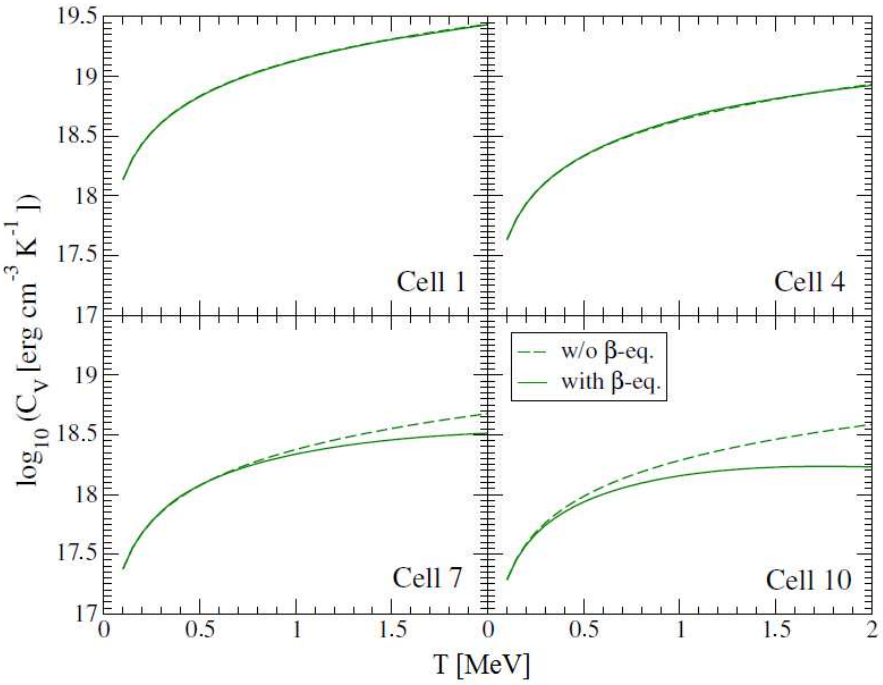

Figure 4.12: Temperature evolution of the electronic specific heat for the same representative cells as in Fig. 4.1. Full line: complete NSE calculation. Dashed line: as the full line, but the value of the global proton fraction is assumed equal to that one calculated from β-equilibrium at the lowest temperature, $y_p(T) = y_p(0.1\text{MeV})$.

small.

4.5.2 Thermal evolution of the outer crust

More recently, our attention has been directed also to the thermalization of the proto-neutron star outer crust. In these layers, the specific heat has contributions from the electrons and the ions (see Fig. 4.11). While, making use of Eq. (4.31), it is easy to get the electron contribution, the evaluation of the ion term is not trivial. The thermodynamic state of the ions goes from liquid to solid as the star cools down, and in the solid state from a classical to a quantal crystal [144]. The simplest model for the electron-ion plasmas is the one component plasma (OCP), where each ion thermodynamic state is determined, for each Wigner Seitz cell k, only by Coulomb coupling

parameter:

$$\Gamma_C = \frac{(Ze)^2}{R_{WS}T}. \tag{4.32}$$

Monte-Carlo simulations in OCP approximation show that crystallization occurs at $\Gamma_C > \Gamma_m \approx 175$ [72, 144]. The specific heat per ion increases from the ideal-gas value, $c_V^{(k)} = \frac{3}{2}$ at $T \gg T_m$ to the Dulong-Petit law for a classical harmonic crystal value $c_V^{(k)} = 3$ at $T \lesssim T_m$. With further cooling, quantum effects suppress the specific heat and into the deep quantum regime its value will be given by the Debye result:

$$c_V^{k(D)} = \frac{12\pi^4}{5}\left(\frac{T}{\Theta_D}\right)^3, \tag{4.33}$$

where Θ_D is the Debye temperature. Work is in progress to include these corrections in our model.

As a final remark, we would like to mention another improvement that we are going to implement in the extended version of the NSE model described so far.

In the outer crust of the neutron star shell effects, which are not included in the LDM functional here adopted, are known to play a non-negligible role. However, the parameterization EXP+LDM, which substitutes the value given by the functional with the experimental mass of the nuclear cluster whenever it is available, could lead to discontinuities in the treatment of ordinary and beyond dripline nuclei. Therefore, we are trying to use some Skyrme models which require additional parameters and could significantly improve the matching between the two different parameterizations of the masses. In particular, we are adopting the BSk functionals [82], which have been recently proposed by the Bruxelles group and are specifically optimized to astrophysical applications.

This work is expected to provide a more accurate estimation of the crust thermalization time of proto-neutron stars.

Chapter 5

Structure and small amplitude dynamics in neutron-rich nuclei

Neutron-rich nuclei, as stressed in Chapter 3 and 4, play a crucial role in nuclear astrophysics as well as for constraining the nuclear energy density functional. In particular, the isovector term of the nuclear effective interaction is widely studied not only in the modelization of the compact stellar objects, but also in nuclear reactions, according to the possibilities offered by the new radioactive beam facilities which allow to investigate several properties connected with the isospin degree of freedom.

From these studies, it has emerged that neutron-rich nuclei exhibit some fascinating properties which make them different from ordinary nuclei. For instance, neutron-rich nuclei are characterized by new kinds of collective motion which are absent in those without neutron excess [130, 182].

Therefore hereafter we are going to explore the nuclear structure and the collective phenomena emerging in the small amplitude dynamics of nuclei. Actually, to make a bridge with the previous chapters, in the first part we investigate the collective modes in asymmetric nuclear matter. This analysis should lead in fact to a better understanding of the dipole response of neutron-rich nuclei, which is initially addressed within a semi-classical transport model employing some new Skyrme effective interactions for the nuclear mean field [202] (see Chapter 1), in order to evidence the isoscalar-isovector

mixing of the collective excitations developing in such systems. The second part is dedicated to the comparison of these semi-classical results with quantal calculations; both these investigations are going to connect the characteristics of nuclei to the low density behavior of the symmetry energy. Finally, the Canonical basis extension of the TDHF theory should allow one to evaluate also the effect of pairing correlations on the properties of the dipole modes.

5.1 New Skyrme interactions: SAMi-J

In all numerical calculations of this chapter, for the mean-field representation, we employ the recently introduced SAMi-J Skyrme effective interactions which have been fitted according to the SAMi protocol [151]:

- binding energies and charge radii of some doubly magic nuclei to predict reasonable saturation properties of symmetric nuclear matter ($\rho_0 = 0.159$ fm^{-3}, energy per nucleon E/A = -15.9 MeV and incompressibility $K = 245$ MeV);
- some selected spin-orbit splittings;
- spin and spin-isospin sensitive Landau-Migdal parameters [38];
- neutron matter EoS of [198].

These features allow the new SAMi interactions to give a reasonable description of spin-isospin resonances, keeping a good reproduction of well known empirical data such as masses, radii and important nuclear excitations. The main difference between SAMi and the SAMi-J family is that the latter has been produced by systematically varying the value of J = $C(\rho_0)$ from 27 to 35 MeV, keeping fixed the optimal value of the incompressibility and effective mass predicted by SAMi and fitting again the parameters for each value of J. This produces a set of interactions of similar quality on the isoscalar channel and that, approximately, isolates the effects of modifying the isovector channel in the study of a given observable. In our calculations, we employed,

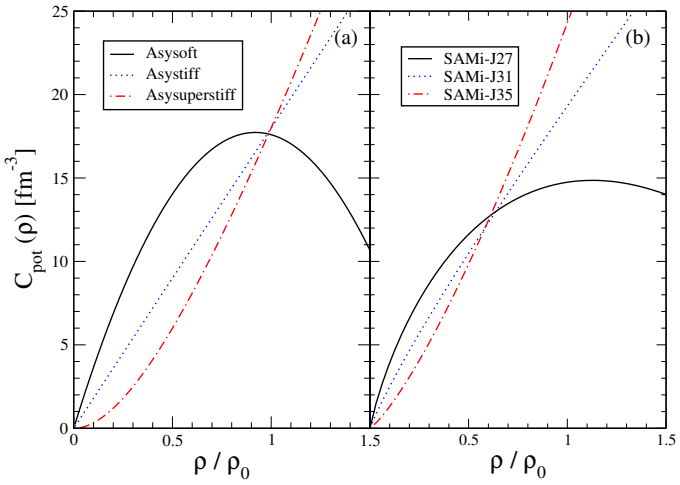

Figure 5.1: Density dependence of the potential part of the symmetry energy for three SAMi-J Skyrme parameterizations and some momentum independent interactions with similar behavior at density saturation ρ_0.

in particular, three SAMi-J parameterizations: SAMi-J27, SAMi-J31, and SAMi-J35 [151], whose density behavior of $C_{pot}(\rho)$ (see Fig. 1.2) is illustrated in Fig. 5.1, panel (b). Since, as mentioned above, the SAMi-J interactions have been fitted in order to also reproduce the main features of finite nuclei, for the three parameterizations the symmetry energy coefficient gets the same value, $\frac{E_{sym}}{A}(\rho_c) \approx 22$ MeV at $\rho_c = 0.65\rho_0$, which can be taken as the average density of medium-size nuclei. Thus the curves representing the density dependence of $C_{pot}(\rho)$ cross each other at $\rho = \rho_c$, i.e., below saturation density, contrarily to the other simplified Skyrme parameterizations (see for example Fig. 5.1, panel (a)).

5.2 Collective modes in asymmetric matter

In the astrophysical applications of Chapter 3, within the general framework of thermodynamics, we discussed the equilibrium properties of the asymmetric nuclear matter. In order to address the elementary (resonant) excitations of nuclear systems, we are going to review now the linear response mean-field methods adopted to describe the collective modes [142], which are modes physically involving a coherent motion of many particles of the system,so that the individual constituents loose their meaning.

To make the connection with thermodynamics, we first consider the col-

lective modes in the bulk matter, where the density fluctuations generally propagate and form sound waves [47]. Since nucleons are fermions, the density fluctuations should be investigated in Landau's fluid theory, but for comparison, before embarking on the specific description of Fermi liquids, we recall the hydrodynamical approach usually adopted to describe the behavior of a classical fluid.

5.2.1 Hydrodynamical theory for bulk matter

The dynamics of a classical fluid is dominated by (quasi-)particle binary collisions [142]. In this regime, the solution of the Boltzmann-Nordheim-Vlasov transport equation Eq. (1.52) is then completely determined by the pressure P, which accounts for the contribution of the mean-field, and by the collision integral I_c so that ordinary hydrodynamic waves are possible. Under these circumstances, by denoting with $\mathbf{v}$ the velocity field, the dynamics of density fluctuations can be described by the Eulero equations:

$$\begin{aligned} \frac{d(\rho\mathbf{v})}{dt} &= \frac{\partial(\rho\mathbf{v})}{\partial t} + \mathbf{v}\cdot\nabla(\rho\mathbf{v}) = -\frac{1}{m}\nabla P \\ \frac{\partial\rho}{\partial t} &= -\nabla\cdot(\rho\mathbf{v}). \end{aligned} \tag{5.1}$$

These equations can be linearized around an uniform initial density $\bar{\rho}$ by considering the small amplitude fluctuation $\delta\rho = \rho(\mathbf{r},t) - \bar{\rho}$, leading to the following relations:

$$\begin{aligned} \bar{\rho}\frac{d\mathbf{v}}{dt} &= -\frac{1}{m}\nabla P \\ \frac{\partial\delta\rho}{\partial t} &= -\bar{\rho}\nabla\cdot\mathbf{v}, \end{aligned} \tag{5.2}$$

which can be combined to yield

$$\frac{\partial^2\delta\rho}{\partial t^2} = \frac{1}{m}\nabla^2 P \approx \frac{1}{m}\left(\frac{\partial P}{\partial\rho}\right)\Big|_{\rho=\bar{\rho}}\nabla^2\delta\rho, \tag{5.3}$$

where the linearization of the pressure has been taken into account.

Performing the Fourier transform and exploiting the thermodynamical relation between pressure and chemical potential derivatives with respect to the density

$$\frac{\partial P}{\partial \rho} = \rho \frac{\partial \mu}{\partial \rho}, \tag{5.4}$$

one finally gets the following dispersion relation

$$\omega_k^2 = \left(\frac{\rho}{m} \frac{\partial \mu}{\partial \rho} \right) k^2 \equiv v_s^2 k^2, \tag{5.5}$$

where ω_k and $\mathbf{k}$ denote the frequency and the wave number, respectively, of the perturbation considered and the speed of sound v_s has been introduced. The latter expression brings out the connection existing between sound waves and thermodynamics [47]. The development introduced above can be easily generalized to two-component systems and therefore we are going to apply it to the asymmetric nuclear matter (ANM) case.

However, in the two-dimensional framework of ANM, in place of the chemical potential derivative in Eq. (5.5), one should consider the two eigenvalues (isoscalar λ_S and isovector λ_V, respectively) of the curvature matrix defined in Eq. (1.61), in order to get the corresponding dispersion relations. We remind that these two eigenvalues correspond to the normal modes of oscillation of the system in the space of density fluctuations and completely characterize the thermodynamical stability of the system itself. In Chapter 1, it has been also stressed that the two modes are fully decoupled only in the case of symmetric nuclear matter (SNM), whereas in ANM a coupling is introduced in the linearized equations and, as a consequence, the two nucleonic species oscillate with different amplitudes.

The square phase velocities ω_k/k of both modes are illustrated in Fig. 5.2, in case of symmetric nuclear matter ($I = 0$) and for density fluctuations of infinite wavelength ($k = 0$), as a function of the density. One observes that, as it is expected, the isoscalar mode (top panel) reproduces the density behavior of the nuclear matter incompressibility K, while the isovector one (bottom panel) is ruled by the symmetry term (see Fig. 5.1). Within the density region characterized by positive values of the compressibility, known in literature

as first sound regime, the isoscalar density fluctuations propagate. However, whereas the square frequency of the isovectore mode is always positive, there is a density region where the corresponding quantity for the isoscalar mode becomes negative. This region, characterized by a negative value of the compressibility, is nothing but the spinodal region addressed in Chapter 1 and 2. Then, the corresponding speed of sound comes out to be imaginary and the system is unstable against density undulations.

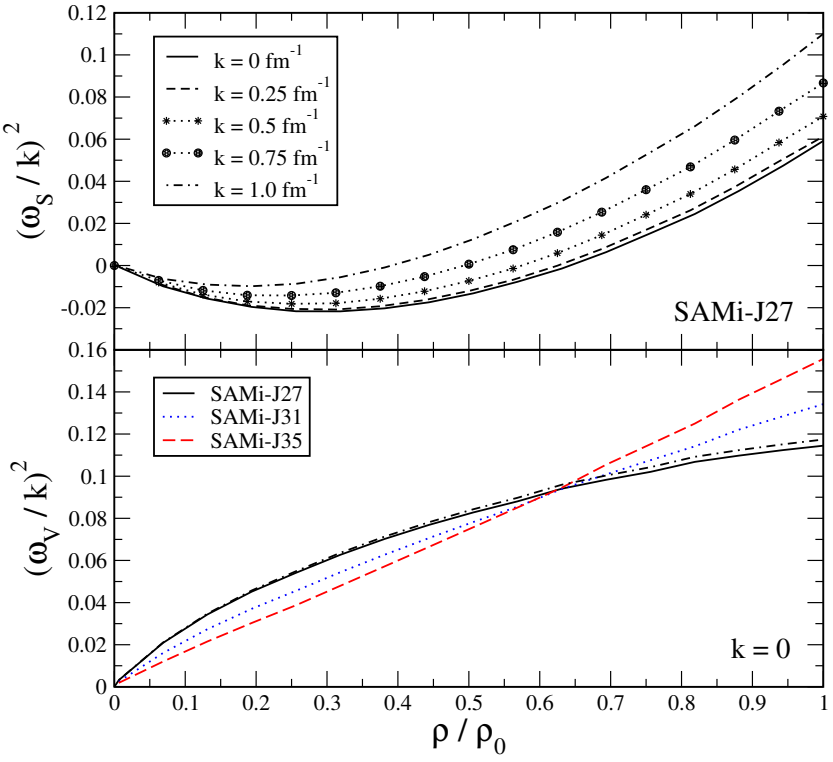

Figure 5.2: Top panel: square of the phase velocity for the isoscalar mode as determined in symmetric nuclear matter (SNM), for SAMi-J27 parameterization and for several k-values, as a function of the reduced density $\tilde{\rho} = \rho/\rho_0$. Bottom panel: the same as in the top panel, but for the isovector mode, for $k = 0$ and three SAMi-J parameterizations of the effective interaction here considered. The dashed-dotted line illustrates, for SAMi-J27 interaction, also the result at finite k.

The top panel of Fig. 5.2 illustrates, for the SAMi-J27 parameterization, the density behavior of the isoscalar mode also for finite-size density fluctuations. The analysis at finite k-values allows one to appreciate the modification introduced by the surface terms of the effective interaction, which increase

the frequency of the mode. Actually, the surface term slightly affects also the isovector mode, as one can deduce looking at the dashed-dotted curve in the bottom panel of Fig. 5.2. The latter variation is however small and its sign depends on the parameterization of the effective interaction adopted.

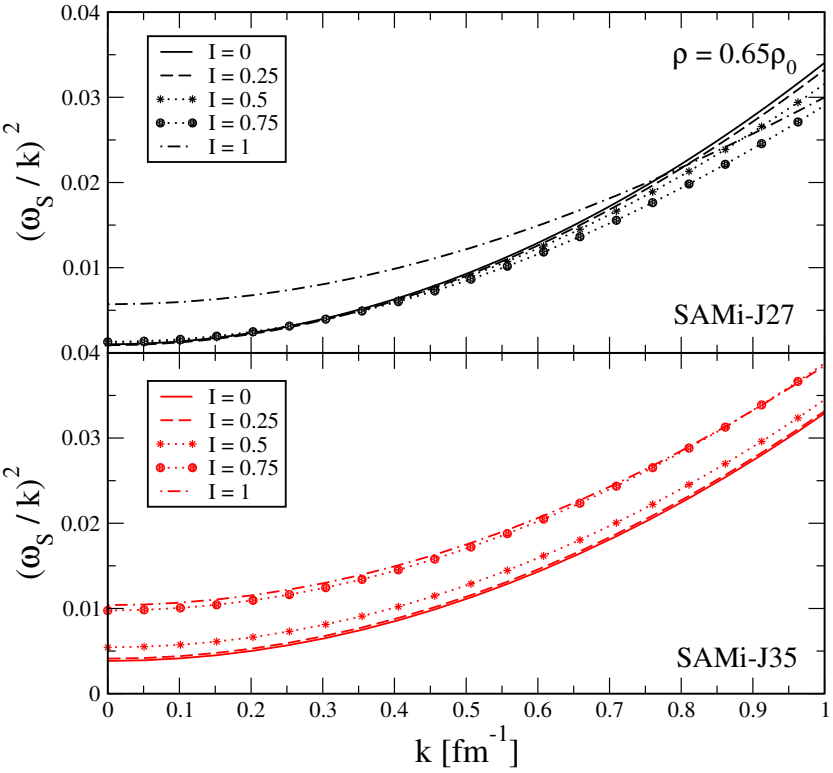

Figure 5.3: Top panel: square phase velocity for the isoscalar-like mode as determined at the crossing density ρ_c, for SAMi-J27 parameterization and for several asymmetry values, as a function of the wave number k. Bottom panel: the same as in the top panel, but for SAMi-J35 interaction.

The effect of the surface contributions on the isoscalar-like mode is shown also in Fig. 5.3, where its square phase velocity, as obtained at the density crossing ρ_c, for SAMi-J27 (top panel) and SAMi-J35 (bottom panel), is plotted as a function of k, for several asymmetry values I. Quite interestingly, it emerges that the symmetry energy and its slope, which rule mostly the behavior of the isovector mode, influence also the compressibility of the matter, leading to a larger frequency (at small k values) for ANM. However, this effect reduces at larger k values, since as observed also in Fig. 5.2, the isovec-

tor finite term D_{fin} defined in Eq. (1.38) is smaller than the corresponding isoscalar surface contribution C_{fin}. This explains the trend shown in Fig. 5.3, especially in case of SAMi-J27 parameterization, where, for large values of the wave number, the square phase velocity becomes smaller for matter with a stronger neutron excess.

It should be noted however that the fermionic nature of the nucleons reflects in a more complex scenario with respect to the one depicted here. The exclusion Pauli principle in fact guarantees that at low temperature collisions between thermally excited particles play a negligible role, questioning therefore the applicability of the results deduced in the hydrodynamical approach.

5.2.2 Linearized Vlasov equations: semi-classical RPA

The propagation of density waves in Fermi liquids has been considered already long time ago by Landau [108]. For a fermionic system at zero temperature the Pauli-blocking strongly suppresses collisions, thus reinforcing the role of the mean field, and reduces the number of active particles to those near the Fermi surface, hence affecting the propagation of waves [47]. At finite temperature, on the contrary, several collisions act to disrupt the collective motion and hence to damp the waves [142].

In order to obtain the dispersion relation of the collective modes in asymmetric nuclear matter, one should consider therefore the opposite (collisionless) regime, thus applying the linear response analysis to the Vlasov equation Eq. (1.50), where the residual collisions I_c in Eq. (1.52) are entirely neglected. This is the so-called zero sound regime.

Let us consider a small amplitude perturbation δf_q of the distribution function f_q of each nucleonic species, that is

$$f_q \approx f_q^0 + \delta f_q \qquad q = n, p, \tag{5.6}$$

then the linearized Vlasov equation, for any nucleonic species q assumes this form:

$$\frac{\partial(\delta f_q)}{\partial t} + \nabla_{\mathbf{r}}(\delta f_q) \cdot \nabla_{\mathbf{p}} \epsilon_q^0 - \nabla_{\mathbf{p}} f_q^0 \cdot \nabla_{\mathbf{r}}(\delta \epsilon_q) = 0, \tag{5.7}$$

where a modification has been introduced with respect to Eq. (1.50) also to take into account the momentum dependence of the effective interaction. The derivations of the single particle energy ϵ_q, already defined in Eq. (1.32), and of its fluctuation $\delta\epsilon_q$ are detailed in section A.5. In deriving the Eq. (5.7), it is taken into account that, considering a space-uniform distribution function at equilibrium f_q^0 and in the case of homogeneous nuclear matter, one obtains $\nabla_{\mathbf{r}} f_q^0 = \nabla_{\mathbf{r}} \epsilon_q^0 = 0$.

We are interested in particular in plane-wave solutions δf_q, periodic in time with frequency ω_k and wave number $\mathbf{k}$ such as:

$$\delta f_q(\mathbf{r}, \mathbf{p}, t) \sim \sum_{\mathbf{k}} \delta f_q^{\mathbf{k}} \, e^{i(\mathbf{k}\cdot\mathbf{r} + \omega_k t)}. \tag{5.8}$$

Under this assumption, it is possible to demonstrate (see section A.6) that the two coupled Vlasov equations lead to the following dispersion relations:

$$\begin{aligned} c_0 \alpha_q^0 &= -\sum_{l=0,1} c_l \, s_q^l \, \chi_q \sum_{q'=n,p} \alpha_{q'}^l L_{l\,qq'} \\ c_1 \alpha_q^1 &= -\sum_{l=0,1} c_l \, s_q^{l+1} \, \chi_q \sum_{q'=n,p} \alpha_{q'}^l L_{l\,qq'} - c_1 \gamma, \end{aligned} \tag{5.9}$$

where α_q^l are the coefficients of the l-expansion of δf_q in terms of Legendre polynomials, $L_{l\,qq'}$ the usual Landau parameters and γ is related to $L_{1\,qq'}$ by

$$\gamma = \frac{1}{3} \sum_{q'=n,p} \alpha_{q'}^1 L_{1\,qq'}. \tag{5.10}$$

Moreover, s_q denotes the (dimensionless) zero sound velocity v_s in units of the Fermi velocity modified by the effective mass, v_{Fq}^*, that is:

$$s_q \equiv \frac{v_s}{v_{Fq}^*} = \frac{\omega_k}{k v_{Fq}^*}, \tag{5.11}$$

$\chi(s_q)$ is the Lindhard function defined as

$$\chi(s_q) \equiv 1 - \frac{s_q}{2} \ln\left(\frac{s_q + 1}{s_q - 1}\right), \tag{5.12}$$

and lastly, $c_0 = -1$ and $c_1 = \frac{\sqrt{3}}{3}$. The equations in Eq. (5.9) are equivalent to the linear and homogeneous system $\mathbf{A}\alpha = 0$, where the matrix $\mathbf{A}$ is:

$$\mathbf{A} = \begin{pmatrix} c_0(1+L^0_{nn}\chi_n) & c_0 L^0_{np}\chi_n & c_1 L^1_{nn} s_n \chi_n & c_1 L^1_{np} s_n \chi_n \\ c_0 L^0_{pn}\chi_p & c_0(1+L^0_{pp}\chi_p) & c_1 L^1_{pn} s_p \chi_p & c_1 L^1_{pp} s_p \chi_p \\ c_0 L^0_{nn} s_n \chi_n & c_0 L^0_{np} s_n \chi_n & c_1\left[1+L^1_{nn}\left(\frac{1}{3}+s_n^2\chi_n\right)\right] & c_1 L^1_{np}\left(\frac{1}{3}+s_n^2\chi_n\right) \\ c_0 L^0_{pn} s_p \chi_p & c_0 L^0_{pp} s_p \chi_p & c_1 L^1_{pn}\left(\frac{1}{3}+s_p^2\chi_p\right) & c_1\left[1+L^1_{pp}\left(\frac{1}{3}+s_p^2\chi_p\right)\right] \end{pmatrix}$$

while $\alpha = (\alpha^0_n, \alpha^0_p, \alpha^1_n, \alpha^1_p)$. Since we are looking for nontrivial α solutions of this system, one must impose that the determinant of $\mathbf{A}$ vanishes.

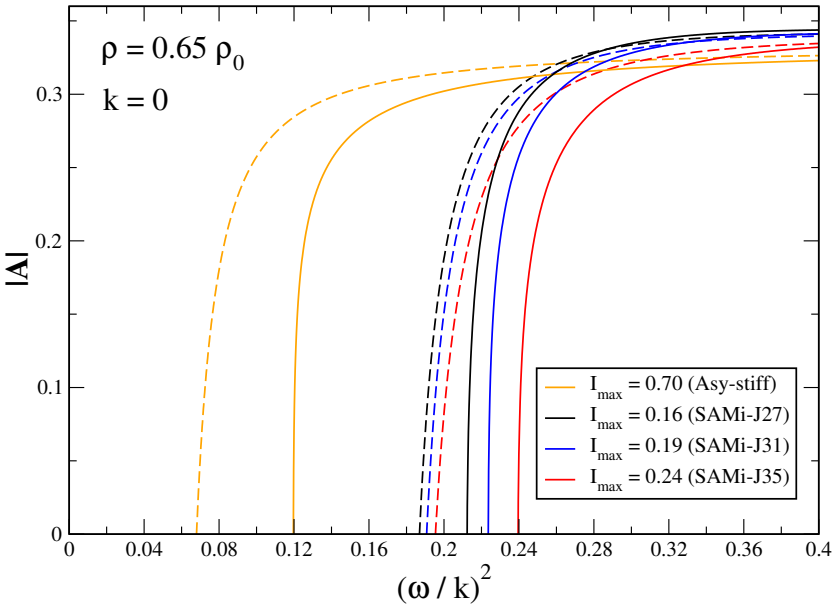

Figure 5.4: Dependence of the determinant of $\mathbf{A}$ (see text) on the phase velocity of the collective mode, for asystiff and SAMi-J parameterizations, $k = 0$ and symmetric nuclear matter (dashed lines). The full lines are instead evaluated at the maximum value of the asymmetry compatible with at least one ω/k value which allows the determinant to vanish.

In such a framework, therefore, the eigenfrequencies of the system correspond to the ω_k/k values matching zeros of the determinant. Our searching for the solution is illustrated in Fig. 5.4, for the three SAMi-J parameterizations previously considered, at the density ρ_c and for $k = 0$. The dashed lines are related to the SNM case and clearly manifest the dependence of the result

on the slope of the symmetry energy. The three curve are however quite close each other since, as already stressed, the SAMi-J parameterizations cross at ρ_c. The full curves are instead evaluated at the maximum value of the asymmetry I_{max} which allows one to find a solution. For higher asymmetry, the single particle motion prevails and the collective motion looses its meaning. One can observe that, for the SAMi-J parameterizations, the more robust is the mode in case of SNM, the higher is the I_{max} value up to which the mode resists.

The comparison with the orange curves puts in evidence the effect of the momentum dependence. We can see that, accounting for the effective mass and for the momentum dependent contributions, leads to a significant displacement of the solution towards higher values of the eigenfrequencies. On the other hand, however, the momentum dependence seems to reduce the range of asymmetry values where one can finds the solution.

The phase velocities corresponding to zero determinant are also plotted in the top panels of Fig. 5.5, as a function of the asymmetry I, for several ρ values and for SAMi-J27 (left panel) and SAMi-J35 (right panel), respectively. The solutions obtained by solving the linearized Vlasov equations at $I = 0$ appear close to those deduced by the hydrodynamical approach, when the isovector mode is considered (see Fig. 5.2, bottom panel). These figures also reveal, as in the hydrodynamical case, how the frequency associated to the collective mode behaves like the symmetry term $C_{pot}(\rho)$, which is always an increasing function of ρ, in the density range considered. Moreover, it clearly emerges how the robustness of the collective mode and so the value of I_{max}, for each ρ value, depends on the evaluation of the symmetry energy at that density. As a consequence, one observes an opposite trend in the behavior with the asymmetry I, for the two effective interactions, when considering density values which lie below or above the density of the crossing ρ_c.

Looking at the ratio $\frac{\delta\rho_n}{\delta\rho_p}$, one gets also the characterization of the nature of these modes, as it is displayed in the bottom panels of Fig. 5.5. Concerning the results for SNM (I=0), one evidently deduces that these eigenfrequencies correspond to purely isovector modes. Furthermore, owing to the isospin

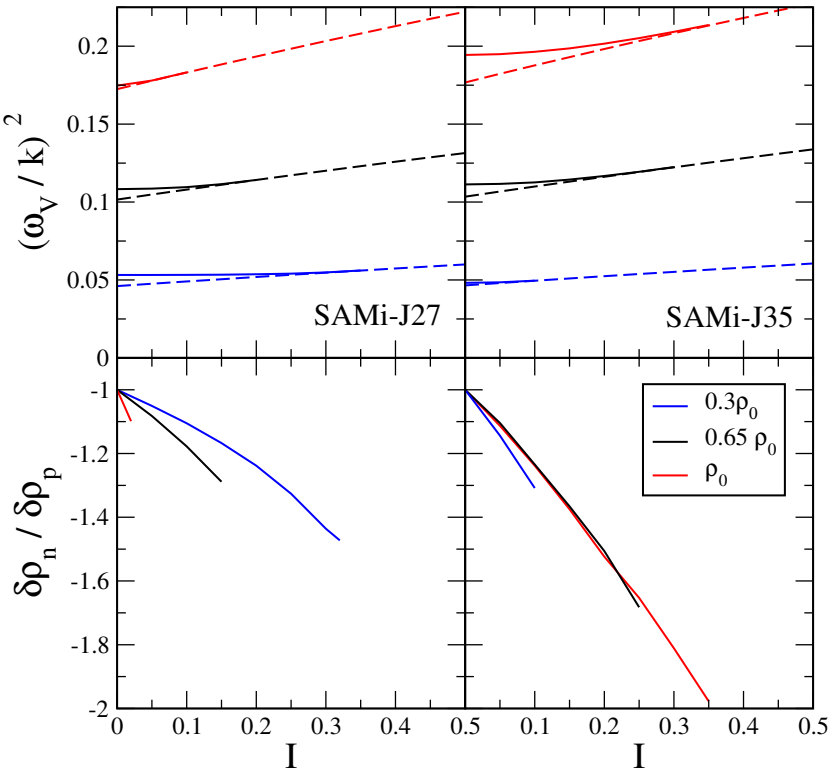

Figure 5.5: Top panels: Square phase velocity of the isovector-like mode (solid lines) and square neutron Fermi velocity (dashed lines), as functions of the asymmetry I, as obtained by solving the linearized Vlasov equations, for several density values. Bottom panels: Ratio between neutron and proton density fluctuations as a function of the asymmetry I, for the same density values as in the top panels. Left panels represent results for SAMi-J27 parameterization, right panels for the SAMi-J35 one.

asymmetry exhibited by the matter, the absolute value of the ratio between neutron and proton density fluctuations becomes larger when increasing the neutron excess. However, this ratio, as it has been widely discussed in section 2.6.1, is mainly ruled by the density behavior of the slope of the symmetry energy. In particular, the higher is the value of the slope, the closer to one is the ratio between the density fluctuations, according to the larger degree of mixing with the isoscalar-like mode [13].

Actually, by solving the linearized Vlasov equations with the SAMi-J parameterizations, one determines only the isovector-like eigenfrequencies, whereas the isoscalar-like solutions, being damped, are not found in this ap-

proach. However, one should remind that the isoscalar-like modes, which have been investigated in the hydrodynamical framework, are anyway recovered in the context of finite nuclei.

5.3 Collective modes in finite nuclei

The investigation of collective phenomena in the dynamics of nuclei represents one of the most challenging and lively research fields in nuclear physics. The goal of these studies is to shed light on the main features of some well established collective states, which have an energy larger than the particle separation energy, such as the giant resonances [90, 169] and to evidence their connection with the properties of the effective interaction.

5.3.1 Strength function and transition densities

The collective modes in a finite nuclear system can be generally described as time-dependent oscillations of the nucleus after a perturbation of the ground state [182] or an excited state. One can therefore consider an (instantaneous) perturbation at $t = t_0$ such that:

$$\hat{V}_{ext}(t) = \eta_k \delta(t - t_0) \hat{D}_k, \tag{5.13}$$

where $\hat{D}_k$ is the operator corresponding to the excitation one wants to study and η_k is a constant which is supposed to be small. According to basic quantum mechanics, if $|\Phi_0\rangle$ is the state before perturbation, then the excited state becomes $|\Phi_k(t_0)\rangle = e^{i\eta_k \hat{D}_k} |\Phi_0\rangle$ and the value of η_k can be related to the initial expectation value of the collective dipole momentum $\hat{\Pi}_k$, which is canonically conjugated to the collective coordinate $\hat{D}_k$, i.e., $[\hat{D}_k, \hat{\Pi}_k] = i\hbar$.

Within the linear response theory, the expectation value of the operator $\hat{D}_k$ as a function of time is given by [71]:

$$\begin{aligned} \delta\langle \hat{D}_k \rangle(t) &= \langle \hat{D}_k \rangle(t) - \langle \Phi_0 | \hat{D}_k | \Phi_0 \rangle \\ &= -\frac{2\eta_k \Theta(t - t_0)}{\hbar} \sum_n |\, \langle \Phi_n | \hat{D}_k | \Phi_0 \rangle \,|^2 \sin \frac{(E_n - E_0)\, t}{\hbar}, \end{aligned} \tag{5.14}$$

where E_0 is the energy of the ground state of the unperturbed Hamiltonian, $|\Phi_n\rangle$ is an excited state and E_n its corresponding energy. Defining then the strength response function as usual by

$$S_k(E) = \sum_{n>0} |\langle\Phi_n|\hat{D}_k|\Phi_0\rangle|^2 \delta\left(E - (E_n - E_0)\right), \tag{5.15}$$

it is easy to show that one can also obtain $S_k(E)$ from $\delta\langle\hat{D}_k\rangle(t)$ by taking the imaginary part of its Fourier transform, viz

$$S_k(E) = -\frac{1}{\pi\eta_k}\int_{t_0}^{\infty} dt\delta\langle\hat{D}_k\rangle(t)\sin\frac{Et}{\hbar} = \frac{\mathrm{Im}D_k(E)}{\pi\eta_k}, \tag{5.16}$$

being $D_k(E) = \int_{t_0}^{\infty} D_k(t)e^{-\frac{iEt}{\hbar}}dt$.

In addition to the investigation of the response function, the analysis of the transition densities associated with the different excitation modes of the system is very instructive in the study of the collective modes, since it delivers important information about the spatial structure related to the dynamics of every excitation. The overall spatial structure of the transition densities also indicates which part of the system (internal part, surface) is more involved in the oscillation.

However, the perturbation $\hat{V}_{ext}$ agitates simultaneously all modes which can be excited by the operator $\hat{D}_k$. Thus the corresponding density oscillations observed along the dynamical evolution will appear as the result of the combination of the different excitation modes. In order to pin down the contribution of a given mode to the density oscillations, one can consider the energy E associated, for instance, with a peak in the strength function and compute the transition density as the Fourier transform of $\delta\rho(\mathbf{r},t)$:

$$\delta\rho(\mathbf{r},E) \propto \int_{t_0}^{\infty} dt\delta\rho(\mathbf{r},t)\sin\frac{Et}{\hbar}. \tag{5.17}$$

So, in order to undertake this analysis, one needs to evaluate the local spatial density as a function of time.

5.4 Dipole excitations in neutron-rich systems

With the advent of the first-generation exotic-beam facilities, much attention has been in particular directed towards the study of the collective (multipole) response of nuclei far from the stability. Many investigations have been devoted for example to the evolution of the well-known Giant Dipole Resonance (GDR), which is still the object of intense research.

5.4.1 Giant and Pigmy Dipole Resonance

Restricting the discussion to dipole excitations of neutron-rich systems, one generally observes a stronger fragmentation of the response than in stable nuclei, with significant components located in an energy domain well below that of the GDR [2, 41, 91, 104, 105, 154, 174, 195]. The nature of these low-lying excitations is still a matter of ongoing discussions [5, 52, 130].

Unlike the GDR, where neutrons and protons move against each other, the strength of these modes could be associated with an oscillation of the neutron excess at the nuclear surface (neutron skin) against the isospin-symmetric core. This mode is commonly referred to as Pygmy Dipole Resonance (PDR). This interpretation was already discussed in the early 1990s [173, 184] and is supported by recent calculations based on relativistic random phase approximation (and its extensions) [114, 200].

On the other hand, some microscopic studies predict, for ^{132}Sn, a large fragmentation of the GDR strength and the absence of collective states in the low-lying excitation region [159, 160], thus relating the observed strength to a particular structure of the single-particle levels. Therefore a number of critical questions concerning the nature of the PDR still remain.

It is worth noting that the low-lying electric dipole E1 strength in unstable neutron-rich nuclei is currently discussed also in the astrophysical context, in connection with the reaction rates in the r-process nucleosynthesis. It appears that the existence of the pygmy mode could have a strong impact on the abundances of the elements in the Universe [83, 178]. Moreover, as it has been evidenced in mean-field based calculations, the features of neutron-rich nuclei, such as pygmy mode and neutron skin, are clearly related to the

isovector terms of the nuclear effective interactions, discussed in Chapter 1.

In view of the importance of these dipole excitations, in the following we will focus only on the E1 dipole response of nuclei with a strong neutron excess.

5.4.2 Isoscalar and isovector dipole perturbation

The E1 (isoscalar and isovector) response of nuclear systems can be generally investigated by introducing dipole excitations along a given z direction with the following $\hat{D}_k$ operators [15, 202]:

$$\hat{D}_S = \sum_i \left(r_i^2 - \frac{5}{3}\langle r^2 \rangle \right) z_i, \qquad \hat{D}_V = \sum_i \left[\tau_i \frac{N}{A} z_i - (1-\tau_i)\frac{Z}{A} z_i \right], \quad (5.18)$$

where $k = \mathrm{S}, \mathrm{V}$ for isoscalar (IS) or isovector (IV) perturbation, respectively, $\tau_i = 1(0)$ for protons (neutrons) and

$$\langle r^2 \rangle = \frac{1}{A} \int d^3\mathbf{r} r^2 \rho(\mathbf{r}, t) \quad (5.19)$$

denotes the mean square radius of the nucleus considered. We note that the operator D_V actually contains also an isoscalar component, which vanishes only for symmetric (N = Z) systems. By considering both IS and IV perturbations one gets a complete investigation of the dipole excitations, which could evidence the mixing in the isoscalar-isovector character of the collective modes, expected in neutron-rich nuclei in analogy with some features already discussed in the context of infinite nuclear matter [14, 50].

As far as the transition densities are concerned, we exploit the cylindrical symmetry of the initial perturbation. In order to reduce numerical fluctuations in evaluating the time evolution of the spatial density, one can average over the azimuthal ϕ angle and extract the density $\rho_q(r, \cos\theta, t)$ of the nucleonic species q and the corresponding fluctuation $\delta\rho_q(r, \cos\theta, t) = \rho_q(r, \cos\theta, t) - \rho_q(r, t_0)$ of Eq. (5.17), where $\cos\theta = z/r$ and $\rho_q(r, t_0)$ denotes the ground state density profile which, for spherical nuclei, only depends on r. As suggested in [182], assuming that the amplitude of the oscillation is

weak (linear response regime), the spherical symmetry of the ground state and the dipole form of the excitation operator imply that the transition density can be written, at each time, as: $\delta\rho_q(r, \cos\theta, t) = \delta\rho_q(r, t)\cos\theta$. In such a way, one can finally extract the transition density used as a function of the radial coordinate r, just by averaging over $\cos\theta$ the quantity $\delta\rho_q(r, t)$.

5.5 Semi-classical Vlasov model

In the past, studies based on semi-classical approaches, such as Goldhaber-Teller (GT) [80] or Steinwedel-Jensen (SJ) [172] models, have given an important contribution to the understanding of the main features of giant resonances and of their link to important nuclear properties, such as incompressibility and symmetry energy. In particular, the models based on the Vlasov equation Eq. (1.50) have already been shown to describe reasonably well some relevant properties of different collective excitations of nuclei [1, 30]. It is clear that, within such a semi-classical description, shell effects, certainly important in shaping the fine structure of the dipole response [152], are absent. However, the genuine collective features of the nuclear excitations should naturally come out from this analysis and therefore this kind of studies reveal crucial in the understanding of the nature of these modes. In particular, our investigation contributes in bringing to light the collective behavior exhibited by the PDR, as well as in establishing a connection between the properties of this resonance and the details of the interaction.

5.5.1 Effective interaction and test-particle method

The aim of our work has been therefore to investigate the dipole response of neutron-rich nuclei, by solving the two coupled Vlasov kinetic equations for the neutron and proton distribution functions $f_q(\mathbf{r}, \mathbf{p}, t)$, with $q = n, p$, bearing in mind the modification introduced in Eq. (1.50) since SAMi-J effective interaction are momentum dependent (MD). However, in order to make a connection with previous studies, we also consider the momentum independent (MI) Skyrme interactions described in section 2.5, with the addition of

the asysuperstiff EoS (see Table 1.1), $C_{pot}(\rho) = 18\frac{\rho}{\rho_0}\frac{2\rho}{(\rho+\rho_0)}$ MeV, where the symmetry term increases rapidly around saturation density, being characterized by a large value of the slope parameter. The density behavior of the symmetry energy for these MI interaction is shown in panel (a) of Fig. 5.1, to be compared with the trend observed for the SAMi-J parameterizations. In both cases, we neglect the spin-orbit term in the Eq. (1.38), while we include the Coulomb interaction.

The integration of the transport equations is based on the test-particle (t.p.) (or pseudoparticle) method [199], which is able to reproduce accurately the equation of state of nuclear matter and provide reliable results regarding the properties of nuclear surface and ground state energy for finite nuclei [16]. We choose to consider 1500 t.p. per nucleon in all cases, ensuring in this way a good spanning of the phase space. Because test particles are often associated with finite width wave packets (we use triangular functions [85]), some surface effects are automatically included in the initialization procedure and in the dynamics, even though explicit surface terms, such as those contained in the effective Skyrme interactions, are not considered. This implies that, for the surface terms, one cannot simply use the coefficients associated with the SAMi-J parameterizations, while we observe that a good reproduction of the experimental values of the proton root-mean-square radius and binding energy, for the nuclei selected in our analysis, is obtained when taking $C_{surf} = D_{surf} = 0$ in our parameterizations. Thus this choice has been adopted here.

5.5.2 Ground state properties and density profile

Here and in the next sections, as in our recent work [202], we concentrate our analysis on three mass regions, considering the following neutron-rich nuclei: ^{68}Ni ($N/Z = 1.43$), ^{132}Sn ($N/Z = 1.64$), ^{208}Pb ($N/Z = 1.54$).

In order to determine the ground state configuration of the nuclei under study, one should find the stationary solution of Eq. (1.50). We adopt the following numerical procedure: neutrons and protons are distributed inside spheres of radii R_n and R_p, respectively and, accordingly, in the Thomas-Fermi approximation, particle momenta are initialized inside Fermi spheres

associated with the local neutron or proton densities. Then R_n and R_p are tuned in order to minimize the corresponding total energy, associated with the effective interaction adopted in the calculations.

The values of binding energy and of neutron and proton root-mean-square radii correspondingly deduced are reported in Table 5.1 for the SAMi-J interactions.

Table 5.1: Neutron and proton root mean square radii, and their difference, and binding energy for three nuclei under study, as obtained in semi-classical model with the SAMi-J interactions. The experimental values are also indicated.

	$\sqrt{\langle r^2\rangle_n}$ [fm]	$\sqrt{\langle r^2\rangle_p}$ [fm]	$\sqrt{\langle r^2\rangle_n} - \sqrt{\langle r^2\rangle_p}$ [fm]	$\frac{B}{A}$ [MeV]
		^{68}**Ni**		
SAMi-J27	4.043	3.889	0.154	9.130
SAMi-J31	4.102	3.898	0.204	9.050
SAMi-J35	4.143	3.900	0.243	8.971
Exp (^{64}Ni)	—	3.857	—	8.682
		^{132}**Sn**		
SAMi-J27	4.940	4.728	0.212	8.637
SAMi-J31	5.035	4.741	0.294	8.552
SAMi-J35	5.150	4.753	0.397	8.405
Exp	—	4.709	—	8.354
		^{208}**Pb**		
SAMi-J27	5.648	5.513	0.135	8.105
SAMi-J31	5.735	5.536	0.198	8.042
SAMi-J35	5.813	5.549	0.264	7.930
Exp	—	5.5012	—	7.867

In Fig. 5.6, we show the neutron and proton density profiles, obtained for example for the system ^{132}Sn, with the three SAMi-J parameterizations considered in our study. As expected, the neutron skin thickness increases with the slope parameter L: this effect is indeed related to the derivative of the symmetry energy around saturation density.

When the symmetry energy decreases significantly below ρ_0, as in the case of the asy-superstiff EoS or the SAMi-J35 interaction, it is energetically convenient for the system to push the neutron excess towards the nuclear surface.

The same trend is observed for the ^{68}Ni and ^{208}Pb ground state configuration (see Table 5.1) and also for the MI interactions [16]. However, it should be noticed in Fig. 5.6 that, in the case of the SAMi-J interactions, the different value of the symmetry energy at saturation induces a quite different behavior of the neutron density also in the bulk.

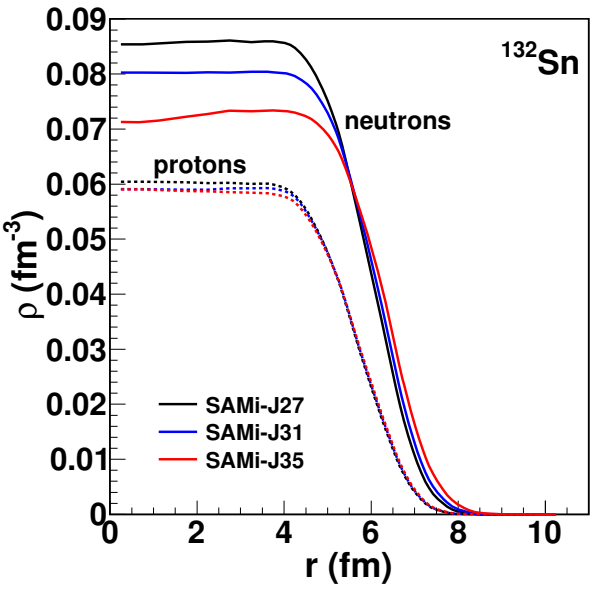

Figure 5.6: Neutron (full lines) and proton (dashed lines) density profiles of ^{132}Sn for the SAMi-J parameterizations, as obtained in Thomas-Fermi approximation.

5.6 Collective dipole response in Vlasov model

Dipole oscillations and response functions can be investigated, considering an initial IS or IV perturbation of the ground state configuration of the nucleus under study and then looking at its dynamical evolution. In our Vlasov calculations, according to Eq. (5.18), we assume $\eta_S = 0.5$ MeV fm^{-2}, $\eta_V = 25$ MeV and we run the time evolution until $t_{max} = 1800$ fm/c. A filtering procedure, as described in [149], was applied in order to eliminate the artifacts which result when extracting oscillations of the dipole moments from a finite time domain analysis of the signal. Thus a smooth cut-off function was introduced such that $D_k(t) \to D_k(t)\cos^2\left(\frac{\pi t}{2t_{max}}\right)$. Correspondingly, also the sine function in Eq. (5.17) comes out to be multiplied by a damping factor.

In this section we are going to examine the results concerning the isoscalar and isovector dipole response for the selected nuclei in three different mass regions considered in section 5.5.2.

5.6.1 Coupling between IS and IV mode

As it has been already mentioned in Chapter 1, as well as in section 5.2, in symmetric nuclear matter isoscalar and isovector modes are fully decoupled. We have stressed, moreover, how in neutron-rich systems, neutrons and protons may oscillate with different amplitudes, inducing a coupling of isoscalar and isovector excitations. One of the goals of the analysis we have carried out in a recent work [202] has been to get a deeper insight into this effect.

In Fig. 5.7, we represent dipole oscillations (left panels) and corresponding strength, as a function of the excitation energy $E = \hbar\omega$ (right panels) for the system ^{132}Sn and the SAMi-J31 interaction. One can observe that, when introducing an IS perturbation at the initial time t_0 (Fig. 5.7, panels (a)-(b)), also isovector-like modes are excited, as it is evidenced from the analysis of the corresponding isovector dipole oscillations and associated strength (panels (c)-(d)). Similarly, an initial IV perturbation (panels (e)-(f)) also generates an isoscalar response (panels (g)-(h)).

In the isovector response (panel (f)) one can easily recognize the main IV GDR peak, with $E_{GDR} \approx 14$ MeV.

Some strength is also evidenced at lower energy (mostly in the range between $E_1 = 9$ MeV and $E_2 = 11$ MeV), which could be associated with the PDR. These low-energy modes contribute significantly to the corresponding isoscalar projection (panel (h)), now acquiring a larger strength, comparable to that associated with the robust GDR mode, thus manifesting their isoscalar-like nature. A (negative) peak is seen at higher energy (around 29 MeV), which corresponds to the giant isoscalar-like dipole mode (IS GDR) which is also excited, owing to its mixed character, by the initial perturbation. When agitating the system with an initial isoscalar excitation, essentially the same oscillation modes emerge, with a larger strength for the isoscalar-like ones in this case.

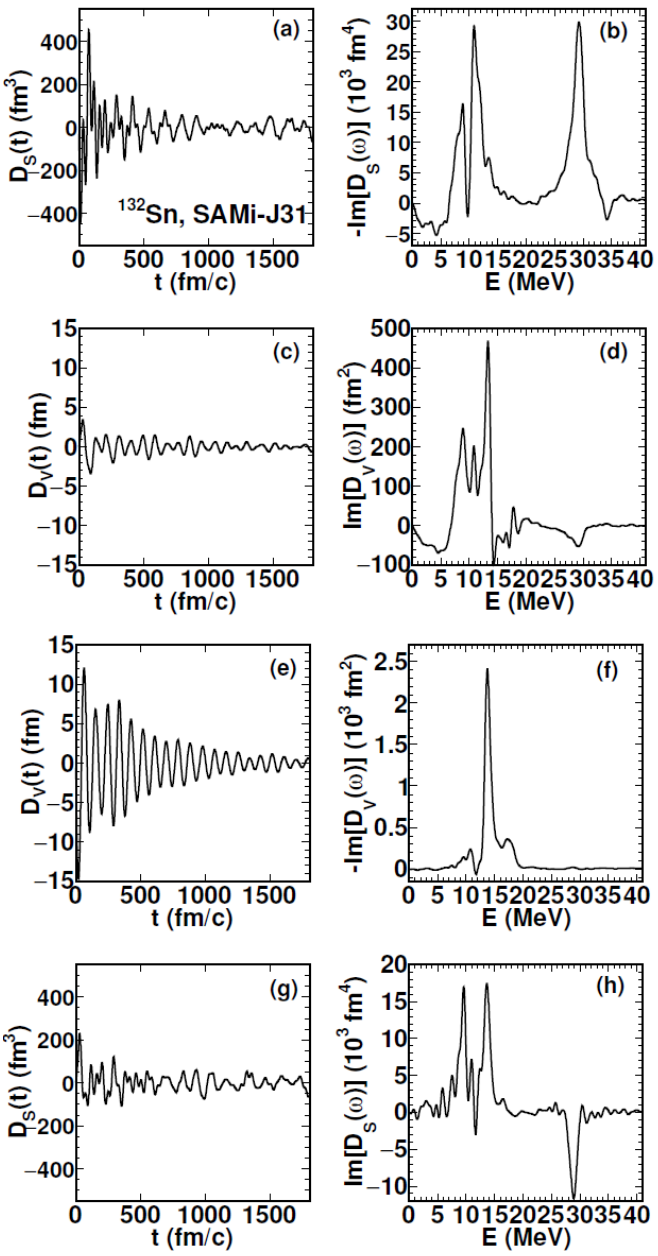

Figure 5.7: Dipole oscillations (left panels) and corresponding strength (right panels), as obtained in semi-classical Vlasov model for ^{132}Sn and SAMi-J31 interaction. Panels from (a) to (d) are deduced employing an initial IS perturbation, while panels from (e) to (h) are obtained with an initial IV one.

Indeed, in the isoscalar response (panel (b)) two main peaks, whose positions are quite close to the E_1 and E_2 energies evidenced in panel (h), are observed in the low energy region, together with some strength located around the IV GDR region. A quite large contribution appears also in the high energy region of the spectrum. Projecting onto the isovector direction (panel (d)) the strength of the IV GDR mode is enhanced, as expected according to its isovector-like nature, becoming comparable to that of the low-energy isoscalar-like modes excited by the initial perturbation. On the other hand, the high energy mode exhibits a quite small (negative) strength, pointing again to its isoscalar-like character.

To summarize, we observe that the same energy modes, which are ac-

tually the normal modes of the system and are of mixed nature, appear at the same time in the isoscalar and isovector responses of the system, but with a different weight, depending on their intrinsic structure and on the initial perturbation type. In particular, the low-energy modes, lying below the GDR peak, have predominant isoscalar nature, but they may also contribute to the isovector response, in the PDR region.

5.6.2 Dependence on the effective interaction

We move now to investigate how the response of the system depends on the effective interaction adopted, in the three mass regions considered in our work. Hereafter we will only examine the isoscalar (isovector) response connected to an initial isoscalar (isovector) perturbation.

In the left panels of Fig. 5.8, we show, for the three nuclei considered, the strength function as a function of the excitation energy E corresponding to the IS dipole response, while in the right panels the same quantity is shown for the IV one. In all panels, the predictions of the three selected SAMi-J interactions are shown.

For ^{68}Ni and ^{132}Sn, the isoscalar strength appears quite fragmented in the low-energy domain. However one can recognize two main regions of important contribution for all the interactions considered (see in particular the SAMi-J35 results) and identify a smaller peak centered at the energy of the IV GDR (originating from its mixed nature in neutron-rich systems, as stressed above). It is worth noting that the observation of two main low-energy peaks in the isoscalar response is in agreement with the semi-classical studies of [182], where isoscalar toroidal excitations are investigated. In particular, in [182] it is shown that the lowest energy mode is associated mostly with surface oscillations and, in the case of neutron-rich systems, is responsible for the low-lying strength observed in the isovector response (in the PDR region). For the largest system considered, ^{208}Pb, our calculations show instead essentially just one main peak, of significant strength, in the low-energy region. In any case, the low-energy peaks of the IS response appear connected to the low-lying strength observed in the IV response.

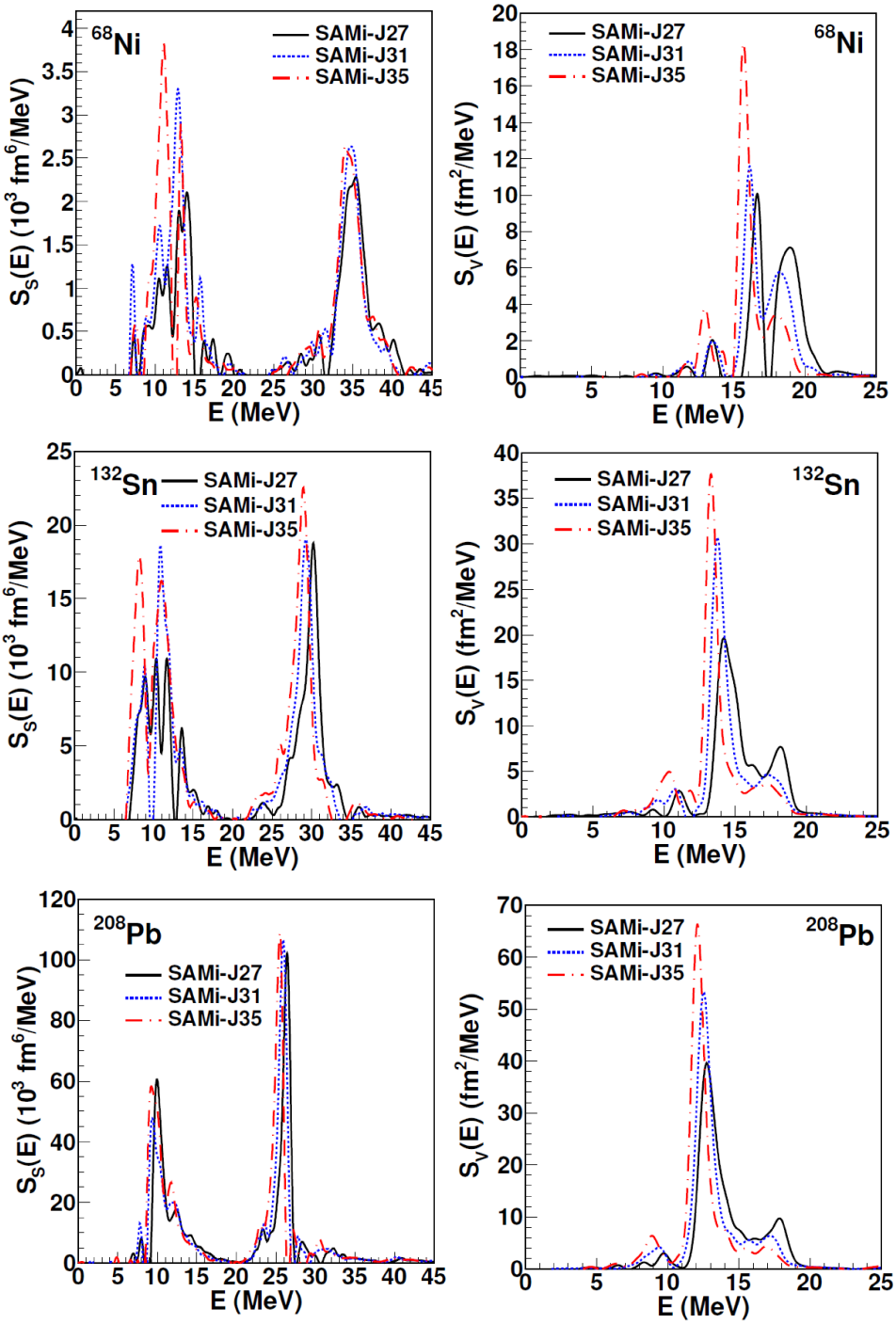

Figure 5.8: Strength functions versus excitation energy for all nuclei of Table 5.1, as obtained in semi-classical Vlasov model and for each SAMi-J parameterizations considered. Left panels are for the initial IS perturbation and right panels for the initial IV one.

Neverthless, since the different peaks are quite close to each other, only one main peak, resulting from two interfering contributions, may appear in the PDR region.

Let us concentrate now on the details of the isovector response. In the ^{208}Pb case, the centroid energies of the PDR as well as the energy peak of the isovector GDR predicted by the employed interactions (E = 8 - 10 MeV and E = 12.5 - 13 MeV, respectively) are close to the experimental data (E = 7.37 MeV within a window of 6 - 8 MeV [156] and E = 13.43 MeV with a total width of 2.42 MeV [19] respectively).

The predictions of the three SAMi-J interactions for the PDR, for ^{132}Sn (E = 9.0 - 11.0 MeV) and for ^{68}Ni (E = 11.5 - 13.5 MeV), are also close, but still a little higher than the measured data (E = 9.1 - 10.5 MeV for ^{132}Sn [2] and E =11 MeV with an energy width estimated to be less than 1 MeV for ^{68}Ni [154, 196]). The overestimation of the PDR energy in our calculations may be connected to the semi-classical treatment of surface effects and, for that reason, it appears more critical in smaller systems, where the relative importance of surface to volume effects increases. Indeed the PDR region is essentially populated by low-lying isoscalar-like oscillations, whose structure is significantly affected by surface effects. This result can be probably improved through a fine tuning of the coefficients C_{fin} and D_{fin} in the Skyrme parameterizations.

Qualitatively, in the three nuclei it appears that the larger the value of L, the higher the different peaks arising in the low-energy region of the IV dipole response (see Fig. 5.8, right panels). Moreover, as it clearly appears from left panels, the strength of the lowest energy mode in the IS response increases (except for ^{208}Pb) when increasing the slope L of the parameterization considered. On the basis of nuclear matter calculations in neutron-rich systems, as it has been shown in section 5.2, we expect in fact a larger degree of mixing between isoscalar and isovector modes, for symmetry energy parameterizations with larger slope L [13]. Since this corresponds also to a more extended neutron skin (see Fig. 5.6), one can conclude that surface and isospin effects are both enhanced.

Finally, we observe for all nuclei that the IV projection of the PDR is an

order of magnitude smaller than the IV GDR, but its isoscalar counterpart is of the same order of magnitude as the corresponding IS GDR. We conclude that the PDR is mostly an isoscalar low-energy mode, involving nucleons which belong also to the nuclear surface. Owing to the charge asymmetry of the systems considered, this mode also manifests an isovector character, especially in the case of the stiffer interactions, which predict a larger asymmetry in the surface (neutron skin), as it emerges in the density profile of Fig. 5.6.

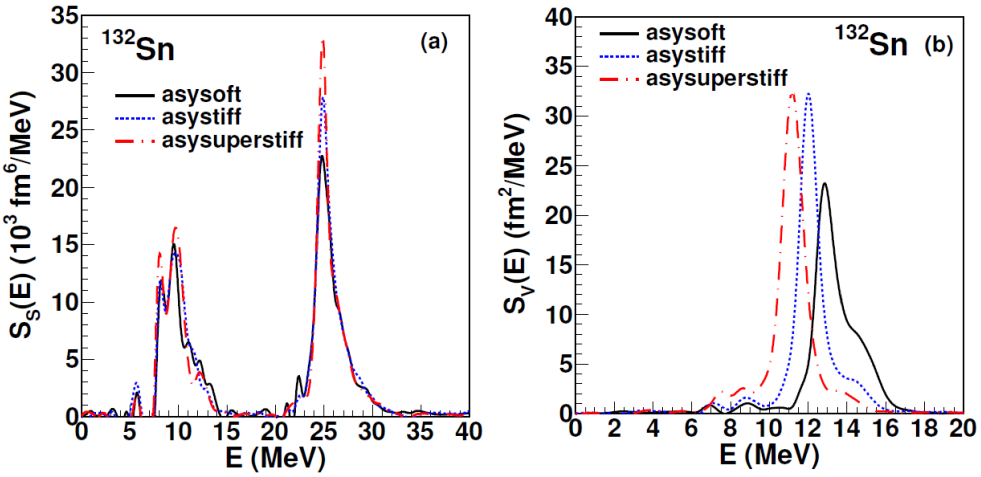

Figure 5.9: Strength functions versus excitation energy for ^{132}Sn as obtained in semi-classical Vlasov model and for each MI interaction considered. Panel (a) is for the initial IS perturbation and panel (b) for the initial IV one.

Actually the IV response also exhibits other interesting features, which can be better discussed by comparing with the results obtained with the MI Skyrme interactions and displayed in Fig. 5.9 for ^{132}Sn. Concerning the dominant IV GDR, our calculations indicate that its excitation energy is mainly affected by the value of the symmetry energy at the density $\rho_c = 0.65\ \rho_0$, where the three SAMi-J interactions cross each other (see Fig. 5.1). Indeed, the centroid of the IV GDR peak does not evolve much with the parameterization considered, in the SAMi-J case. The largest shift is observed for the smallest system, ^{68}Ni, indicating that the GDR centroid is actually sensitive to the value of the symmetry energy at a density below ρ_c in this case. On the other hand, for the MI parameterizations, which cross at normal density

(see Fig. 5.1, panel (a)), thus exhibitng a larger difference of the symmetry energy value below ρ_0, the energy centroid is clearly more sensitive to the parameterization employed, being smaller in the asysuperstiff case (see Fig. 5.9, panel (b)). We also stress that the GDR energy appears always underestimated by the MI interactions, whereas it is close to the experimental observation when the SAMi-J interactions are considered, as expected from nuclear matter calculations (see Fig. 5.4). In particular, the SAMi-J31 and the asystiff parameterizations are characterized by a quite similar behavior of the symmetry energy (compare the two panels of Fig. 5.1), nevertheless the results of the dipole response are different in the two cases. Moreover in the isovector dipole response obtained with the SAMi-J, we also observe a quite pronounced peak at higher energy, with respect to the GDR, whose strength decreases with the stiffness of the interaction, in agreement with RPA calculations [152]. This peak is however less pronounced in the MI case, highlighting also the role of momentum dependent effects in shaping the features of the nuclear response.

5.6.3 Spatial structure of low-lying energy modes

In section 1.6.2 of Chapter 1 as well as in section 5.2, we already discussed how in symmetric matter neutrons and protons oscillate with exactly equal (isoscalar) or opposite (isovector) amplitudes. Although in neutron-rich systems the picture is more complex, it has been argued that one can still identify isoscalar-like modes, when the two nuclear species oscillate in phase, and isovector-like modes, with neutrons and protons oscillating out of phase. To further analyze the isoscalar or isovector character of each excitation mode and their overall spatial structure, we evaulate here neutron and proton transition densities, according to the definition given in Eq. (5.17).

In Fig. 5.10, in particular, we represent the transition density associated with the low energy peaks, as observed in the isoscalar response, for the three systems considered and the three SAMi-J parameterizations adopted. Actually the transition density associated to these peaks could also be extracted from the isovector response, but since the IV strength is quite small,

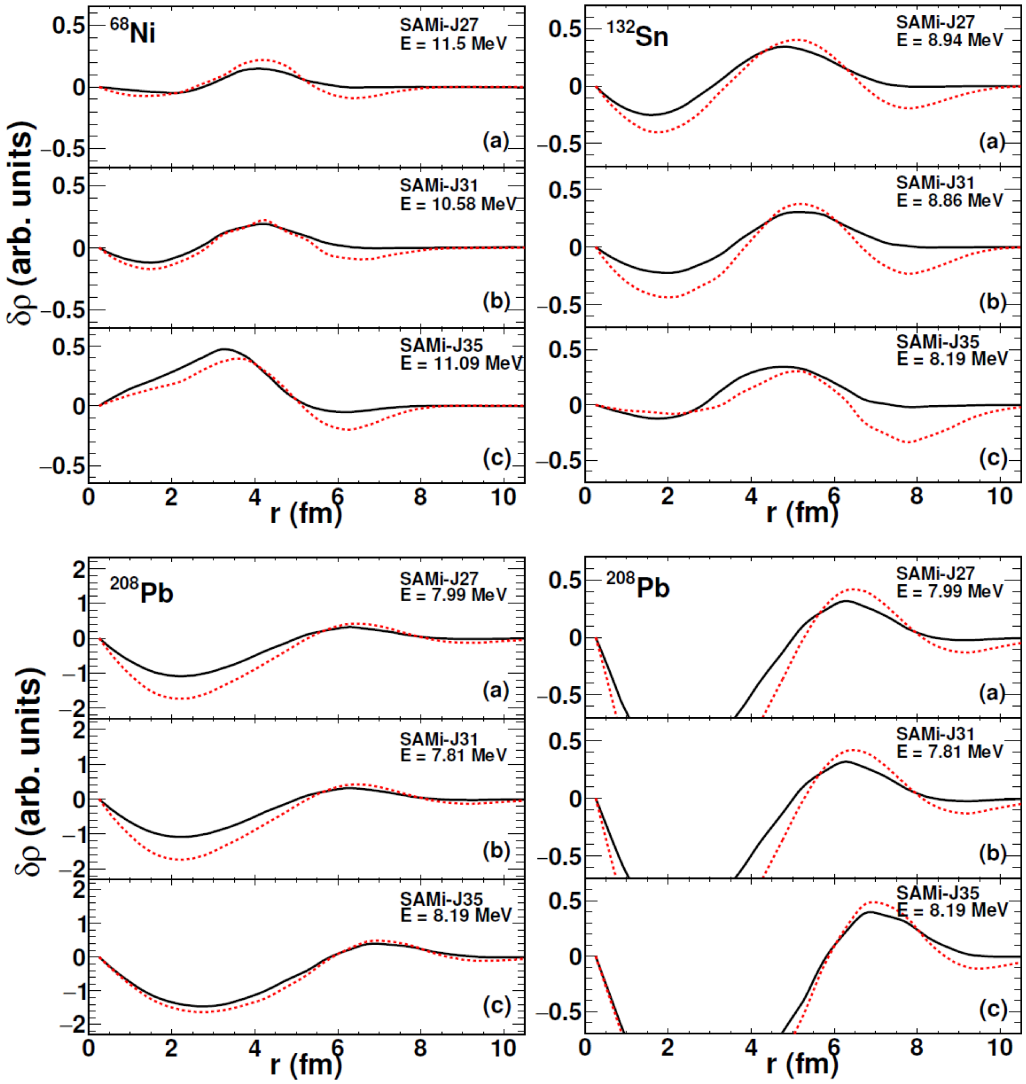

Figure 5.10: Transition densities, as obtained in semi-classical Vlasov model, for the peak in the pygmy dipole resonance region as a function of the radial distance. An initial IS perturbation is employed and, for all nuclei of Table 5.1, all the SAMi-J parameterizations are considered. Full black lines are for protons, dashed red lines for neutrons. The energy of the excitation mode considered is indicated in each panel. For ^{208}Pb, a reduced scale on the vertical axis is also used to better evidence the surface behavior.

numerical fluctuations would spoil the signal.

We observe that neutrons and protons oscillate in phase, but with different amplitudes, with neutrons having generally larger amplitude than protons. The nuclear surface is significantly involved in these oscillations. Moreover, when considering interactions with increasing slope L (from SAMi-J27 to SAMi-J35), one can see that neutron oscillations become larger, with respect to proton oscillations, especially in the surface region, whereas the opposite seems to hold for the interior of the system. This can be explained by the fact that, for increasing L, the system asymmetry is more pushed towards the surface, corresponding to the development of the neutron skin, whereas the internal part of the system becomes more symmetric. As one can see from the right-bottom panel of Fig. 5.10, where the surface region of the transition density is better evidenced, surface effects are less pronounced in the ^{208}Pb case. However, a significant contribution to the dipole strength may also come from the intermediate spatial region, where the transition densities are positive[1]. This determines an overall increase of the mixed character of the mode, mainly determined by the surface behavior, but also by the internal part of the system, leading to a larger strength observed in the isovector response, see Fig 5.8.

Transition densities for the other modes. We also extend our analysis to the other modes giving a relevant contribution to the isoscalar and the isovector responses. This is illustrated in Fig. 5.11, for the system ^{132}Sn, in the case of the SAMi-J31 interaction, and for IS (left panels) and IV (right panels) excitations, respectively.

As it is observed from the analysis of the isoscalar response (see Fig. 5.8), there exists a second mode, around $E_2 = 11$ MeV, which gives an important contribution in the low-energy region. Looking at the associated transition density generated by an IS perturbation of the system, it appears that neutrons and protons essentially move in phase, but still with different ampli-

[1]According to the definition of the IV dipole operator Eq. (5.18), the dipole strength increases when $\frac{\delta\rho_n}{\delta\rho_p} > \frac{N}{Z}$, for negative transition densities, or when $\frac{\delta\rho_n}{\delta\rho_p} < \frac{N}{Z}$, for positive transition densities. Both conditions are better satisfied, in the surface and in the intermediate region respectively, with increasing L.

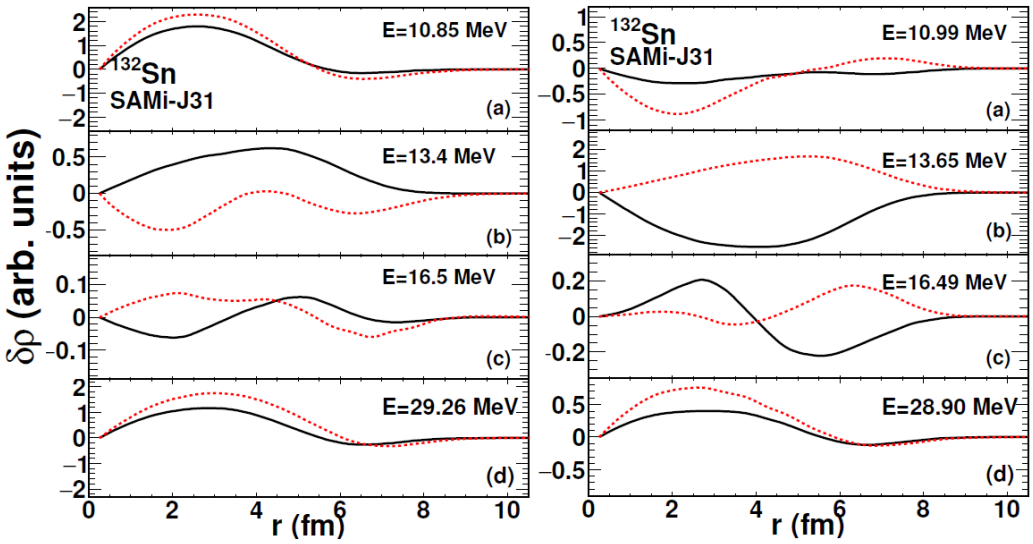

Figure 5.11: Transition densities, as obtained in semi-classical Vlasov model, for all the modes with a peak in the strength as a function of the radial distance r. An IS (left panels) or IV (right panels) initial perturbation is considered, for ^{132}Sn and with SAMi-J31 interaction. Full black lines are for protons, dashed red lines for neutrons.

tudes. Thus the oscillation has a mixed character and this is why it presents some strength in the isovector response. Now the interior of the system is more involved in the oscillation, though the surface is still affected. It is worth noting that, also for this transition density, the asymmetry increases, with L, at the surface and diminishes in the internal part.

We observe that, when this energy region is excited from the IV operator, though the structure of the mode keeps similar (apart from the sign, which is not relevant), the difference between neutrons and protons becomes more pronounced. This effect could be due to the influence of the strong isovector oscillations associated with the IV GDR region, whose contribution may extend to the considered energy, so that GDR and PDR may overlap. Indeed, as it has been already stressed in section 5.3.1, even if the energy E corresponds to a peak in $S_k(E)$, the transition densities obtained with the method employed here may still contain contributions from other modes if those have a width which makes their spectrum extend to the energy E [182]. It is moreover interesting to underline that the splitting of the PDR into a

low-energy, mostly isoscalar contribution and a higher energy region with a more pronounced isovector character has been pointed out in recent experimental and theoretical analyses [52, 69].

The highest energy isoscalar mode, that should be associated with the isoscalar giant dipole compression mode, corresponds to transition densities which affect significantly the interior of the system (Fig. 5.11, panels (d)) and its features do not depend much on the type of initial perturbation. Moreover it appears of quite robust isoscalar nature, with a tiny isoscalar/isovector mixing at the surface.

It is also interesting to look at the modes which are isovector-like. In this case neutrons and protons oscillate mostly out of phase, with protons having larger amplitude. As one can deduce comparing panels (b) and (c) in Fig. 5.11, the transition densities extracted from the isoscalar or from the isovector responses exhibit similar features. It appears that the main IV GDR mode (panels (b)) corresponds essentially to one oscillation, with a maximum close to the nuclear surface. This result is compatible with GT picture of neutron and proton spheres oscillating against each other. On the other hand, the higher energy peak, $E \approx 16.5$ MeV (panels (c)), corresponds to a kind of double oscillation, which is typical of SJ modes, i.e. volume oscillations, involving also the internal part of the system.

The full energy spectrum of transition densities, as obtained considering an initial IS [panels (a) and (b)] or IV [panels (c) and (d)] perturbation, at two radial distances is shown in Fig. 5.12 for the system ^{132}Sn and the SAMi-J31 interaction. One can observe again that the low-energy region, on the left of the GDR peak, corresponds mostly to isoscalar-like excitations, where neutrons and protons move in phase. The same is seen at energies greater than E $\approx$ 17 MeV. On the other hand, the energy region E $\approx$ 13–17 MeV is clearly characterized by isovector-like excitation modes.

Final remarks. In order to conclude this section, let us stress the important result one gets from our analysis: the evidence of a relevant degree of isoscalar-isovector mixing of the collective excitations developing in neutron-rich systems, in analogy with some features underlined in the nuclear matter

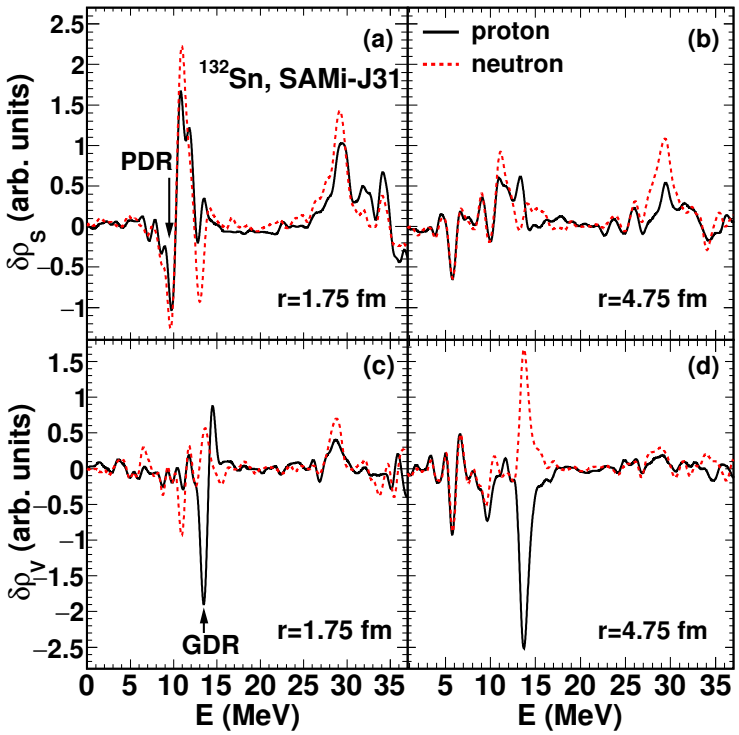

Figure 5.12: Transition densities, as obtained in semi-classical Vlasov model considering an initial IS [(a) and (b)] or IV [(c) and (d)] perturbation, as a function of the excitation energy E, for ^{132}Sn and the SAMi-J31 interaction, at two radial distances: $r = 1.75$ fm and $r = 4.75$ fm.

context. Focusing in particular on the low-lying strength emerging in the isovector response, we show that this energy region essentially corresponds to the collective excitation of isoscalar-like modes, which also contribute to the isovector response owing to their mixed character. Considering effective interactions which mostly differ in the isovector channels, we observe that these mixing effects increase with the slope L of the symmetry energy, leading to a larger strength in the low-energy region of the isovector response. This result appears connected to the increase, with L, of the neutron-proton asymmetry at the surface of the considered nuclei, i.e., to the neutron skin thickness.

5.7 Comparison with quantal calculations

The semi-classical model investigated in this chapter has demonstrated reliable in describing the ground state properties and in shaping the main features of the collective response of the nuclei under study. To confirm the

Table 5.2: Neutron and proton root mean square radii, and their difference, and binding energy for the three closed shell nuclei under study, as obtained with the SAMi-J interactions in HF calculations.

	$\sqrt{\langle r^2\rangle_n}$ [fm]	$\sqrt{\langle r^2\rangle_p}$ [fm]	$\sqrt{\langle r^2\rangle_n} - \sqrt{\langle r^2\rangle_p}$ [fm]	$\frac{B}{A}$ [MeV]
		^{68}**Ni**		
SAMi-J27	3.974	3.824	0.150	8.741
SAMi-J31	4.001	3.831	0.170	8.845
SAMi-J35	4.025	3.823	0.203	8.911
		^{132}**Sn**		
SAMi-J27	4.837	4.656	0.181	8.472
SAMi-J31	4.927	4.664	0.263	8.448
SAMi-J35	4.990	4.658	0.331	8.437
		^{208}**Pb**		
SAMi-J27	5.558	5.438	0.120	7.951
SAMi-J31	5.652	5.455	0.197	7.917
SAMi-J35	5.720	5.455	0.265	7.882

validity of the semi-classical method and to check also the role of shell effects and single particle structure on the results, in the following sections we are going to investigate the collective dipole modes by performing some quantal calculations, which are based on TDHF approach (see Chapter 1), to be compared with the previous results.

5.7.1 Modifications on the static properties

In order to appreciate the quantal modifications on the static properties, for each nucleus given in Table 5.1, we employ a code based on the Hartree-Fock equation Eq. (1.20). In particular, we obtain the initial single particle wave functions using the ev8 code [26] that solves the HF equation in r-space with the Skyrme functional in the mean-field term. The ground state properties of the three nuclei under study, as extracted by the HF energy minimization, fill out the Table 5.2 and should be related with the analogous semi-classical results listed in Table 5.1. The data compare rather well,

but evidently the quantal approach gives back values which are closer to the experimental results. The two sets of data overlap especially in the case of ^{208}Pb, confirming the reliability of the semi-classical approach in the reproduction of the heavy ion properties.

The neutron and proton density profiles deduced by adopting the SAMi-J parameterizations are instead illustrated in Fig. 5.13 for the system ^{132}Sn. By comparison with the result of Fig. 5.6, it clearly emerges that the bulk density of the nucleus in the HF case is higher than the one deduced in the semi-classical model. According to the conservation of the total number of particles, this also reflects in a larger compactness of the system, which implies a reduction of the surface diffuseness and of the neutron skin thickness, as one infers from Table 5.2. The same considerations made in the previous section hold instead for the dependence of this thickness on the slope of the symmetry energy.

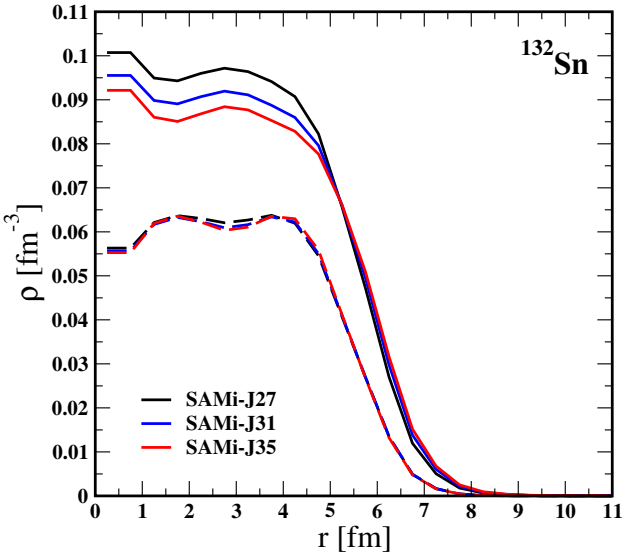

Figure 5.13: Neutron (full lines) and proton (dashed lines) density profiles as in Fig. 5.6, but deduced by performing HF calculations.

Also the behavior of the density profiles in the internal part shows a remarkable difference with respect to the one in Fig. 5.6, which is trivially constant in the bulk region. The quantal HF approach allows in fact to involve shell effects and so more degrees of freedom than the simple Thomas-Fermi approximation and this also reflects into the oscillations observed at intermediate radial distances in Fig. 5.13.

5.7.2 Strength function in quantal approach

To underline if, and eventually how, the difference observed in the density profiles of Figs. 5.6 and 5.13, together with the surface and the shell effects, influence also the response function of the system, one could investigate the small amplitude dynamics of the nuclei under study within the TDHF approach. In this framework, the analysis of the collective dipole modes has been addressed by making use of the three-dimensional code developed by P. Bonche and coworkers [103] and recently adopted also by the IPN-Orsay theory group [162]. The corresponding strength function one obtains, for ^{132}Sn and SAMi-J31 interaction, are illustrated in Fig. 5.14, for an initial IS ($\eta_S/\hbar$ =10^{-4} fm^{-3}, panel (a)) or IV perturbation ($\eta_V/\hbar$ =10^{-4} fm^{-1}, panel (b)), respectively.[2]

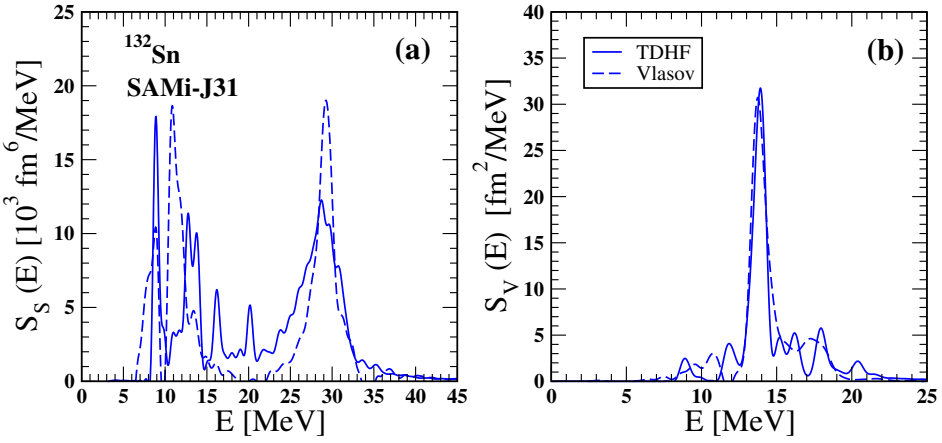

Figure 5.14: Comparison between the strength functions versus excitation energy, as obtained in TDHF calculations and the corresponding result extracted with the semi-classical Vlasov model, for ^{132}Sn and SAMi-J31 interaction. Panel (a) is for the initial IS perturbation and panel (b) for the initial IV one.

Looking at the two panels of Fig. 5.14, the most striking feature one can observe in both panels is the splitting of the peak associated to the PDR

[2]We have adopted here a smaller value of $\eta_k, k = S, V$ with respect to that one used in the semi-classical Vlasov model, because in TDHF calculation it is possible to get the dipole oscillation, even if a so tiny perturbation is employed. Moreover, we remind that in this small amplitude limit the results should be equivalent with those obtained within the RPA approach.

in two different peaks which, according to their mixed nature, appear both in the isoscalar and isovectore response. Similarly to what it is observed in RPA calculations [152], the TDHF results exhibit a more isolated peak in the low-energy region of the IS strength function $S_S(E)$, but some contributions appear also at higher energy, with respect to Vlasov calculations, in a region around the domain of the IV GDR. This latter component of the IS dipole response has been the object of several experimental and theoretical analyses [49, 117, 181]. These studies have pointed out the non-compressional nature of this excitation, in agreement with the findings, based on semi-classical studies of [182]. The discrepancy with respect to the Vlasov calculations may be probably attributed to the lack of intrinsic gradient terms of quantal nature in the semi-classical approach as well as to the numerical treatment of surface effects [7].

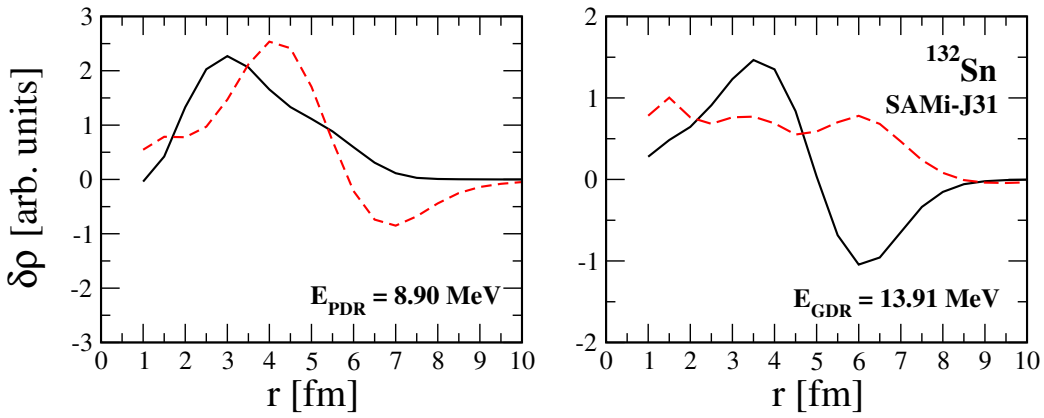

Figure 5.15: Transition densities, as obtained in TDHF approach, for PDR (left panel) and GDR (right panel) as a function of the radial distance r. An IS (left panel) or IV (right panel) initial perturbation is considered, for ^{132}Sn and with SAMi-J31 interaction. Full black lines are for protons, dashed red lines for neutrons.

However, looking at the transition densities in Fig. 5.15, as obtained for the pygmy and the giant dipole resonances, by introducing an initial IS or IV perturbation, respectively, one can observe that the genuine properties which characterize the structure of the two modes are well reproduced in both models. Similarly to semi-classical calculations, the transition densities deduced in the TDHF approach show for the PDR a quite large contribution

in the external part close to the surface, which is mostly isoscalar-like, also in agreement with RPA calculations [152], whereas a more complex behavior is exhibited in the bulk region. The transition densities associated to the main IV GDR peak clearly reveal the isovector-like nature of this mode and, analogously to the ones deduced by the Vlasov model, significantly involve the nucleons of the surface but get important contributions also from the the internal part.

5.8 Pairing effects on the giant resonances

In section 2.3.2, we have already mentioned that the introduction of pairing correlations in semi-classical approaches complicates significantly the study of the small amplitude dynamics of nuclear systems. As a consequence, since we would like to investigate pairing effects on the collective dipole resonances, we resort to the Cb-(TDHFB) extension of the TDHF approach (see section 2.3.1), which include pairing correlations in the BCS approximation [68]. In particular, we would like to analyze the influence of pairing for the tin isotopes chain, according to the importance that these nuclei take on also in the experimental activity research for the pygmy and the giant dipole resonances [2].

A functional form similar to the one given in Eq. (2.33) is adopted for the pairing effective interaction, whose parameters have been fitted in order to reproduce the two particle separation energy S_{2n} for some nuclei of the tin isotopes chain (from ^{128}Sn to ^{136}Sn). We present preliminary results for the axially deformed even-even isotopes ^{130}Sn and ^{128}Sn, since the spherical one ^{132}Sn, being a double-magic nucleus, is not affected by pairing correlations.

The strength functions extracted by the dynamical evolution following an initial IS or IV perturbation are plotted, for both TDHF and TDHF+BCS calculations, in Fig. 5.16. The right panels of the latter figure, which are related to the IV response to an initial IV perturbation, clearly manifest that, whereas for both nuclei the two curves are almost indistinguishable in the PDR region, the excitation energies of the GDR peak is modified by the introduction of the pairing correlations. This effect is even more

pronounced in the case of ^{128}Sn, which moving more away from the closed-shell configuration, presents a larger deformation with respect to ^{130}Sn.

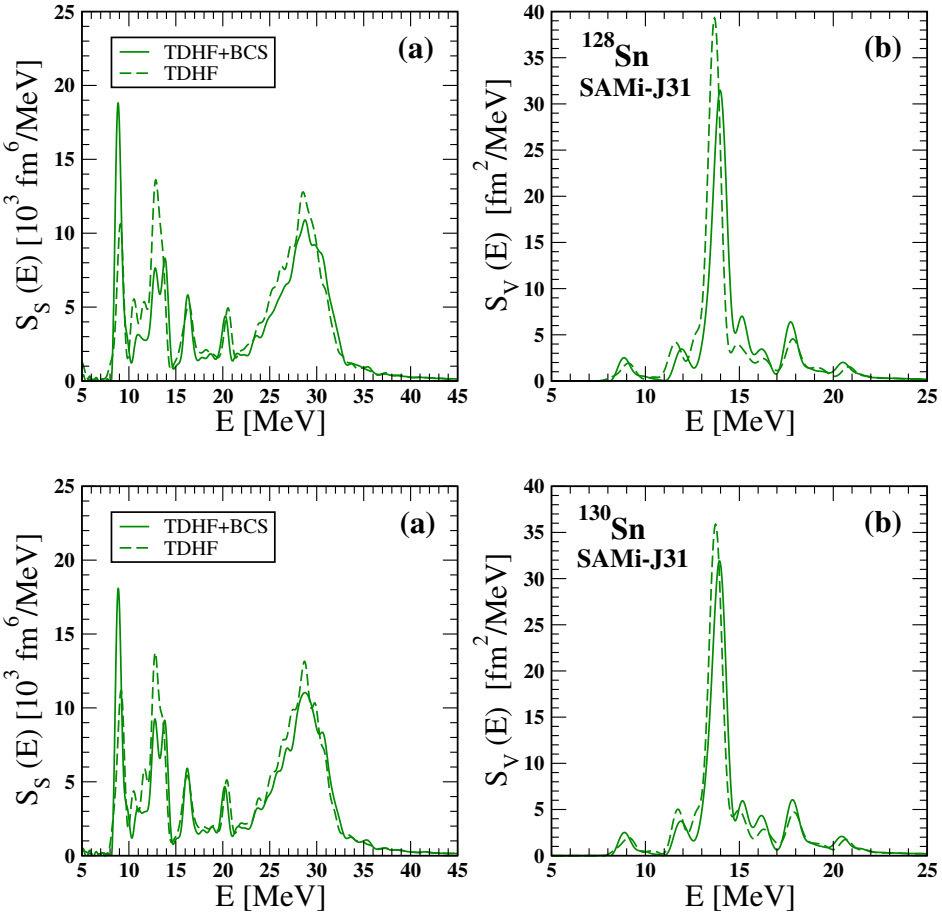

Figure 5.16: Comparison between the strength functions versus excitation energy, as obtained in TDHF+BCS calculations and the corresponding TDHF result extracted neglecting pairing correlations, for two even-even nuclei of the tin isotopes chain and SAMi-J31 interaction. Left panels are related to an initial IS perturbation, right panels to an initial IV one.

It has been pointed out that the difference observed in the dipole response between TDHF and TDHF+BCS calculations comes out exclusively from the initial condition [161], i.e., from the shape exhibited by the nuclei in their ground state. Therefore, we deduce here that, while in absence of pairing correlations the ground states of the two tin isotopes here considered are

deformed, taking into account the formation of Cooper pairs, more spherical shapes become favoured.

More in detail, since both nuclei present a prolate shape along the same z-direction of the perturbation given in Eq. (5.18), the reduction of the axial deformation induced by the pairing leads to an increase in the excitation energy of the GDR peak, analogously as one gets for a nucleus with a smaller size. The inclusion of pairing correlations appears hence rather important to perform realistic calculations to be compared with experimental results.

Regarding the peak associated with the PDR, we have already discussed how its IV projection is actually more sensitive to the surface oscillations and hence to the neutron skin thickness, which is not much affected by pairing correlations for the nuclei considered. However, the IS projection (left panels) of the PDR appears to be significantly influenced by the formation of Cooper pairs, since the corresponding peak in the strength function manifests a larger relative importance with respect to the case without pairing correlations, when one makes a TDHF+BCS calculation. In order to analyze the dependence of the IV PDR peak on the pairing, one should instead investigate nuclei which lie far from the closure of the shell, where the pairing gap is expected to be larger and can accordingly modify the surface diffuseness.

Work is in progress to explore the dipole response of these isotopes, with the aim to improve our understanding of the nature of the pygmy dipole resonance and, in connection with the experimental measurements, its dependence on the symmetry energy.

Conclusions

The purpose of this dissertation has been to study some general properties of nuclear many-body systems, ranging from infinite nuclear matter to finite nuclei. Our investigations have been focused in particular on nuclear systems with neutron excess, with the aim to get a deeper insight in the open issue which concerns the isospin dependence of the nuclear interaction.

The analysis has been concentrated especially on the behavior of nuclear matter at densities which lie below the saturation one. This density region allows in fact to address several nuclear phenomena, which involve surface effects in nuclei as well as clustering processes emerging in nuclear reactions and compact stellar objects.

Since we limit ourselves to aspects which manifest in the low density region of the phase diagram, our study has been devoted also to shed light on the impact of some relevant interparticle correlations which occur in fermionic system and are responsible for the superfluid phenomena: the pairing correlations.

Our goal has been therefore to examine the interplay of these correlations with the other terms of the effective interaction, usually introduced within the mean-field approximation to approach the nuclear quantal many-body problem.

Wide attention has been dedicated in our work to the role of the pairing interaction in the astrophysical setting of stellar matter, especially when the cooling process of proto-neutron stars is concerned. Our analysis evidences in fact important pairing effects on neutrino emissivity and specific heat, which are two of the key ingredients of the thermal evolution of a compact star.

On the one hand, superfluidity turns out to be responsible for a significant

modification of the neutrino emission, for suitable density, asymmetry and temperature conditions, in the simplifying approximation of homogeneous nuclear matter, which can be of interest for the evolution of neutron stars and supernovae explosion in the pre-bounce phase. In this context, focusing on neutral current neutrino scattering, we have generally observed an increase of the neutrino differential cross section in a paired and low-density nuclear medium, at least close to the spinodal border, where the matter is characterized by quite large density fluctuations. If these schematic treatment is confirmed by realistic simulations in stellar matter, it would imply an enhancement of neutrino trapping and a reduction in the energy flux carried by neutrinos. This behavior, essentially due to neutron-neutron pairing attraction which favour low-density clustering, leads to the emergence of new effects about the impact of superfluidity on the cooling mechanism.

On the other hand, in order to improve the understanding of the thermal evolution of compact stars, we have also presented a calculation of the specific heat in the inner crust of proto-neutron stars, within an approach based on cluster degrees of freedom, that considers the complete distribution of different nuclear species in thermal and β-equilibrium. This has produced the first modelization of stellar matter containing at the same time a statistical distribution of different nuclear clusters at finite temperature and pairing correlations in the unbound neutron component.

The resulting specific heat appears compatible with complete mean-field Hartree-Fock-Bogoliubov calculations, which assume a single cluster component. However, our study brings to light a strong influence of resonance population at moderate temperatures and in density regions close to the crust-core transition. This feature considerably affects the specific heat, since the cluster disappearence at high temperature does not lead in this model to a uniform gas of nucleons, as in other mean-field models, but allows the correlations to survive in the form of exotic neutron-rich resonant states at the limit of nuclear binding. Further work will be necessary to get to quantitative results including in-medium effects on the light cluster self-energies [153, 179], but our preliminary calculations in the semiclassical Extended Thomas-Fermi (ETF) formalism suggest that these effects will not drastically modify

the present picture.

Furthermore, in our work we show that an accurate treatment of β-equilibrium is important for a quantitative determination of the specific heat and consequently of the neutron star cooling curve.

As stressed before, our activity research has been focused mainly on isospin-asymmetric nuclear matter. Nuclear systems with neutron excess have in fact an essential role not only for astrophysics, but also in the context of nuclear structure.

In the second part of the thesis, we move therefore to the investigation of structure and small amplitude dynamics of neutron-rich nuclei, focusing on the mixed isoscalar-isovector character of their collective excitations. In particular, we have addressed some of the open questions concerning the nature of the low-lying isovector dipole strength experimentally observed in neutron-rich nuclei and known in literature as pygmy dipole resonance. Then, we have showed that the relative isoscalar-isovector weight of the different modes, as observed in the nuclear response, is determined by their intrinsic structure, as well as by the type of initial perturbation considered. As a result, within our framework, the low-lying strength arising in the isovector dipole response reveals that the corresponding excitations are essentially isoscalar-like, i.e., neutrons and protons oscillate in phase but with different amplitude. This mechanism induces however a finite, though small, isovector dipole moment oscillation, which is indeed revealed in the isovector strength.

By performing a systematic investigation over three mass regions and employing effective interactions which differ in the isovector channel, we have also explored the relation between the mixed isoscalar-isovector structure of the dipole collective modes and the density dependence of the symmetry energy. Since the latter quantity also affects the size of the neutron skin, our analysis has aimed at elucidating the possible connection between the strength observed, for selected nuclei, in the pygmy dipole response region and the corresponding neutron skin thickness. The results are moreover in a good qualitative agreement with full quantal Random Phase Approximation (RPA) calculations [40, 55, 75, 140, 189].

All these features have been investigated in a semi-classical as well as in

a quantal mean-field transport model. The latter has been also extended to include pairing correlations, in order to underline the effect of the formation of Cooper pair in shaping the dipole response of some neutron-rich systems.

One should remark that the findings presented here can be useful for further, systematic experiments searching for the pygmy dipole resonance and can be even extended to other collective modes, such as the recently observed pygmy quadrupole resonance (PQR) [139]. In particular, the features emerging from the analysis of the structure of the modes may help to select the best experimental conditions to probe this quite elusive mode. Moreover, a precise estimate of the strength acquired by the pygmy resonance in the dipole response can provide indications about the neutron skin extension, helping to better constrain yet unknown properties of the nuclear effective interaction, namely the density dependence of the symmetry energy.

Further developments to extend our work can be hence enviseged to get a deeper insight on the role of pairing and quantal effects in characterizing the collective excitations of neutron-rich nuclei.

As a perspective, also our understanding of the cooling process of compacts stars can be improved. Concerning our study on neutrino emissivity, first of all it is important to assess how our results modify accounting for the presence of a cluster component inside the nuclear medium. Moreover, one should explore other regions of the phase diagram, with the aim to address the supernova matter and, therefore, to investigate the effect of pairing correlations in more isospin-symmetric conditions. With regard to the realistic cluster model adopted so far to evaluate the specific heat, we would like to investigate in more details the sensitivity to the energy density functional employed. In such a way, we aspire to provide a better understanding of the mechanisms ruling the thermalization of the neutron stars and a more reliable simulation of the cooling process.

To conclude this dissertation, let us stress once more the challenging purpose tackled by our work and, generally speaking, by the current nuclear physics research, to make a bridge between the microscopic world and the astrophysical context. Despite of the huge number of orders of magnitude which separates these objects, nuclei and stars are indeed intimately con-

nected by the behavior of nuclear matter. Several features that have been widely discussed in the present thesis, such as effective interactions, EoS and pairing correlations, characterize indeed both systems. As a result, atomic nuclei and stellar objects turn out to be deeply bond.

Furthermore, the two studies appear strictly complementary. In our work, for example, we have addressed clustering phenomena and superfluidity effects in the stellar matter scenario, whereas the context of finite nuclei has been more exploited to explore the density dependence of the symmetry energy. However, one could concentrate on the role of the pairing effects also focusing on finite nuclear systems, not only looking at their structure and small amplitude dynamics as it has been partially done in our work, but also dealing with the study of nuclear reactions. Also, one should consider that constraints on the symmetry energy and, in general, on the nuclear EoS, are even imposed by astrophysical observations. Valuable informations in this sense may come also from the study of heavy ion collisions (HIC), which constitute one of the tools adopted to probe the symmetry energy [97] and the framework for the emergence of clusters in finite systems, as it is experimentally observed in multifragmentation processes [28].

Bibliography

[1] V. I. Abrosimov et al. *Nucl. Phys. A* 864.1 (2011).

[2] P. Adrich et al. *Phys. Rev. Lett.* 95.13 (2005).

[3] G. Audi and A. H. Wapstra. *Nucl. Phys. A* 565.1 (1993).

[4] G. Audi et al. *Chin. Phys. C* 36.12 (2012).

[5] T. Aumann and T. Nakamura. *Phys. Script.* T152 (2013).

[6] S. S. Avancini et al. *Phys. Rev. C* 85.3 (2012).

[7] S. Ayik, M. Colonna, and P. Chomaz. *Phys. Lett. B* 353.4 (1995).

[8] F. Aymard, F. Gulminelli, and J. Margueron. *Phys. Rev. C* 89.6 (2014).

[9] M. Baldo, E. E. Saperstein, and S. V. Tolokonnikov. *Nucl. Phys. A* 749 (2005).

[10] M. Baldo et al. *Phys. Rep.* 391 (2004).

[11] M. Baldo et al. *Phys. Rev. C* 89.4 (2014).

[12] R. Balina. *From Microphysics to Macrophysics.* Springer Berlin Heidelberg, 1991.

[13] V. Baran et al. *Phys. Rev. Lett.* 86.20 (2001).

[14] V. Baran et al. *Phys. Rep.* 410 (2005).

[15] V. Baran et al. *Phys. Rev. C* 85.5 (2012).

[16] V. Baran et al. *Phys. Rev. C* 88.4 (2013).

[17] J. Bardeen, L. N. Cooper, and J. R. Schrieffer. *Phys. Rev.* 108 (5 1957).

[18] F. Barranco et al. *Phys. Rev. C* 58.2 (1998).

[19] B. L. Berman and S. C. Fultz. *Rev. Mod. Phys.* 47.3 (1975).

[20] G. F. Bertsch and H. Esbensen. *Ann. Phys.* 209.2 (1991).

[21] H. A. Bethe and J. R. Wilson. *Astr. Jour.* 295 (1985).

[22] J. P. Blaizot and G. Ripka. *Quantum Theory of Finite Systems*. Cambridge, MA, 1986.

[23] N. N. Bogoliubov. *Sov. Phys. JETP* 34 (1958).

[24] D. Bohm and D. Pines. *Phys. Rev.* 92 (1953).

[25] A. Bonasera and F. Gulminelli. *Phys. Lett. B* 275.1 (1992).

[26] P. Bonche, H. Flocard, and P. H. Heenen. *Comp. Phys. Comm.* 171.1 (2005).

[27] P. Bonche, S. Koonin, and J. W. Negele. *Phys. Rev. C* 13 (1976).

[28] B. Borderie and M. F. Rivet. *Progr. Part. Nucl. Phys.* 61.2 (2008).

[29] M. Brack, C. M. Guet, and Håkansson H. B. *Phys. Rep.* 123.5 (1985).

[30] D. M. Brink, A. Dellafiore, and M. Di Toro. *Nucl. Phys. A* 456.2 (1986).

[31] K. A. Brueckner. *Phys. Rev.* 97 (1955).

[32] S. Burrello, M. Colonna, and F. Matera. *Phys. Rev. C* 89.5 (2014).

[33] S. Burrello, M. Colonna, and F. Matera. *Phys. Rev. C* 94 (2016).

[34] S. Burrello et al. *Phys. Rev. C* 92.5 (2015).

[35] A. Burrows. *Ann. Rev. Nucl. Part. Sci.* 40.1 (1990).

[36] A. Burrows and R. F. Sawyer. *Phys. Rev. C* 58.1 (1998).

[37] N. Buyukcizmeci et al. *Nucl. Phys. A* 907 (2013).

[38] L. G. Cao, G. Colò, and H. Sagawa. *Phys. Rev. C* 81.4 (2010).

[39] L. G. Cao, U. Lombardo, and P. Schuck. *Phys. Rev. C* 74.6 (2006).

[40] L. G. Cao et al. *Phys. Rev. C* 80 (6 2009).

[41] A. Carbone. *Phys. Rev. C* 81.4 (2010).

[42] W. B. Case. *Amer. Jour. Phys.* 76.10 (2008).

[43] N. Chamel. *Phys. Rev. C* 82.1 (2010).

[44] N. Chamel, S. Goriely, and J. M. Pearson. *Nucl. Phys. A* 812.1 (2008).

[45] N. Chamel et al. *Phys. Rev. C* 81.4 (2010).

[46] L. W. Chen, C. M. Ko, and B. A. Li. *Phys. Rev. Lett.* 94 (2005).

[47] P. Chomaz, M. Colonna, and J. Randrup. *Phys. Rep.* 389.5 (2004).

[48] P. Chomaz and F. Gulminelli. "Phase Transitions in Finite Systems". *Dynamics and Thermodynamics of Systems with Long-Range Interactions*. Springer Berlin Heidelberg, 2002.

[49] G. Colo et al. *Phys. Lett. B* 485.4 (2000).

[50] M. Colonna, V. Baran, and M. Di Toro. *Eur. Phys. Jour. A* 50.2 (2014).

[51] M. Colonna and F. Matera. *Phys. Rev. C* 71 (2005).

[52] F. C. L. Crespi et al. *Phys. Rev. Lett.* 113.1 (2014).

[53] M. D'Agostino et al. *Nucl. Phys. A* 699 (2002).

[54] P. Danielewicz and J. Lee. *Nucl. Phys. A* 818.1 (2009).

[55] I. Daoutidis and P. Ring. *Phys. Rev. C* 83.4 (2011).

[56] A. De Shalit and H. Feshbach. *Theor. Nucl. Phys.* New York: John Wiley, 1974.

[57] D. J. Dean and M. Hjorth-Jensen. *Rev. Mod. Phys.* 75 (2003).

[58] M. Di Toro and V. M. Kolomietz. *Zeit. Phys. A-Atomic Nuclei* 328.3 (1987).

[59] J. Dobaczewski, W. Nazarewicz, and P. G. Reinhard. *Nucl. Phys. A* 693 (2001).

[60] J. Dobaczewski et al. *Phys. Rev. C* 53.6 (1996).

[61] R. M. Dreizler and E. K. U. Gross. *Density Functional Theory: An Approach to the Quantum Many-Body Problem*. 1990.

[62] J. E. Drut, R. J. Furnstahl, and L. Platter. *Progr. Part. Nucl. Phys.* 64.1 (2010).

[63] C. Ducoin, P. Chomaz, and F. Gulminelli. *Nucl. Phys. A* 771 (2006).

[64] C. Ducoin, P. Chomaz, and F. Gulminelli. *Nucl. Phys. A* 789.1 (2007).

[65] C. Ducoin et al. *Phys. Rev. C* 83 (2011).

[66] T. Duguet, K. Bennaceur, and P. Bonche, eds. *Proceedins of the YITP Workshop on New Developments in Nuclear Self-Consistent Mean-Field Theories*. 112, Soryushiron Kenkyu, 2005.

[67] S. Ebata. *PhD thesis* (2011).

[68] S. Ebata et al. *Phys. Rev. C* 82 (2010).

[69] J. Endres et al. *Phys. Rev. C* 85.6 (2012).

[70] E. Fermi. *Z. Phys.* 48 (1928).

[71] L.A. Fetter and J.D. Walecka. *Quantum Theory of Many-Particle Systems,* New York: Dover Publications, Inc., 2003.

[72] M. Fortin et al. *Phys. Rev. C* 82 (2010).

[73] S. Frauendorf. *Fifty Years of Nuclear BCS: Pairing in Finite Systems.* (2013).

[74] S. Furusawa et al. *Astr. Jour.* 772.2 (2013).

[75] D. Gambacurta, M. Grasso, and F. Catara. *Phys. Rev. C* 81 (5 2010).

[76] E. Garrido et al. *Phys. Rev.* C60 (1999).

[77] G. Giuliani, H. Zheng, and A. Bonasera. *Progr. Part. Nucl. Phys.* 76 (2014).

[78] O. Y. Gnedin, D. G. Yakovlev, and A. Y. Potekhin. *Monthly Notices of the Royal Astronomical Society* 324.3 (2001).

[79] D. Gogny, G. Ripka, and M. Porneuf. "Nuclear self-consistent fields". *North-Holland* (1975).

[80] M. Goldhaber and E. Teller. *Phys. Rev.* 74.9 (1948).

[81] L.C. Gomes, J.D. Walecka, and V.F. Weisskopf. *Ann. Phys.* 3.3 (1958).

[82] S. Goriely, N. Chamel, and J. M. Pearson. *Phys. Rev. C* 82.3 (2010).

[83] S. Goriely, E. Khan, and M. Samyn. *Nucl. Phys. A* 739.3 (2004).

[84] M. Grasso and M. Urban. *Phys. Rev. A* 68.3 (2003).

[85] A. Guarnera, M. Colonna, and P. Chomaz. *Phys. Lett. B* 373.4 (1996).

[86] F. Gulminelli. *Physica Scripta* 2013.T152 (2013).

[87] F. Gulminelli. *Lectures on thermal properties of nuclear systems*. 2011.

[88] F. Gulminelli and Ad. R. Raduta. *Phys. Rev. C* 92.5 (2015).

[89] K. Hagino and H. Sagawa. *Nucl. Phys. A* 695.1 (2001).

[90] M. N. Harakeh and A. Woude. *Giant Resonances: fundamental high-frequency modes of nuclear excitation*. Vol. 24. Oxford University Press on Demand, 2001.

[91] T. Hartmann et al. *Phys. Rev. Lett.* 85.2 (2000).

[92] Y. Hashimoto. *Phys. Rev. C* 88 (3 2013).

[93] S. Heckel, P. P. Schneider, and A. Sedrakian. *Phys. Rev. C* 80.1 (2009).

[94] M. Hempel and J. Schaffner-Bielich. *Nucl. Phys. A* 837.3 (2010).

[95] C. J. Horowitz, M. A. Perez-Garcia, and J. Piekarewicz. *Phys. Rev. C* 69.4 (2004).

[96] C. J. Horowitz et al. *Phys. Rev. C* 86.6 (2012).

[97] C. J. Horowitz et al. *Jour. Phys. G: Nucl. Part. Phys.* 41.9 (2014).

[98] K. Huang. "Statistical mechanics". *New York—London* (1963).

[99] N. Iwamoto and C. J. Pethick. *Phys. Rev. D* 25.2 (1982).

[100] H. T. Janka et al. *Phys. Rep.* 442.1 (2007).

[101] L. P. Kadanoff and G. A. Baym. *Quantum statistical mechanics*. Benjamin, 1962.

[102] E. Khan et al. *Phys. Rev. C* 66.2 (2002).

[103] K. H. Kim, T. Otsuka, and P. Bonche. *Jour. Phys. G: Nucl. Part. Phys.* 23.10 (1997).

[104] A. Klimkiewicz et al. *Phys. Rev. C* 76.5 (2007).

[105] T. Kondo et al. *Phys. Rev. C* 86.1 (2012).

[106] S. Kowalski et al. *Phys. Rev. C* 75 (2007).

[107] D. Lacroix. *Review of mean-field theory: lectures.* 2011.

[108] L. D. Landau. *Sov. Phys. JETP* 3.6 (1957).

[109] L. D. Landau and E. M. Lifshitz. "Statistical Physics, Part 1: Volume 5" (1980).

[110] J. M. Lattimer and M. Prakash. *Phys. Rep.* 442.1 (2007).

[111] J. M. Lattimer and F. D. Swesty. *Nucl. Phys. A* 535.2 (1991).

[112] J. M. Lattimer et al. *Astr. Jour.* 425 (1994).

[113] B. A. Li, L. W. Chen, and C. M. Ko. *Phys. Rep.* 464.4 (2008).

[114] E. Litvinova et al. *Phys. Rev. C* 79.5 (2009).

[115] U. Lombardo and H. J. Schulze. *Physics of Neutron Star Interiors.* Springer, 2001.

[116] C. Losa et al. *Phys. Rev. C* 81.6 (2010).

[117] Y. W. Lui et al. *Nucl. Phys. A* 731 (2004).

[118] J. Margueron, J. Navarro, and P. Blottiau. *Phys. Rev. C* 70.2 (2004).

[119] G. Martínez-Pinedo. *Phys. Rev. Lett.* 109.25 (2012).

[120] R. Mayle, J. R. Wilson, and D. N. Schramm. *Astr. Jour.* 318 (1987).

[121] A. B. Migdal. *Nucl. Phys.* 13 (1959).

[122] A.B. Migdal and S.A. Moszkowski. *Amer. Jour. Phys.* 36.9 (1968).

[123] W. D. Myers. *Atomic Data and Nuclear Data Tables* 17 (1976).

[124] W. D. Myers and W. J. Swiatecki. *Nucl. Phys. A* 336.2 (1980).

[125] J. W. Negele and D. Vautherin. *Nucl. Phys. A* 207.2 (1973).

[126] V. O. Nesterenko et al. 74 (2006).

[127] A. Nogga, H. Kamada, and W. Glöckle. *Phys. Rev. Lett.* 85 (5 2000).

[128] J. R. Oppenheimer and G. M. Volkoff. *Phys. Rev.* 55.4 (1939).

[129] N. Paar et al. *Phys. Rev. C* 67.3 (2003).

[130] N. Paar et al. *Rep. Progr. Phys.* 70.5 (2007).

[131] D. Page. *Fifty Years of Nuclear BCS: Pairing in Finite Systems* (2013).

[132] D. Page et al. *Astr. Jour. Suppl. Ser.* 155 (2004).

[133] D. Page et al. *arXiv:1302.6626* (2013).

[134] H. Pais, W. G. Newton, and J. R. Stone. *Phys. Rev. C* 90.6 (2014).

[135] P. Papakonstantinou et al. *Phys. Rev. C* 88.4 (2013).

[136] R. G. Parr and W. Yang. *Density Functional Methods of Atoms and Molecules*. 1989.

[137] A. Pastore. *Phys. Rev. C* 91.1 (2015).

[138] J. M. Pearson et al. *Phys. Rev. C* 85.6 (2012).

[139] L. Pellegri et al. *Phys. Rev. C* 92.1 (2015).

[140] J. Piekarewicz. *Phys. Rev. C* 73.4 (2006).

[141] J. Piekarewicz et al. *Phys. Rev. C* 85 (2012).

[142] D. Pines and P. Nozières. *The Theory of Quantum Liquids: Normal Fermi Liquids*. Vol. 1. WA Benjamin, 1966.

[143] P. M. Pizzochero et al. *Astr. Jour.* 569.1 (2002).

[144] A. Y. Potekhin, J. A. Pons, and D. Page. *Sp. Sci. Rev.* 191.1-4 (2015).

[145] M. Prakash et al. *Physics of neutron star interiors*. Springer, 2001.

[146] A. R. Raduta and F. Gulminelli. *Phys. Rev. C* 82 (6 2010).

[147] Ad. R. Raduta, F. Aymard, and F. Gulminelli. *Eur. Phys. Jour. A* 50.2 (2014).

[148] Ad. R. Raduta and F. Gulminelli. *Phys. Rev. C* 82.6 (2010).

[149] P. G. Reinhard et al. *Phys. Rev. E* 73.3 (2006).

[150] P. Ring and P. Schuck. *The Nuclear Many-Body Problem,* Berlino: Springer-Verlag, 1980.

[151] X. Roca-Maza, G. Colò, and H. Sagawa. *Phys. Rev. C* 86.3 (2012).

[152] X. Roca-Maza et al. *Phys. Rev. C* 85.2 (2012).

[153] G. Röpke et al. *Phys. Rev. C* 88.2 (2013).

[154] D. M. Rossi et al. *Phys. Rev. Lett.* 111.24 (2013).

[155] P. Russotto et al. *Phys. Lett. B* 697.5 (2011).

[156] N. Ryezayeva et al. *Phys. Rev. Lett.* 89.27 (2002).

[157] M. Samyn, S. Goriely, and J. M. Pearson. *Nucl. Phys. A* 725.0 (2003).

[158] N. Sandulescu, N. Van Giai, and R. J. Liotta. *Phys. Rev. C* 69.4 (2004).

[159] D. Sarchi, P. F. Bortignon, and G. Colo. *Phys. Lett. B* 601.1 (2004).

[160] D. Savran, T. Aumann, and A. Zilges. *Progr. Part. Nucl. Phys.* 70 (2013).

[161] G. Scamps. PhD thesis. Université de Caen, 2014.

[162] G. Scamps and D. Lacroix. *Phys. Rev. C* 87 (2013).

[163] G. Scamps and D. Lacroix. *EPJ Web of Conferences*. Vol. 86. EDP Sciences. 2015.

[164] A. Sedrakian and U. Lombardo. *Phys. Rev. Lett.* 84.4 (2000).

[165] A. V. Senatorov and D. N. Voskresensky. *Phys. Lett. B* 184.2-3 (1987).

[166] S. Shlomo and V. M. Kolomietz. *Rept. Prog. Phys.* 68.1 (2004).

[167] P. J. Siemens. *Nature* 305 (1983).

[168] C. Simenel, P. Chomaz, and G. De France. *Phys. Rev. Lett.* 86.14 (2001).

[169] Simenel, C. *Eur. Phys. Jour. A* 48.11 (2012).

[170] T. H. R. Skyrme. *Nucl. Phys.* 9.4 (1958).

[171] A. W. Steiner and other. *Phys. Rep.* 411.6 (2005).

[172] H. Steinwedel, J. H. D. Jensen, and P. Jensen. *Phys. Rev.* 79.6 (1950).

[173] Y. Suzuki, K. Ikeda, and H. Sato. *Progr. Theor. Phys.* 83.2 (1990).

[174] A. Tamii et al. *Phys. Rev. Lett.* 107.6 (2011).

[175] J. Terasaki and J. Engel. *Phys. Rev. C* 74.4 (2006).

[176] L. H. Thomas. *Mathematical Proceedings of the Cambridge Philosophical Society* 23 (Jan. 1927).

[177] M. B. Tsang et al. *Phys. Rev. C* 86.1 (2012).

[178] N. Tsoneva et al. *Phys. Rev. C* 91.4 (2015).

[179] S. Typel et al. *Phys. Rev. C* 81.1 (2010).

[180] S. Typel et al. *Eur. Phys. J. A* 50.2 (2014).

[181] M. Uchida et al. *Phys. Rev. C* 69 (5 2004).

[182] M. Urban. *Phys. Rev. C* 85 (2012).

[183] M. Urban and P. Schuck. *Phys. Rev. A* 73.1 (2006).

[184] P. Van Isacker, M. A. Nagarajan, and D. D. Warner. *Phys. Rev. C* 45.1 (1992).

[185] D. Vautherin. *Phys. Rev. C* 7 (1973).

[186] D. Vautherin and D. M. Brink. *Phys. Rev. C* 5 (1972).

[187] A. A. Vlasov. *Sov. Phys. Usp.* 10.6 (1968).

[188] T. Von Egidy and D. Bucurescu. *Phys. Rev. C* 72.4 (2005).

[189] D. Vretenar and other. *Phys. Rev. C* 63 (4 2001).

[190] M. Warda et al. *Phys. Rev. C* 80.2 (2009).

[191] G. Watanabe, K. Iida, and K. Sato. *Nucl. Phys. A* 676.1 (2000).

[192] G. Watanabe et al. *Phys. Rev. C* 68.3 (2003).

[193] H. Weyl. *The theory of groups and quantum mechanics*. Courier Corporation, 1950.

[194] G. C. Wick. *Phys. Rev.* 80 (1950).

[195] O. Wieland and A. Bracco. *Progr. Part. Nucl. Phys.* 66.2 (2011).

[196] O. Wieland et al. *Phys. Rev. Lett.* 102.9 (2009).

[197] R. B. Wiringa. *Rev. Mod. Phys.* 65 (1 1993).

[198] R. B. Wiringa, V. Fiks, and A. Fabrocini. *Phys. Rev. C* 38.2 (1988).

[199] C. Wong. *Phys. Rev. C* 25.3 (1982).

[200] E. Yüksel, E. Khan, and K. Bozkurt. *Nucl. Phys. A* 877 (2012).

[201] Z. Zhang and L. Chen. *Phys. Rev. C* 90.6 (2014).

[202] H. Zheng et al. *Phys. Rev. C* 94 (2016).

Appendix A

Appendix

A.1 Hartree-Fock energy

Starting by eq. Eq. (1.13) and by exploiting the Wick's theorem and the antisymmetrization of the two-body interaction, it is trivial to get

$$\begin{aligned}
E^{\mathrm{HF}}[\rho] &= \sum_{ij} T_{ij}\rho_{ji} + \frac{1}{4}\sum_{i,j,k,l} \bar{V}_{ijkl}\left(\rho_{lj}\rho_{ki} - \rho_{li}\rho_{kj}\right) \\
&= \sum_{ij} T_{ij}\rho_{ji} + \frac{1}{4}\sum_{i,j,k,l} \bar{V}_{ijkl}\rho_{lj}\rho_{ki} + \frac{1}{4}\sum_{i,j,k,l} \bar{V}_{ijlk}\rho_{li}\rho_{kj} \\
&= \sum_{ij} T_{ij}\rho_{ji} + \frac{1}{4}\sum_{i,j,k,l} \bar{V}_{ijkl}\rho_{lj}\rho_{ki} + \frac{1}{4}\sum_{i,j,k,l} \bar{V}_{ijkl}\rho_{ki}\rho_{lj} \\
&= \sum_{ij} T_{ij}\rho_{ji} + \frac{1}{2}\sum_{i,j,k,l} \rho_{ki}\bar{V}_{ijkl}\rho_{lj} \\
&= \sum_{ij} T_{ij}\rho_{ji} + \frac{1}{2}\sum_{i,j,k,l} \rho_{ji}\bar{V}_{ikjl}\rho_{lk} \\
&= \sum_{ij} \left(T_{ij} + \frac{1}{2}U_{ij}\right)\rho_{ji}, \qquad \text{(A.1)}
\end{aligned}$$

which, bearing in mind the definition of the mean-field potential given in Eq. (1.15), is the result quoted in Eq. (1.14).

A.2 TDHF equations

Bearing in mind that the hamiltonian operator $\hat{H}$ can be represented as in Eq. (1.11), the equation of motion Eq. (1.23) requires to evaluate the expectation values of the following algebraic commutators:

$$\left[\hat{a}_j^\dagger \hat{a}_i, \hat{a}_m^\dagger \hat{a}_n\right] \qquad \left[\hat{a}_j^\dagger \hat{a}_i, \hat{a}_k^\dagger \hat{a}_l^\dagger \hat{a}_m \hat{a}_n\right], \tag{A.2}$$

which are related to the kinetic energy term and to the potential part of $\hat{H}$, respectively.

Let us consider only the first contribution, since the derivation for the second one is longer but altogether similar. By taking into account the following relation which applies for the algebraic commutator:

$$\left[\hat{A}\hat{B}, \hat{C}\hat{D}\right] = \hat{A}\left[\hat{B}, \hat{C}\right]\hat{D} + \hat{A}\hat{C}\left[\hat{B}, \hat{D}\right] + \left[\hat{A}, \hat{C}\right]\hat{B}\hat{D} + \hat{C}\left[\hat{A}, \hat{D}\right]\hat{B} \tag{A.3}$$

and reminding, together with the anti-commutation relations for the fermionic operator, that

$$\left[\hat{A}, \hat{B}\right] = 2\hat{A}\hat{B} - \left\{\hat{A}, \hat{B}\right\}, \tag{A.4}$$

one can easily carry out this simple algebra:

$$\begin{aligned}
\left[\hat{a}_j^\dagger \hat{a}_i, \hat{a}_m^\dagger \hat{a}_n\right] &= \hat{a}_j^\dagger \left[\hat{a}_i, \hat{a}_m^\dagger\right] \hat{a}_n + \hat{a}_j^\dagger \hat{a}_m^\dagger \left[\hat{a}_i, \hat{a}_n\right] + \left[\hat{a}_j^\dagger, \hat{a}_m^\dagger\right] \hat{a}_i \hat{a}_n + \hat{a}_m^\dagger \left[\hat{a}_j^\dagger, \hat{a}_n\right] \hat{a}_i \\
&= 2\hat{a}_j^\dagger \hat{a}_i \hat{a}_m^\dagger \hat{a}_n - \hat{a}_j^\dagger \hat{a}_n \delta_{im} + 2\hat{a}_j^\dagger \hat{a}_m^\dagger \hat{a}_i \hat{a}_n + 2\hat{a}_j^\dagger \hat{a}_m^\dagger \hat{a}_i \hat{a}_n + 2\hat{a}_m^\dagger \hat{a}_j^\dagger \hat{a}_n \hat{a}_i - \hat{a}_m^\dagger \hat{a}_i \delta_{jn} \\
&= -2\hat{a}_j^\dagger \hat{a}_m^\dagger \hat{a}_i \hat{a}_n + 2\hat{a}_j^\dagger \hat{a}_n \delta_{im} - \hat{a}_j^\dagger \hat{a}_n \delta_{im} + 6\hat{a}_j^\dagger \hat{a}_m^\dagger \hat{a}_i \hat{a}_n - \hat{a}_m^\dagger \hat{a}_i \delta_{jn} \\
&= 4\hat{a}_j^\dagger \hat{a}_m^\dagger \hat{a}_i \hat{a}_n + \hat{a}_j^\dagger \hat{a}_n \delta_{im} - \hat{a}_m^\dagger \hat{a}_i \delta_{jn}.
\end{aligned} \tag{A.5}$$

Therefore, by denoting the expectation value given in Eq. (1.23) as $\left\langle \left[\hat{a}_j^\dagger \hat{a}_i, \hat{H}\right] \right\rangle_\Psi$, one finally get:

$$\left\langle \left[\hat{a}_j^\dagger \hat{a}_i, \hat{a}_m^\dagger \hat{a}_n\right] \right\rangle_\Psi = \left\langle \hat{a}_j^\dagger \hat{a}_n \right\rangle_\Psi \delta_{im} - \left\langle \hat{a}_m^\dagger \hat{a}_i \right\rangle_\Psi \delta_{jn}, \tag{A.6}$$

since the other contribution vanishes.

In a completely similar way, one then also finds that the second commu-

tator can be written like

$$\left\langle \left[\hat{a}_j^\dagger \hat{a}_i, \hat{a}_k^\dagger \hat{a}_l^\dagger \hat{a}_n \hat{a}_m\right] \right\rangle_\Psi = \left\langle \hat{a}_j^\dagger \hat{a}_l^\dagger \hat{a}_n \hat{a}_m \right\rangle_\Psi \delta_{ik} - \left\langle \hat{a}_j^\dagger \hat{a}_k^\dagger \hat{a}_n \hat{a}_m \right\rangle_\Psi \delta_{il} - \left\langle \hat{a}_k^\dagger \hat{a}_l^\dagger \hat{a}_i \hat{a}_m \right\rangle_\Psi \delta_{jn} + \left\langle \hat{a}_k^\dagger \hat{a}_l^\dagger \hat{a}_i \hat{a}_n \right\rangle_\Psi \delta_{jm}. \tag{A.7}$$

By inserting now the formulas obtained in Eq. (A.5) and Eq. (A.7) in the equation Eq. (1.23), one suddenly gets for the first contribution:

$$\begin{aligned} \left[i\hbar\dot{\rho}_{ij}(t)\right]_1 &= \sum_{m,n} \left(T_{mn}\rho_{nj}\delta_{im} - \rho_{im}T_{mn}\delta_{jn}\right) \\ &= \sum_n T_{in}\rho_{nj} - \sum_m \rho_{im}T_{mj} \end{aligned} \tag{A.8}$$

while for the second one, as in Appendix A.1, again the application of the Wick's theorem and the antisymmetrization of the two-body interaction allow to achieve

$$\begin{aligned} \left[i\hbar\dot{\rho}_{ij}(t)\right]_2 &= \frac{1}{4}\left[\sum_{l,m,n} \bar{V}_{ilmn}\left(\rho_{nl}\rho_{mj} - \rho_{ml}\rho_{nj}\right)\right] - \frac{1}{4}\left[\sum_{k,m,n} \bar{V}_{kimn}\left(\rho_{nk}\rho_{mj} - \rho_{mk}\rho_{nj}\right)\right] \\ &\quad - \frac{1}{4}\left[\sum_{k,l,m} \bar{V}_{klmj}\left(\rho_{il}\rho_{mk} - \rho_{ik}\rho_{ml}\right)\right] + \frac{1}{4}\left[\sum_{k,l,n} \bar{V}_{kljn}\left(\rho_{il}\rho_{nk} - \rho_{ik}\rho_{nl}\right)\right] \\ &= \frac{1}{2}\left[\sum_{l,m,n} \bar{V}_{ilmn}\left(\rho_{nl}\rho_{mj} - \rho_{ml}\rho_{nj}\right)\right] - \frac{1}{2}\left[\sum_{k,l,m} \bar{V}_{klmj}\left(\rho_{il}\rho_{mk} - \rho_{ik}\rho_{ml}\right)\right] \\ &= \sum_n U_{in}\rho_{nj} - \sum_m \rho_{im}U_{mj}, \end{aligned} \tag{A.9}$$

whereas in the last line it has been introduced the definition of mean-field potential given in Eq. (1.15). By exploting the results deduced in Eq. (A.8) and Eq. (A.9), one finally gets the TDHF equations:

$$i\hbar\dot{\rho}_{ij}(t) = \sum_m \left[\left(T_{im} + U_{im}\right)\rho_{mj} - \rho_{im}\left(T_{mj} + U_{mj}\right)\right] = \left[h, \rho\right]_{ij}. \tag{A.10}$$

A.3 Vlasov equation

The Wigner function, as given in the r-basis in Eq. (1.45), can be also equivalently defined in terms of matrix elements of the density operator in the momentum basis as:

$$f(\mathbf{r},\mathbf{p}) = \frac{1}{h^3}\int e^{+i\frac{\mathbf{q}\cdot\mathbf{r}}{\hbar}}\,\langle \mathbf{p}+\frac{\mathbf{q}}{2}|\,\hat{\rho}\,|\mathbf{p}-\frac{\mathbf{q}}{2}\rangle\,d\mathbf{q}. \tag{A.11}$$

With this definition, the one-body contribution of the TDHF equation (Eq. (1.24)) can be written as:

$$\begin{aligned}
\left(\frac{\partial f}{\partial t}\right)_1 &= \frac{1}{i\hbar}\frac{1}{h^3}\int e^{-i\frac{\mathbf{p}\cdot\mathbf{R}}{\hbar}}\,\langle \mathbf{r}+\frac{\mathbf{R}}{2}|\left[\hat{T},\hat{\rho}\right]|\mathbf{r}-\frac{\mathbf{R}}{2}\rangle\,d\mathbf{R}\\
&= \frac{1}{i\hbar}\frac{1}{h^3}\int e^{+i\frac{\mathbf{q}\cdot\mathbf{r}}{\hbar}}\,\langle \mathbf{p}+\frac{\mathbf{q}}{2}|\left[\hat{T},\hat{\rho}\right]|\mathbf{p}-\frac{\mathbf{q}}{2}\rangle\,d\mathbf{q}\\
&= \frac{1}{i\hbar}\frac{1}{h^3}\int e^{+i\frac{\mathbf{q}\cdot\mathbf{r}}{\hbar}}\,\langle \mathbf{p}+\frac{\mathbf{q}}{2}|\left[\hat{T}\hat{\rho}-\hat{\rho}\hat{T}\right]|\mathbf{p}-\frac{\mathbf{q}}{2}\rangle\,d\mathbf{q}\\
&= \frac{1}{i\hbar}\frac{1}{h^3}\int e^{+i\frac{\mathbf{q}\cdot\mathbf{r}}{\hbar}}\left[\frac{(\mathbf{p}+\frac{\mathbf{q}}{2})^2}{2m}-\frac{(\mathbf{p}-\frac{\mathbf{q}}{2})^2}{2m}\right]\langle \mathbf{p}+\frac{\mathbf{q}}{2}|\,\hat{\rho}\,|\mathbf{p}-\frac{\mathbf{q}}{2}\rangle\,d\mathbf{q}\\
&= \frac{1}{i\hbar}\frac{1}{h^3}\int e^{+i\frac{\mathbf{q}\cdot\mathbf{r}}{\hbar}}\frac{\mathbf{p}\cdot\mathbf{q}}{m}\,\langle \mathbf{p}+\frac{\mathbf{q}}{2}|\,\hat{\rho}\,|\mathbf{p}-\frac{\mathbf{q}}{2}\rangle\,d\mathbf{q}\\
&= \frac{\mathbf{p}}{m}\cdot\frac{1}{i\hbar}\frac{1}{h^3}\int e^{+i\frac{\mathbf{q}\cdot\mathbf{r}}{\hbar}}\mathbf{q}\,\langle \mathbf{p}+\frac{\mathbf{q}}{2}|\,\hat{\rho}\,|\mathbf{p}-\frac{\mathbf{q}}{2}\rangle\,d\mathbf{q}\\
&= -\frac{\mathbf{p}}{m}\cdot\nabla_{\mathbf{r}} f.
\end{aligned} \tag{A.12}$$

At the same time, the two-body contribution is easily evaluated employing these simple algebraic calculations:

$$\begin{aligned}
\left(\frac{\partial f}{\partial t}\right)_2 &= \frac{1}{i\hbar}\frac{1}{h^3}\int e^{-i\frac{\mathbf{p}\cdot\mathbf{R}}{\hbar}}\,\langle \mathbf{r}+\frac{\mathbf{R}}{2}|\left[\hat{U},\hat{\rho}\right]|\mathbf{r}-\frac{\mathbf{R}}{2}\rangle\,d\mathbf{R}\\
&= \frac{1}{i\hbar}\frac{1}{h^3}\int e^{-i\frac{\mathbf{p}\cdot\mathbf{R}}{\hbar}}\,\langle \mathbf{r}+\frac{\mathbf{R}}{2}|\left[\hat{U}\hat{\rho}-\hat{\rho}\hat{U}\right]|\mathbf{r}-\frac{\mathbf{R}}{2}\rangle\,d\mathbf{R}\\
&= \frac{1}{i\hbar}\frac{1}{h^3}\int e^{-i\frac{\mathbf{p}\cdot\mathbf{R}}{\hbar}}\left[U\left(\mathbf{r}+\frac{\mathbf{R}}{2}\right)-U\left(\mathbf{r}-\frac{\mathbf{R}}{2}\right)\right]\langle \mathbf{r}+\frac{\mathbf{R}}{2}|\,\hat{\rho}\,|\mathbf{r}-\frac{\mathbf{R}}{2}\rangle\,d\mathbf{R}\\
&= \sum_{n=0}^{\infty}\frac{1}{n!}\frac{\partial U^n(\mathbf{r})}{\partial \mathbf{r}^n}\frac{1}{i\hbar}\frac{1}{h^3}\int e^{-i\frac{\mathbf{p}\cdot\mathbf{R}}{\hbar}}\left[\left(\frac{\mathbf{R}}{2}\right)^n-\left(-\frac{\mathbf{R}}{2}\right)^n\right]\langle \mathbf{r}+\frac{\mathbf{R}}{2}|\,\hat{\rho}\,|\mathbf{r}-\frac{\mathbf{R}}{2}\rangle\,d\mathbf{R}
\end{aligned}$$

$$
\begin{aligned}
&= \sum_{l=0}^{\infty} \frac{1}{(2l+1)!} \frac{\partial^{2l+1} U}{\partial \mathbf{r}^{2l+1}} \frac{1}{i\hbar} \frac{1}{h^3} \int e^{-i\frac{\mathbf{p}\cdot\mathbf{R}}{\hbar}} \frac{\mathbf{R}^{2l+1}}{2^{2l}} \langle \mathbf{r} + \frac{\mathbf{R}}{2} | \, \hat{\rho} \, | \mathbf{r} - \frac{\mathbf{R}}{2} \rangle \, d\mathbf{R} \\
&= \frac{2}{\hbar} \sum_{l=0}^{\infty} \frac{(-1)^l}{(2l+1)!} \left(\frac{\hbar}{2} \right)^{2l+1} \frac{\partial^{2l+1} U}{\partial \mathbf{r}^{2l+1}} \frac{\partial^{2l+1} f}{\partial \mathbf{p}^{2l+1}} \\
&= \frac{2}{\hbar} \sin \left(\frac{\hbar}{2} \nabla_{\mathbf{r}} U \cdot \nabla_{\mathbf{p}} f \right) \xrightarrow{\hbar \to 0} \nabla_{\mathbf{r}} U \cdot \nabla_{\mathbf{p}} f. \qquad \text{(A.13)}
\end{aligned}
$$

The sum of the two contributions derived in Eqs. (A.12) and (A.13) leads to the Vlasov equation (Eq. (1.50)), as one wants to proof.

A.4 TDHFB equations

The temporal evolution of the normal density $\hat{\rho}$ as determined in Eq. (A.10) in case of TDHF theory modifies now to take into account the contribution of the abnormal density $\hat{\kappa}$, defined in Eq. (2.8). In particular, while the kinetic part Eq. (A.8) is not affected by the pairing density, one should notice that it is possible to make other contractions which involve $\hat{\kappa}$ in applying the Wick's theorem to the commutator in Eq. (A.7). So the potential term Eq. (A.9) modifies now in this way:

$$
\begin{aligned}
\left[i\hbar \dot{\rho}_{ij}(t) \right]_2 &= \frac{1}{2} \left[\sum_{l,m,n} \bar{V}_{ilmn} \left(\rho_{nl} \rho_{mj} - \rho_{ml} \rho_{nj} - \kappa_{mn} \kappa^*_{jl} \right) \right] \\
&\quad - \frac{1}{2} \left[\sum_{k,l,m} \bar{V}_{klmj} \left(\rho_{il} \rho_{mk} - \rho_{ik} \rho_{ml} - \kappa_{mi} \kappa^*_{kl} \right) \right] \\
&= \sum_{n} \left(U_{in} \rho_{nj} + \Delta_{in} \kappa^*_{jn} \right) - \sum_{m} \left(\rho_{im} U_{mj} + \kappa_{mi} \Delta^*_{mj} \right), \qquad \text{(A.14)}
\end{aligned}
$$

where the definition of $\hat{\Delta}$ expressed in Eq. (2.11) has been used. Since the matrix κ_{ij} is antisymmetric, definitively it gets:

$$
\begin{aligned}
i\hbar \dot{\rho}_{ij}(t) &= \sum_{m} \left[\left(T_{im} + U_{im} \right) \rho_{mj} - \rho_{im} \left(T_{mj} + U_{mj} \right) \right] - \Delta_{im} \kappa^*_{mj} + \kappa_{im} \Delta^*_{mj} \\
&= \left[h, \rho \right]_{ij} + \kappa \Delta^* - \Delta \kappa^*, \qquad \text{(A.15)}
\end{aligned}
$$

which is exactly the first of the TDHFB equations written in Eq. (2.28). The equation of motion for the abnormal density $\hat{\kappa}$ requires instead to evaluate, analogously as it has been done in Appendix A.2 for the normal density contributions, these algebraic commutators:

$$\left[\hat{a}_j\hat{a}_i, \hat{a}^\dagger_m\hat{a}_n\right] \qquad\qquad \left[\hat{a}_j\hat{a}_i, \hat{a}^\dagger_k\hat{a}^\dagger_l\hat{a}_m\hat{a}_n\right], \tag{A.16}$$

whose expectation values are given by these formulas:

$$\begin{aligned}
\left\langle\left[\hat{a}_j\hat{a}_i, \hat{a}^\dagger_m\hat{a}_n\right]\right\rangle_\Psi &= \langle\hat{a}_j\hat{a}_n\rangle_\Psi\,\delta_{im} - \langle\hat{a}_i\hat{a}_n\rangle_\Psi\,\delta_{jm} \\
\left\langle\left[\hat{a}_j\hat{a}_i, \hat{a}^\dagger_k\hat{a}^\dagger_l\hat{a}_n\hat{a}_m\right]\right\rangle_\Psi &= \left\langle\hat{a}^\dagger_k\hat{a}_j\hat{a}_n\hat{a}_m\right\rangle_\Psi\delta_{il} - \left\langle\hat{a}^\dagger_k\hat{a}_i\hat{a}_n\hat{a}_m\right\rangle_\Psi\delta_{jl} \\
&\quad + \left\langle\hat{a}_j\hat{a}^\dagger_l\hat{a}_n\hat{a}_m\right\rangle_\Psi\delta_{ik} - \left\langle\hat{a}_i\hat{a}^\dagger_l\hat{a}_n\hat{a}_m\right\rangle_\Psi\delta_{jk}.
\end{aligned} \tag{A.17}$$

The two-body contribution on the equation of motion for $\hat{\kappa}$ results to be given therefore by:

$$\begin{aligned}
i\hbar\dot{\kappa}_{ij}(t)_2 &= \sum_m \left[(T_{im}+U_{im})\,\kappa_{mj} + \kappa_{im}\,(T_{mj}+U_{mj}) + \Delta_{im}\left(\delta_{mj}-\rho^*_{mj}\right) - \rho_{im}\Delta_{mj}\right] \\
&= h\kappa + \kappa h^* + \Delta\,(\mathbb{1}-\rho^*) - \rho\Delta,
\end{aligned} \tag{A.18}$$

which is nothing but the second equation of the Eq. (2.29).

A.5 Single particle energy functional

The single particle energy ϵ_q, for each nuclear species $q = n, p$, can be defined as the distributional derivative of the energy density functional $\mathcal{E}$ introduced in Eq. (1.37) with respect to the distribution fuction f_q:

$$\epsilon_q \equiv \mathcal{A}\,\frac{D\mathcal{E}[f_n, f_p]}{Df_q}, \tag{A.19}$$

where $\mathcal{A}$ is a suitable constant, which will be fixed later. By exploiting the following expressions for the single particle density ρ_q and kinetic energy density τ_q, which manifest the dependence of these quantities on the distribution

function f_q:

$$\rho_q[f_q] = \int \frac{d^3\mathbf{p}}{h^3/2} f_q(\mathbf{p}) \tag{A.20}$$

$$\tau_q[f_q] = \frac{1}{\hbar^2} \int \frac{d^3\mathbf{p}}{h^3/2} p^2 f_q(\mathbf{p}) \qquad q = n, p, \tag{A.21}$$

one can easily evaluate the single particle energy functional as

$$\begin{aligned}
\epsilon_q &= \mathcal{A} \sum_{q'=n,p} \left[\frac{\partial \mathcal{E}}{\partial \rho_{q'}} \frac{D\rho_{q'}}{Df_q} + \frac{\partial \mathcal{E}}{\partial \tau_{q'}} \frac{D\tau_{q'}}{Df_q} \right] \\
&= \mathcal{A} \sum_{q'=n,p} \left[\frac{\partial \mathcal{E}}{\partial \rho_{q'}} \delta_{qq'} \int \frac{d^3\mathbf{p}'}{h^3/2} \delta(\mathbf{p} - \mathbf{p}') + \frac{\partial \mathcal{E}}{\partial \tau_{q'}} \delta_{qq'} \frac{1}{\hbar^2} \int \frac{d^3\mathbf{p}'}{h^3/2} p'^2 \delta(\mathbf{p} - \mathbf{p}') \right] \\
&= \frac{\partial \mathcal{E}}{\partial \rho_q} + \frac{p^2}{\hbar^2} \frac{\partial \mathcal{E}}{\partial \tau_q},
\end{aligned} \tag{A.22}$$

having adopted for the δ-function the normalization:

$$\int \frac{d^3\mathbf{p}'}{h^3/2} \delta(\mathbf{p} - \mathbf{p}') = \frac{1}{\mathcal{A}}. \tag{A.23}$$

For sake of simplicity, let us neglect the finite terms in $\mathcal{E}$, since their contribution is straightforwardly evaluated. Under this assumption, the energy density functional for the (asymmetric) nuclear matter case can be written as:

$$\mathcal{E}(\rho, \rho_3, \tau, \tau_3) = \mathcal{K} + \mathcal{E}_{pot} + \mathcal{E}_{eff}, \tag{A.24}$$

where we isolate the momentum dependent contribution $\mathcal{E}_{eff}$ from the remaining part $\mathcal{E}_{pot} = \mathcal{E}_0 + \mathcal{E}_3$. For the kinetic term, we have a contribution only by the derivative with respect to the kinetic energy density, so:

$$\varepsilon \equiv \mathcal{A} \frac{D\mathcal{K}}{Df_q} = \frac{p^2}{\hbar^2} \frac{\partial \mathcal{K}}{\partial \tau_q} = \frac{p^2}{\hbar^2} \frac{\hbar^2}{2m} = \frac{p^2}{2m} \tag{A.25}$$

while, for the momentum independent part of the potential, we have to consider only the terms which come out from the derivative with respect to the

density:

$$U_q(\rho,\rho_3) \equiv \mathcal{A}\frac{D\mathcal{E}_{pot}}{Df_q} = \frac{\partial \mathcal{E}_{pot}}{\partial \rho_q}. \tag{A.26}$$

Since ρ_q and τ_q depend on the momentum, in order to maintain the translational invariance, the momentum dependent part of the potential has to be changed, according to this expression:

$$\rho_q\tau_q[f_q] = \frac{1}{2\hbar^2}\int \frac{d^3\mathbf{p}}{h^3/2}\int \frac{d^3\mathbf{p}'}{h^3/2}(\mathbf{p}-\mathbf{p}')^2 f_q(\mathbf{p})f_q(\mathbf{p}'). \tag{A.27}$$

As a consequence, the functional $\mathcal{E}_{eff}$ can be rewritten as

$$\begin{aligned}
\mathcal{E}_{eff} &= C_{eff}\rho\tau + D_{eff}\rho_3\tau_3 \\
&= \frac{C_{eff}}{2\hbar^2}\int \frac{d^3\mathbf{p}}{h^3/2}\int \frac{d^3\mathbf{p}'}{h^3/2}(\mathbf{p}-\mathbf{p}')^2\left[f_n(\mathbf{p})+f_p(\mathbf{p})\right]\left[f_n(\mathbf{p}')+f_p(\mathbf{p}')\right] \\
&+ \frac{D_{eff}}{2\hbar^2}\int \frac{d^3\mathbf{p}}{h^3/2}\int \frac{d^3\mathbf{p}'}{h^3/2}(\mathbf{p}-\mathbf{p}')^2\left[f_n(\mathbf{p})-f_p(\mathbf{p})\right]\left[f_n(\mathbf{p}')-f_p(\mathbf{p}')\right] \\
&= \frac{C_{eff}}{2\hbar^2}\int \frac{d^3\mathbf{p}}{h^3/2}\int \frac{d^3\mathbf{p}'}{h^3/2}(\mathbf{p}-\mathbf{p}')^2 \sum_{q,q'=n,p} f_q(\mathbf{p})f_{q'}(\mathbf{p}') \\
&+ \frac{D_{eff}}{2\hbar^2}\int \frac{d^3\mathbf{p}}{h^3/2}\int \frac{d^3\mathbf{p}'}{h^3/2}(\mathbf{p}-\mathbf{p}')^2\left[\sum_{q=n,p} f_q(\mathbf{p})f_q(\mathbf{p}') - \sum_{q,q'=n,p}^{q\neq q'} f_q(\mathbf{p})f_{q'}(\mathbf{p}')\right]
\end{aligned} \tag{A.28}$$

Under the previous position, the contribution to the single particle energy will be given by

$$\begin{aligned}
\tilde{U}_q(\rho,\rho_3,\tau,\tau_3) &\equiv \mathcal{A}\frac{D\mathcal{E}_{eff}}{Df_q} \\
&= \frac{1}{\hbar^2}\int \frac{d^3\mathbf{p}'}{h^3/2}(\mathbf{p}-\mathbf{p}')^2\left\{C_{eff}\left[f_n(\mathbf{p}')+f_p(\mathbf{p}')\right] \pm D_{eff}\left[f_n(\mathbf{p}')-f_p(\mathbf{p}')\right]\right\} \\
&= \int \frac{d^3\mathbf{p}'}{h^3/2}(\mathbf{p}-\mathbf{p}')^2\left[g_{\pm}f_n(\mathbf{p}')+g_{\mp}f_p(\mathbf{p}')\right] \qquad q=n,p
\end{aligned} \tag{A.29}$$

where the upper sign refers to neutrons and the lower sign to protons. More-

over, we defined he two constants g_+ and g_- as

$$g_+ \equiv \frac{C_{eff} + D_{eff}}{\hbar^2} \qquad g_- \equiv \frac{C_{eff} - D_{eff}}{\hbar^2}. \tag{A.30}$$

Finally, including all contibutions obtained in Eq. (A.25), Eq. (A.26), Eq. (A.29), we can write the single particle energy ϵ_q as

$$\epsilon_q = \varepsilon + U_q(\rho, \rho_3) + \tilde{U}_q(\rho, \rho_3, \tau, \tau_3) \tag{A.31}$$

Under a small amplitude perturbation of the distribution function of each nuclear species δf_q as in Eq. (5.6),the single particle energy functional ϵ_q is correspondingly modified as:

$$\epsilon_q \equiv \epsilon_q[f_n, f_p] \approx \epsilon_q[f_n^0, f_p^0] + \epsilon_q[\delta f_n, \delta f_p] = \epsilon_q^0 + \delta\epsilon_q \tag{A.32}$$

where the quantity $\delta\epsilon_q$ is given by:

$$\begin{aligned}
\delta\epsilon_q &= \mathcal{A} \int \frac{d^3\mathbf{p}'}{\hbar^3/2} \sum_{q'=n,p} \frac{D\epsilon_q}{Df_{q'}} \delta f_{q'} \\
&= \mathcal{A} \int \frac{d^3\mathbf{p}'}{\hbar^3/2} \sum_{q',q''=n,p} \left(\frac{\partial\epsilon_q}{\partial\rho_{q''}} \frac{D\rho_{q''}}{Df_{q'}} + \frac{\partial\epsilon_q}{\partial\tau_{q''}} \frac{D\tau_{q''}}{Df_{q'}} \right) \delta f_{q'} \\
&= \sum_{q'=n,p} \int \frac{d^3\mathbf{p}'}{\hbar^3/2} \left(\frac{\partial\epsilon_q}{\partial\rho_{q'}} + \frac{p^2}{\hbar^2} \frac{\partial\epsilon_q}{\partial\tau_{q'}} \right) \delta f_{q'}.
\end{aligned} \tag{A.33}$$

A.6 Linearized Vlasov equations

Let us to find the various contributions of the linearized Vlasov equations, Eq. (5.7). For the $\nabla_{\mathbf{p}}\epsilon_q^0$ and $\nabla_{\mathbf{p}} f_q^0$, making use of the definition of effective mass, we easily get

$$\begin{aligned}
\nabla_{\mathbf{p}}\, \epsilon_q^0 &= \frac{\mathbf{p}}{m} + \nabla_{\mathbf{p}}\, \tilde{U} = \frac{\mathbf{p}}{m} + \frac{\mathbf{p}}{m} \left(\frac{m}{m_q^*} - 1 \right) = \frac{\mathbf{p}}{m_q^*} \\
\nabla_{\mathbf{p}} f_q^0 &= \frac{df_q^0}{d\epsilon_q} \nabla_{\mathbf{p}}\, \epsilon_q^0 = \frac{df_q^0}{d\epsilon_q} \frac{\mathbf{p}}{m_q^*}.
\end{aligned} \tag{A.34}$$

Since we are looking for plane-wave solutions δf_q as in Eq. (5.8), replacing the latter expressions, together with the one we found in Eq. (A.33), in Eq. (5.7), after some algebraic calculations, we obtain:

$$\left(\omega_k + \frac{\mathbf{p}\cdot\mathbf{k}}{m_q^*}\right)\delta f_q^k = \frac{df_q^0}{d\epsilon_q}\frac{\mathbf{p}\cdot\mathbf{k}}{m_q^*}\sum_{q'=n,p}\left(\int\frac{d^3\mathbf{p}'}{\hbar^3/2}\frac{\partial U_q}{\partial\rho_{q'}}\delta f_{q'}^k + \delta\tilde{U}_{q'}^k\right) \qquad \forall k. \tag{A.35}$$

Owing to the requirement of translational invariance, the contribution of $\tilde{U}_q$ cannot be evaluated from the Eq. (A.33). But looking at the result we got in Eq. (A.29), it is immediate to obtain its variation as:

$$\delta\tilde{U}_q = \int\frac{d^3\mathbf{p}'}{h^3/2}(\mathbf{p}-\mathbf{p}')^2\left[g_\pm\delta f_n(\mathbf{p}') + g_\mp\delta f_p(\mathbf{p}')\right] \qquad q = n,p \tag{A.36}$$

where, as in Eq. (A.29), the upper sign refers to neutrons and the lower sign to protons. By introducing this expression in Eq. (A.35), we finally get:

$$\begin{aligned}\delta f_q^k &= \frac{df_q^0}{d\epsilon_q}\left(\frac{\frac{\mathbf{p}\cdot\mathbf{k}}{m_q^*}}{\omega_k + \frac{\mathbf{p}\cdot\mathbf{k}}{m_q^*}}\right)\sum_{q'=n,p}\int\frac{d^3\mathbf{p}'}{h^3/2}\left\{\frac{\partial U_q}{\partial\rho_{q'}} + (\mathbf{p}-\mathbf{p}')^2[g_+\delta_{q,q'} + g_-(1-\delta_{q,q'})]\right\}\delta f_{q'}^k \\ &= \frac{df_q^0}{d\epsilon_q}\left(\frac{\frac{\mathbf{p}\cdot\mathbf{k}}{m_q^*}}{\omega_k + \frac{\mathbf{p}\cdot\mathbf{k}}{m_q^*}}\right)\sum_{q'=n,p}\int\frac{p'^2dp'}{h^3/2}d^2\Omega\left\{\frac{\partial U_q}{\partial\rho_{q'}} + (\mathbf{p}-\mathbf{p}')^2[g_+\delta_{q,q'} + g_-(1-\delta_{q,q'})]\right\}\delta f_{q'}^k.\end{aligned} \tag{A.37}$$

Performing now a change in the integration variable

$$p' \to \varepsilon' = \frac{p'^2}{2m} \tag{A.38}$$

the equation Eq. (A.37) becomes

$$\delta f_q^k = \frac{df_q^0}{d\epsilon_q}\left(\frac{\frac{\mathbf{p}\cdot\mathbf{k}}{m_q^*}}{\omega_k + \frac{\mathbf{p}\cdot\mathbf{k}}{m_q^*}}\right)\sum_{q'=n,p}\int\frac{\sqrt{\varepsilon'}d\varepsilon'}{\frac{2}{3}\frac{\epsilon_{Fq}^{3/2}}{\rho_q}}\frac{d^2\Omega}{4\pi}\left\{\frac{\partial U_q}{\partial\rho_{q'}} + (\mathbf{p}-\mathbf{p}')^2[g_+\delta_{q,q'} + g_-(1-\delta_{q,q'})]\right\}\delta f_{q'}^k, \tag{A.39}$$

where the following identity, deduced by the definition of the Fermi energy, has been introduced

$$\frac{h^3}{2} = \frac{4}{3}\pi\frac{(2m\epsilon_{Fq})^{3/2}}{\rho_q}. \tag{A.40}$$

Let us consider now, as distribution function at equilibrium, the Fermi-Dirac distribution at zero temperature, that is the Heaviside step function

$$f_q^0(\mathbf{p}) \equiv f_q^0(\epsilon_q) = \Theta(\varepsilon - \epsilon_{Fq}^*), \tag{A.41}$$

where ϵ_{Fq}^* is the modified Fermi energy of the nuclear species q defined as

$$\epsilon_{Fq}^* = \frac{m}{m_q^*}\epsilon_{Fq}. \tag{A.42}$$

With this assumption, the f_q^0 derivative which appear previously become

$$\frac{df_q^0}{d\epsilon_q} = -\delta(\varepsilon_q - \epsilon_{Fq}^*) \tag{A.43}$$

and integrating both sides of the relation Eq. (A.37) in the variable ε and then in ε', we finally obtain:

$$\delta\phi_q^k = -\left(\frac{\frac{\mathbf{p}_F\cdot\mathbf{k}}{m_q^*}}{\omega_k + \frac{\mathbf{p}_F\cdot\mathbf{k}}{m_q^*}}\right)\sum_{q'=n,p}\frac{1}{\frac{2}{3}\frac{\varepsilon_{Fq}^*}{\rho_q}}\frac{d^2\Omega}{4\pi}\left\{\frac{\partial U_q}{\partial\rho_{q'}} + 2p_F^2(1-\cos\theta_{\mathbf{p},\mathbf{p}'})[g_+\delta_{q,q'} + g_-(1-\delta_{q,q'})]\right\}\delta\phi_{q'}^k, \tag{A.44}$$

where $\delta\phi_q^k$ has been defined as

$$\delta\phi_q^k(\Omega) \equiv \int d\varepsilon\delta f_q^k. \tag{A.45}$$

In terms of the average level density at zero temperature

$$N_q(0) = \frac{2}{3}\frac{\epsilon_{Fq}^*}{\rho_q}, \tag{A.46}$$

one can also define, as usually, the Landau parameters as it follows:

$$L_{0\,qq'} = N_q^{-1}(0)\left\{\frac{\partial U_q}{\partial \rho_{q'}} + \left[g_+\delta_{q,q'} + g_-(1-\delta_{q,q'})\right]\left(p_{Fq}^2 + p_{Fq'}^2\right)\right\}$$
$$L_{1\,qq'} = -2N_q^{-1}(0)\left[g_+\delta_{q,q'} + g_-(1-\delta_{q,q'})\right]p_{Fq}\,p_{Fq'}, \tag{A.47}$$

so that, by denoting with $\mathbf{v}_{Fq}^* = \frac{\mathbf{p}_F}{m_q^*}$, the modified Fermi velocity, the Eq. (A.44) can be rewritten as:

$$\begin{aligned}\delta\phi_q^k &= -\left(\frac{v_{Fq}^* k\cos\theta_{\mathbf{p},\mathbf{k}}}{\omega_k + v_{Fq}^* k\cos\theta_{\mathbf{p},\mathbf{k}}}\right)\sum_{q'=n,p}\int\frac{d^2\Omega}{4\pi}L_{qq'}\delta\phi_{q'}^k \\ &= -\left(\frac{\cos\theta_{\mathbf{p},\mathbf{k}}}{s_q + \cos\theta_{\mathbf{p},\mathbf{k}}}\right)\sum_{q'=n,p}\int\frac{d^2\Omega}{4\pi}L_{qq'}\delta\phi_{q'}^k,\end{aligned} \tag{A.48}$$

where the parameter $L_{qq'}$ are defined as

$$L_{qq'} = L_{0\,qq'} + L_{1\,qq'}\cos\theta_{\mathbf{p},\mathbf{p}'} \tag{A.49}$$

while s_q is the (dimensionless) sound velocity in unit of modified Fermi velocity, that is:

$$s_q \equiv \frac{v_s}{v_{Fq}^*} = \frac{\omega_k}{k v_{Fq}^*}. \tag{A.50}$$

Let us consider now a decomposition of $\delta\phi_q^k$ into spherical harmonics $Y_l^m(\theta,\phi)$, with $m = 0$ (Legendre polynomials $Y_l^0(\theta)$):

$$\delta\phi_q^k = \sum_{l=0,1}\alpha_q^l Y_l^0 = \alpha_q^0\frac{1}{\sqrt{4\pi}} + \alpha_q^1\sqrt{\frac{3}{4\pi}}\cos\theta_{\mathbf{p},\mathbf{k}}. \tag{A.51}$$

By replacing this development on Eq. (A.48), we have:

$$\sum_{l=0,1}\alpha_q^l Y_l^0 = -\left(\frac{\cos\theta_{\mathbf{p},\mathbf{k}}}{s_q + \cos\theta_{\mathbf{p},\mathbf{k}}}\right)\sum_{q'=n,p}\int\frac{d^2\Omega}{4\pi}\left(L_{qq'}\sum_{l=0,1}\alpha_{q'}^l Y_l^0\right) \tag{A.52}$$

and so, by integrating on Ω and noting that

$$\sum_{l=0,1}\int\frac{d^2\Omega}{4\pi}L_{qq'}Y_l^0=\sum_{i=0,1}\beta_i L_{i\,qq'}Y_i^0,\quad \beta_0=1,\quad \beta_1=\frac{1}{3} \tag{A.53}$$

it is possible to obtain finally the following relation:

$$\sum_{l=0,1}\alpha_q^l Y_l^0=-\left(\frac{\cos\theta_{\mathbf{p},\mathbf{k}}}{s_q+\cos\theta_{\mathbf{p},\mathbf{k}}}\right)\sum_{i=0,1}\beta_i Y_i^0\sum_{q'=n,p}\alpha_{q'}^i L_{i\,qq'}. \tag{A.54}$$

In order to get the four coefficients α_q^l, with $q=p,n$ and $l=0,1$, we need to integrate twice, for each q, the previous equation. So, by integrating a first time on $\cos\theta_{\mathbf{p},\mathbf{k}}$, taking into account that

$$\begin{aligned}\int_0^\pi d\cos\theta_{\mathbf{p},\mathbf{k}}\frac{\cos\theta_{\mathbf{p},\mathbf{k}}}{s_q+\cos\theta_{\mathbf{p},\mathbf{k}}}&=2\left[1-\frac{s_q}{2}\ln\left(\frac{s_q+1}{s_q-1}\right)\right]\equiv 2\chi(s_q)\\ \int_0^\pi d\cos\theta_{\mathbf{p},\mathbf{k}}\frac{\cos^2\theta_{\mathbf{p},\mathbf{k}}}{s_q+\cos\theta_{\mathbf{p},\mathbf{k}}}&=-2s_q\left[1-\frac{s_q}{2}\ln\left(\frac{s_q+1}{s_q-1}\right)\right]=-2s_q\chi(s_q)\end{aligned} \tag{A.55}$$

with $\chi_q=\chi(s_q)$ defined as the Lindhard function and by multiplying both of sides for $\frac{\sqrt{4\pi}}{2}$ we achieve the first dispersion relation of Eq. (5.9), that is:

$$c_0\alpha_q^0=-\sum_{l=0,1}c_l\,s_q^l\,\chi_q\sum_{q'=n,p}\alpha_{q'}^l L_{l\,qq'}\qquad c_0=-1,\quad c_1=\frac{\sqrt{3}}{3} \tag{A.56}$$

On the other hand, by multiplying both sides of Eq. (A.54) for $\cos\theta_{\mathbf{p},\mathbf{k}}$ and performing the same integration and simplification as before, one achieves the second one of Eq. (5.9)

$$c_1\alpha_q^1=-\sum_{l=0,1}c_l\,s_q^{l+1}\,\chi_q\sum_{q'=n,p}\alpha_{q'}^l L_{l\,qq'}-c_1\gamma \tag{A.57}$$

with γ defined as in (5.10) and having considered the result obtained in Eq. (A.55)

and the following last one

$$\int_0^{\pi} d\cos\theta_{\mathbf{p},\mathbf{k}} \frac{\cos^3\theta_{\mathbf{p},\mathbf{k}}}{s_q + \cos\theta_{\mathbf{p},\mathbf{k}}} = 2\left[\frac{1}{3} + s_q^2\chi(s_q)\right]. \tag{A.58}$$